Title	Mechanical basis of the competition for space in heterogeneous cell populations
Author(s)	坪井, 有寿
Citation	大阪大学, 2018, 博士論文
Version Type	VoR
URL	https://doi.org/10.18910/70675
rights	
Note	

Mechanical basis of the competition for space in heterogeneous cell populations

ヘテロな細胞集団間でおこる競合的な組織占有の力学的基盤の解明

Tsuboi, Alice

Laboratory of Theoretical Biology, Department of Biological Sciences,
Graduate School of Science, Osaka University

大阪大学大学院理学研究科　生物科学専攻　理論生物学研究室
坪井有寿

Contents

Abstract

Publication List

Acknowledgements

1. Introduction

Abstract

地球上の多種多様な生き物は、互いに関わりあうことで共同社会(生態系)を構成する。同じ社会に異なる種が存在することによって、単一種のみで存在していたときには見られないような協調・競合的な振る舞いが生まれる。たとえば、同じ場所に異なる種が生息すると、限られた領地をめぐって、生息域の棲み分け、競争排除、共存などが起こる。このような領地争いが、多細胞生物における細胞社会にも存在することがわかりつつある。たとえば、化学的・力学的に異なる細胞集団を同一組織内に共存させると、細胞同士が互いにモザイク状に混ざり合う、クラスター状に分離するなど、組織という限られた領地内で様々な空間分布を示す(Tsuboi et al. 2017)。また、近接する異なる細胞同士で、互いにその適応度を競合し領地を奪い合う適者生存競争も報告されている。本研究では、生体内に生じた腫瘍などの適応度の高い細胞と正常な周辺組織の間で見られる領地争いに注目した。

腫瘍形成の初期段階において、生体内に生じた変異細胞は周囲の正常細胞による空間的制約を受けながら拡大していく。この領地拡大は、単に腫瘍細胞の増殖が速いことのみに起因するのではなく、“細胞競合”によって、相対的な適応度の高い変異細胞(勝者)が正常な周辺組織(敗者)を排除することで駆動される(Eichenlaub, Cohen, and Herranz 2016; Suijkerbuijk et al. 2016)。複数の細胞競合関連因子の同定により、適応度の低い細胞を細胞死に導く機構が解明された。一方で、細胞死に引き続いて、勝者が選択的に失われた空間を埋めていく機構はよくわかっていない。そこで、上皮組織の力学的変形を再現する数理モデル Cell Vertex Model (CVM)とショウジョウバエ実験を組み合わせ、細胞死で失われた領地をめぐって周囲の細胞がどのように競合するかを調べた。

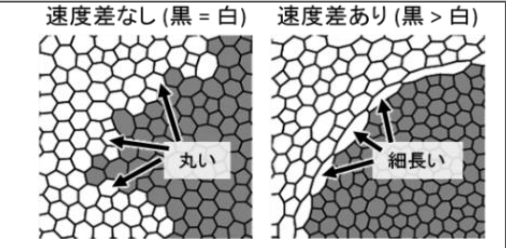

図 1 分裂速度差による細胞変形

これまでに、多くの細胞競合系において勝者が高い増殖活性をもつことが報告されている(例：Hippo 経路変異細胞(Tyler et al. 2007))。そこでまず、勝者の出現により生じた分裂速度差が細胞集団へ与える影響を調べた。その結果、CVM とショウジョウバエ実験の両方に

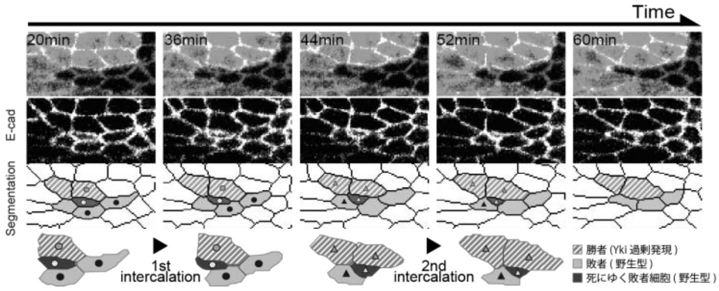

図 2 細胞死で失われた領地をめぐる競合 (ショウジョウバエ実験)
Yki (Hippo 経路の下流で働く転写共役因子)を過剰発現した細胞に隣接する野生型細胞が組織から排除される様子。

おいて、分裂の遅い細胞が細胞集団(クローン)の境界に沿って細長く変形することを見出した(図 1 右)。次に、ショウジョウバエ上皮の細胞競合ライブ観察系を構築し、Yki 過剰発現細胞(勝者)に隣接する野生型細胞(敗者)が細胞死によって排除される過程を定量画像解析した(図 2)。野生型細胞は細胞死の前後でほとんど面積に変化がないのに対して、Yki 過剰発現細胞は細胞死直後から急激に成長して死んだ細胞の面積をほぼ占有した。興味深いことに、この非対称な面積獲得は、死んだ細胞の異方性が高い(細長い; 図 1 右)ほど顕著になった。死ぬ細胞の形が死んだ細胞の領地をめぐる競合の勝敗を規定することから、非対称な面積獲得は、勝者細胞の自律的な成長に起因するのではなく、死細胞と勝者細胞の相互作用よって細胞非自律的に制御されることが予測された。加えて、細胞の力学性質に基づいて構築された CVM による解析でも、ライブ観察と同様に勝者が選択的に拡大したことから、細胞死後の非対称な面積獲得は生化学反応よりもむしろ力学的・幾何学的な細胞性質により制御されることが示唆された。

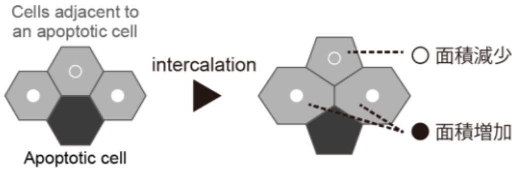

図 3 Cell intercalation による細胞面積変化
Intercalation による細胞配置換えの結果、アポトーシス細胞に接する 3 つの細胞のうち 1 つの細胞(○)の面積が減少し、2 つの細胞(●)の面積が増加する。

以上の結果より、死ぬ細胞が細長くなることで、勝者が選択的に領地を占有していくことが示唆された。ではなぜ、死ぬ細胞の幾何形状が勝者細胞の拡大に重大な影響をもたらすのだろうか？死細胞が異方的である(細長い)場合、異方的でない(丸い)場合の死ぬプロセスの違いを検討したところ、死細胞が排除される過程で繰り返し起こる細胞の配置換え(cell intercalation; 図 2 下)の方向に違いがあった。死ぬ細胞の形が細長い場合には、クローン境界から垂直な細胞辺にバイアスして intercalation が起こるのに対して、丸い場合には全ての細胞辺で等確率に intercalation が起こった。intercalation は面積変化を伴うため(図 3; Heller et al., 2016)、intercalation 方向のバイアスにより、勝者選択的な拡大が達成されると予想した。そこで、実際に CVM において intercalation の方向に人為的なバイアスを導入し、細胞死後の面積変化を測定した結果、intercalation の方向制御のみで十分に勝者細胞の拡大が再現できた。さらに、intercalation を介した勝者細胞の拡大が長期間維持されることで、組織スケールで勝者の領地が拡大することも確認できた。

細胞競合は、上皮組織構造の“破壊(敗者の細胞死)”と“再構築(勝者細胞による占有)”の繰り返しと捉えることができる。一般的に、上皮組織は隣接する細胞間が接着し強く結合したシート状の構造をもつため、上皮の接着結合を維持したまま敗者を勝者に置き換えるには、細胞死によって失われた空間を効率的に埋める機構が必要である。本研究により、上皮組織に共通する cell intercalation という仕組みを介して、勝者細胞の面積拡大に有利な形で細胞間の隣接関係が変化し、細胞死で失われた領地を適切に埋めることが示された。細胞の面積

成長は、力学的なフィードバックを介して細胞増殖を促進することが報告されており (Aragona et al. 2013; Gudipaty et al. 2017)、勝者細胞の面積成長はさらに増殖活性を高めうると予想される。本研究で明らかにした細胞死後の勝者優先的な組織占有メカニズムは、腫瘍が空間的な制約を受けつつも急速にその陣地を広げる原理の理解につながると考えられる。

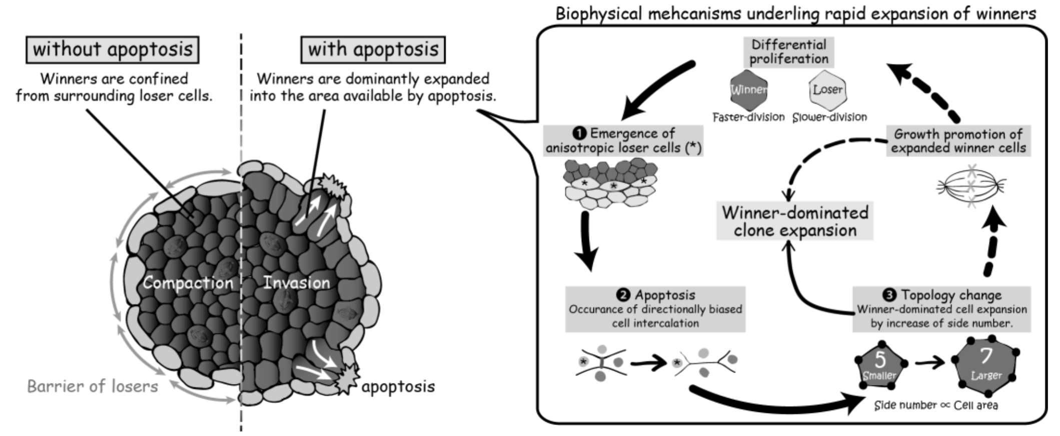

図 4　細胞死により失われた空間をめぐり、勝者が拡大するプロセスの概要

Publication List

1 Alice Tsuboi†, Daiki Umetsu†, Erina Kuranaga and Koichi Fujimoto (2017) Inference of Cell Mechanics in Heterogeneous Epithelial Tissue Based on Multivariate Clone Shape Quantification. *Frontiers in Cell and Developmental Biology* 5:68.
doi: 10.3389/fcell.2017.00068.
†: Equal contribution

2 Alice Tsuboi, Shizue Ohsawa, Daiki Umetsu, Yukari Sando, Erina Kuranaga, Tatsushi Igaki and Koichi Fujimoto (2018) Competition for space is controlled by apoptosis-induced change of local epithelial topology. *Current Biology*, in press
doi: 10.1016/j.cub.2018.05.029

Acknowledgements

I would like to thank Associate Prof. K. Fujimoto for instruction and discussion. I also deeply thank Drs. D. Umetsu, E. Kuranaga, S. Ohsawa, T. Igaki, Y. Sando for their generous cooperation. I am grateful to Drs. K. Matsuno, H. Oda, M. Okada for advices and comments. Also I would like to thank Drs. T. Kondo, K. Hironaka, M. S. Kitazawa, and K. Matsushita for valuable comments on the manuscript draft; Drs. S. Hayashi, S. Ishihara, and K. Sugimura for discussions; Drs. K. Matsuno for technical support; Drs. K. Ikeguchi, Y. Matsumoto, M. Hirohata, M. Kishino and M. Kobayashi for the segmentation of experimental images; Drs. T. Xu, Bloomington Stock Center, and Vienna Drosophila Resource Center for fly stocks. Drs. B. Aigouy for tissue analyzer. This work was supported by Grant-in-Aid for JSPS Fellows (15J01837).

1. Introduction

1.1. Background of thesis

Self-organized structure of living organisms has fascinated many scientists for centuries. How to robustly generate the ordered structure against extrinsic environmental and/or internal genetic noise (perturbation, disturbance) is a fundamental question for developmental biology. Morphogenesis emerges from cooperative and competitive cell-cell interactions within a tissue, which is composed of a large number of heterogeneous cell populations. When different clonal cell populations arise in a tissue due to different gene expression, the different populations are often actively mixed or sorted, consequently promoting or inhibiting the cellular interactions. The different mixing state is known to be regulated by cellular mechanical forces, such as cell pressure and interfacial tension. Therefore, study from a mechanical point of view would provide several perspectives on cell behaviors under heterogeneous populations.

Researchers have long attempted to understand the biological phenomenon from physics and mathematics. In the early 20th century, D'Arcy Thompson explained the shape and structure of living organism from physical and mathematical principle in his famous book "On Growth and Form" (Thompson 1917). In this book, he proposed a structural similarity between bubbles in a foam and cells in a tissue, and provided the concepts that cell shape and packing in living matter could be explained by mechanical force such as tension and pressure. In the same 20th century, his idea inspired F.T Lewis to study characteristics of cellular topology in epithelia. Lewis provided some empirical laws which commonly applicable to multicellular organisms from quantitative observations, and he also tried to understand the laws from mathematical concepts. At a later time, along with the advent and progress of molecular biology, several molecules regulating cellular mechanics have been identified, and revealed the molecular basis for supporting their findings. Additionally, theoretical model based on cellular forces (e.g. cell bond tension and apical area contraction) also supported their findings by successfully capturing the universal feature of the cells. For modern developmental biology, many fundamental concepts have been provided through combining *in silico* and *in vivo* experiments. This led me to use the combinatorial approaches to study the cellular behavior under heterogeneous population.

1.2. Overview of epithelial tissue

Epithelial tissue is one of the four basic tissue types (epithelial, connective, muscle, and nervous tissue) in many multicellular organisms including human. Epithelial tissue is a sheet of cells connected tightly together, and exists as a part of organs. They can take several forms, which include hollow tubes, sacs, and compound of the structures, and function for barrier, secretion or absorption. Given that simple sheet structure can generate such complex structures and functions, it goes without saying that epithelial tissue is very fascinating for developmental biology. Additionally, epithelial tissues are relevant to pathology, because many of cancers originate from epithelial tissues. Therefore, the importance of epithelial tissues has been well illustrated in the fields of basic and applied researches. Here, I first introduce structures of epithelium (1.3), especially in light of "cell topology" which the properties characterizing planar network structure (1.4–1.6).

1.3. Structure of epithelium

1.3.1. Types of epithelium

Simple monolayer of epithelial tissues is typically classified to four types based on the morphology of the cells (Gibson and Gibson 2009): (1) squamous cells with flat shape (width is larger than height), (2) cuboidal cells with cube shape (width and height are approximately the same), (3) Columnar cells with column shape (height is taller than width), (4) pseudostratified cells with showing interdigitated nuclei positioning when sectioned, even though all cells still rest on the basement membrane.

1.3.2. Cell polarization

Cell polarization is a fundamental feature of epithelia which ensures the proper functions of diffusion barrier, directional transport for secretion and absorption, and so on. In contrast, loss of cell polarization leads to destruction of tissue homeostasis like tumor progression. Epithelial polarity is established by maintaining three plasma membrane domains, 'apical', 'lateral, and 'basal' domains (Tepass et al. 2001). The apical and basolateral domains are separated by adherens junctions (AJs), and the apical domain is further subdivided into the apical surface and the subapical complex/marginal zone. In *Drosophila*, septate junctions (SJs) lie just basal to the AJs and form a trans-epithelial diffusion barrier (Tepass et al. 2001), which is functionally analogous to tight junction in vertebrate (Bilder 2001; Gibson and Gibson 2009; Gibson and Perrimon 2003). Molecules composing each domains have been extensively studied. In *Drosophila*, subapical complex includes Bazooka-PAR6-aPKC, AJs include cadherin, α-catenin, Armadillo (*Drosophila* β-catenin), Canoe (*Drosophila* Afadin), and SJs include Neurexin IV, Fasciclin III, Scribble (Scrib), Disks Large (Dlg), Coracle, and Lethal giant larvae (Lgl) (Bilder 2001; Gibson and Gibson 2009; Gibson and Perrimon 2003; Tepass et al. 2001). Some of the components of SJs, Scrib, Dlg, and Lgl ensures apical-basal polarity and function as neoplastic tumor suppressors.

1.3.3. Planar network at adherens junctions

Epithelial tissue structure is formed by a sheet of tightly connected cells with adhesive molecules between neighbors. Such cell-cell connectivity is represented by a planar network (cell packing pattern) at adherens junction and known to reproduce some empirical properties regarding the planar network structure (see Section 1.4). The mechanical coupling between neighbors at adherens junctions can lead to morphogenetic tissue deformations, such as expansion, contraction, or folding. Therefore, understanding the regulation of apical planar network on the basis of physical properties in several morphogenetic processes would provide mechanistic insight into the phenomenon.

1.4. Properties characterizing planar network structure in epithelial tissue

1.4.1. Difference in "cellular geometry" and "cellular topology"

Planar network structure in epithelial tissue is characterized by two properties, cellular geometry and topology. Cellular geometry specifies cell shape, which implies several geometrical features such as area, anisotropy, side lengths, and internal angles at tri-cellular junctions (Gibson and Gibson 2009; Nagpal, Patel, and Gibson 2008). On the other hand, cellular topology specifies the connectivity among cells in a tissue, which is determined solely by the number of sides (adherent neighbors) of each cell. Specifically, when tissue is stretched in a way that individual cells respectively change their shape but preserve local cellular connective relationships, this manipulation changes the cellular geometry, but preserve cell topology. By contrast, manipulation that changes cell topology are accompanied with a re-connection of cell-cell neighbor relationships, in which cell contacts are lost or made. Modification of these two cellular properties is caused by various elementary cellular processes, such as cell division, death, and rearrangement (cell intercalation) (see Section 1.5), and the modification leads to the macroscopic deformation of epithelial tissue during morphogenesis or pathogenesis.

1.4.2. Characteristics of cellular topology in epithelia

When apical section of cells is approximated to be polygonal in shape, cellular topology in tissue is evaluated by "polygon class", which is a distribution of polygon number (i.e., the number of adherent neighbors) of each cell. The constant distribution of polygon class in tissue was shown in 1928 by F.T. Lewis (Lewis 1928). Lewis noted that cells with different polygon numbers were present in reproducible proportions in plant cucumber epidermal tissue. After the Lewis' pioneering work, the distribution of polygon class has been measured in multiple organisms including animals (*Drosophila*, *Hydra*, *Xenopus*) and plants (*Allium*, *Euonymus*, and *Dryopteris*) (Gibson et al. 2006; KORN and SPALDING 1973; Zallen and Zallen 2004). They exhibit similar distributions with a peak of hexagonal cells, high proportions of pentagonal and heptagonal cells, and lesser proportions of other polygon types.

1.5. Cellular dynamics that change cell topology

For a proliferating epithelium, polygon type is changed by three fundamental cell behaviors including cell division, cell intercalation and apoptosis. All of them associate with creating and destroying polygon types, which consequently generate heterogeneity of epithelial topology. Here I show how each cell behavior changes cell topology.

1.5.1. Cell division

Following cell division, a mother cell produces two daughter cells, which can be interpreted as destroying mother polygon cell and producing two new polygon cells. The polygon type of daughter cells depends on the orientation of cleavage plane of cell division. Additionally, two cells abutting the cleavage plane increase side number by one. Such transition rule of side number by cell division has been shown to explain the equilibrium distribution of topology in proliferating tissue in the absence of cell sorting and migration (Gibson et al. 2006).

1.5.2. Cell intercalation

Cell intercalation, namely cell rearrangement or T1 transition, is a process that adjacent four cells dynamically change their arrangement: an edge shared by two contacting cells is shortened to disappear and a new edge shared by the other two cells is created and lengthened, associating with losing a side for the former two cells and gaining a side for the latter two cells.

1.5.3. Cell delamination

Two types of delaminating process have been described from studies in *Drosophila* epithelial tissue. One of the cell delamination type, namely D1 delamination, proceeds with gradual disappearance of junctions by cell intercalation, which leads to gradual decrease in apical cell area (Marinari et al. 2012). As a consequence of the intercalation between a delaminating cell and its surrounding cells, the topology of surrounding cells are changed. Another type of delamination, D2 delamination, proceeds without junctional loss so as to form a rosette structure (a junction of five or more cells) leading to apical surface shrink rapidly (Marinari et al. 2012). Because the rosette structure is transient and it resolves instantly into an arrangement formed by tri-cellular junctions, this D2 type delamination also results in the topological change of surrounding cells.

1.6. Cellular dynamics linked to cell topology

In many biological systems, it has been increasingly apparent that cell topology is linked to some cellular geometry (i.e., cell area), as well as cellular behaviors (i.e., division, death, intercalation).

1.6.1. Cell area

Differences in topology represented by the number of cell sides is known to connect with apical cell area; cell area has a linear correlation with the number of cell sides. This correlated relationship is known as Lewis’s law, which was made by Lewis in 1928 by observing two-dimensional cellular structure in biological systems, such as cucumber epidermis and pigmented epithelium of the retina

(Lewis 1928). This correlation is also confirmed in *Drosophila* (Farhadifar et al. 2007).

1.6.2. Cell fate

Differences in topology are also known to correlate with different cell fates (Heller et al. 2016). Heller and colleagues performed live imaging in wing disc of *Drosophila*, and analyzed the topological dynamics for specific cell classes selected based on their behavior (i.e., dividing cells, dying cells). They found that cells in the entire tissue show a distribution with an average of approximately six sides (see Section 1.4.2), however, dividing cells have on average one extra side, seven sides, distinctly exhibiting a distribution shifted over by one (Gibson et al. 2006, 2014; Heller et al. 2016). This mitotic shift in the frequency of polygon classes is observed several hours prior to division due to increasing in side number of dividing cells twice faster than non-dividing cells. These results sugest that dividing cells accumulate side number over time. In contrast, dying cells decrease side number on average prior to being delaminated. Additionally, they also observed cell area of dividing cells is relatively large, but the one of dying cells is small, consistent with Lewis's law (see Section 1.6.1).

1.6.3. Cell intercalation (T1 transition)

Cell intercalation occurs among four connected cells, in which two pair of cells gain an edge and the other two cells lose. From a live imaging of *Drosophila* wing disc, Heller and colleagues found that cells that will lose an edge have larger side number before intercalation than the cells that will gain an edge (Heller et al. 2016). In more detail, the cells that gain an edge are hexagons (6-sided) or pentagons (5-sided) at the start of intercalation and changed to heptagons (7-sided) or hexagons (6-sided) at the end of intercalation, whereas the cells that lose an edge are heptagons (7-sided) or hexagons (6-sided) at the start and changed to hexagons (6-sided) or pentagons (5-sided) at the end. This was indicating that original topology before intercalation affects the junctional dynamics during cell intercalation.

1.6.4. Tissue mechanics leading to cell intercalation

The mechanisms leading to the junction shortening and lengthening have been extensively studied in gastrulation of *Drosophila* embryo, where germband elongates along its anterior-posterior (AP) direction through intercalation. The studies led to the two models of the intercalation, global external tissue scale tensile stress and local regulation of contractility. The global tensile stress is mainly generated by the invagination of endoderm, which promotes AP-junction elongation and DV (dorso-ventral)-junction shortening, which might facilitate polarized cell intercalation (Lye et al. 2015). This may be correspond to the intercalation driven by "a passive force equilibrium mechanism" described in wing disc epithelial tissue of *Drosophila* by Heller and colleagues, who showed that shorter junctions are more likely to undergo intercalation (Heller et al. 2016). This passive mechanism may be also relevant to a report that junctions are subject to stochastic fluctuations of edge length that trigger cell intercalations by chance as edge lengths decrease to zero (Curran et al. 2017). In this framework, shorter junctions are likely to undergo intercalation, because they are more easily decrease to zero. Together, these framework suggests that global stress biases junctional length along a specific direction, which raises the probability to undergo cell intercalation to the shorter junctions.

In parallel with this global stress, local tensile forces generated by non-muscle Myosin II polarization also drives intercalation. Convergent extension driven by polarized Myosin II was also involved in gastrulation and neurulation (Lienkamp et al. 2012; Nishimura, Honda, and Takeichi 2012; Nishimura and Takeichi 2008; Shindo and Wallingford 2014). Numerous recent studies further showed the underling mechanism to control the Myosin II polarization. During the germ band extension in *Drosophila*, The expression of three Toll family receptors (Toll-2, Toll-6 and Toll-8) in overlapping transverse stripes along AP axis provides positional information for the AP patterning, which polarizes Myosin II at DV-junctions and drives the polarized cell intercalation (Paré et al. 2014). As another mechanism acting in parallel or downstream of Toll receptor signaling, G-protein-coupled receptors (GPCRs) were also shown to be required for polarized myosin II-driven intercalation. A ubiquitously expressed GPCR, Smog regulates G proteins with other GPCRs (Mist and yet unknown GPCR), resulting in activation of Myosin II through the Rho1-Rok pathway (Kerridge et al. 2016). Whereas Toll receptors and GPCR seem to act as the most upstream of polarized myosin II-driven intercalation, some additional actors were reported; Shroom (action- and Rho-kinase-binding protein) (Simões, Mainieri, and Zallen 2014), Abelson kinase (non-receptor tyrosine kinase) (Tamada, Farrell, and Zallen 2012), Bazooka (*Drosophila* Par-3; polarity protein) (Simões et al. 2010), Canoe (*Drosophila* afadin; actin-binding protein) (Sawyer et al. 2011), and β-catenin and E-cadherin (adhesion molecules) (Levayer and Lecuit 2013; Rauzi, Lenne, and Lecuit 2010; Tamada et al. 2012). Another Myosin Dachs, whose localization is defined by the asymmetric arrangement of protocadherin Fat-Dachsous heterodimers between adjacent cells and Golgi kinase Four-jointed, is also known to drive intercalation by increasing junction tension (Bosveld et al. 2012; Hale and Strutt 2015).

As shown above, junction dynamics at adherens junctions have been so far the main focus of the research of cell intercalation. A recent report was shown the basolateral cellular mechanics also contributes to drive intercalation (Sun et al. 2017). They showed the basolateral side of cells migrates prior to the apical side, and the basolateral migration is regulated independent of apical junction shortening. Furthermore, as a regulator of the basolateral migration, they identified tyrosine kinase Src42A which modulates Rac1-dependent protrusive motility. Such contribution of the basal protrusions was also reported in the convergent extension of the mouse neural plate. Altogether, the active migration at basal side of cells also plays a pivotal role in the cell intercalation.

While the most studies of cell intercalation were focused on the junction shortening, the junction lengthening after forming a four-way vertex is also critical for the completion of intercalation. In *Drosophila* wing development, Myosin II concentration, which has raised during the shortening of junctions, turned to conversely decrease during the elongation of the newly formed junctions through a regulation of the tumor suppressor PTEN (Bardet et al. 2013). Contrary to the decrease in Myosin II concentration at the newly formed junctions, Myosin II accumulation near the vertex in the neighbor cells also contributes to junction elongation (Collinet et al. 2015; Hara, Shagirov, and Toyama 2016). In addition to such local junction dynamics, global tissue-scale mechanical force driven by the invagination of the posterior midgut is also known to be involved in junction lengthening in *Drosophila* germ band elongation (Collinet et al. 2015). In sum, these findings suggest that the process of junction lengthening is not a passive relaxation process, but is a rather actively regulated process.

1.7. Overview of cell competition

Cell competition is a fitness-comparison mechanism within heterogeneous epithelial tissue due to mutations and/or stochastic changes in gene expression. During competition, cells with lower fitness (losers) are eliminated via apoptosis, and the space left by apoptotic cells is selectively occupied by cells with higher fitness (winners). This elimination occurs in heterogeneous tissue where loser cells coexist with winners, but not under homogeneous tissue consisting only of cells with equal fitness. Cell competition phenomenon could play a fundamental role in ensuring tissue homeostasis as well as cancer progression in both *Drosophila* and mammals. So far, several mutations have been shown to cause differences in fitness, resulting in winners and losers and triggering context-dependent elimination of losers. Such mutations include those that cause differential growth, disruption of apico-basal polarity, sharp differences in the expression of signaling. Here, I first describe what mutations induce cell competition (Section 1.8), how these mutations affect cell fitness and drives context-dependent elimination of losers (Section 1.9), and show physiological roles of cell competition (Section 1.10).

1.8. Inducers of cell competition

1.8.1. Growth differential

Cell competition phenomenon was first described more than 30 years ago by Morata and Ripoll, who showed in mosaics of *Minute* (*M*), which encodes ribosomal protein (Marygold et al. 2007), in growing epithelial tissue of *Drosophila* (Morata and Ripoll 1975). The homozygous flies (*M/M*), which lack both alleles of *Minute* gene, are lethal, but heterozygous flies (*M/+*) are viable. The *M/+* flies showed a developmental delay due to slower proliferation rate driven by reduction of biosynthetic activity, but reached normal body size without major defects of patterning, indicating that *M/+* cells are viable. However, *M/+* cells induced in a tissue with wild-type background do not contribute to adult organism, suggesting that *M/+* cells which coexist with wild-type cells are eliminated from the tissue. Subsequent work on *Minute* in flies, it has been shown that mammalian *Minute* gene called *Bst*, which encodes Rpl24 riboprotein, also drives context-dependent elimination of heterozygous cells in chimeras (Oliver

2004). This was strongly suggesting that cell competition driven by ribosomal activity is conserved across evolutionary phyla.

The contribution of the effects of translational activity to cell competition was later confirmed in *Drosophila* by analysis of different dose of Myc, a transcription factor regulating cell growth and ribosome biogenesis (Johnston et al. 1999). Similar to the *Minute* case, the Heterozygous *Myc* mutant cells are viable, but eliminated under condition confronting with wild-type cells (Johnston et al. 1999). Moreover, in contrast, wild-type cells are eliminated if they are surrounded by cells expressing higher levels of *Myc* than wild-type cells (de la Cova et al. 2004; Moreno and Basler 2004). In this case, unfit cells are no longer outcompeted, as wild-type cells rather become losers, contrary to the classical type of cell competition, in which wild-type cells eliminate unfit cells (*M/+*) and become winners. For this reason, Myc is considered as super-competitors (Moreno and Basler 2004). This finding of super-competition further supported the concept of cell competition, a mechanism that comparing relative fitness levels, rather than absolute one. Subsequently, the *myc*-induced cell competition has been shown to be conserved in early mouse embryos (Clavería et al. 2013; Sancho et al. 2013), demonstrating that cells with lower levels of *Myc* were eliminated in mosaic mouse embryos. Importantly, Clavería and Sancho showed that endogenous cell death occurs in the mouse embryo through differential expression of *Myc*, providing the first evidence that cell competition functions in normal development. Additionally, the similar function of Myc has been shown in adult mouse cardiomyocytes (Villa del Campo et al. 2014), indicating that cell competition is not restricted to development, but occurs in adult life.

The study of *Minute*- and *Myc*-induced cell competition suggested that the differential growth caused by a difference in translational activity involves in loser cell apoptosis. The role of differential growth for cell competition was demonstrated by showing that *Minute*- induced cell competition was suppressed in starved flies. This was suggesting that the suppression of growth advantage of wild-type over *M/+* by starvation was sufficient to stop cell competition (Simpson 1979). Additionally, the fact that cell competition does not occur after developmental growth ceases support for the role of differential growth (Simpson and Morata 1981). While not all of the competition scenarios associate with differential growth (see last paragraph in this section), it has been considered as a key contributor to cell competition.

Another example of cell competition associating with differential growth is driven by Hippo pathway, which has emerged as a conserved key regulator of growth. The components of Hippo pathway are Hpo/Mst and Wts/Lats (core kinases), and Sav and Mats/Mob (adaptors), which prevent the nuclear accumulation of the transcriptional cofactor Yki/Yap. Repression of Hippo pathway drives Yki/Yap accumulation in nuclei and promotes the expression of multiple targets (i.e., cyclin E, IAPs), leading to promotion of cell proliferation and suppression of apoptosis. Similar to *Myc* overexpressing cells, such overgrowing cells with Hippo pathway deficiency, or cells overexpressing Yki act as super-competitors, which eliminate their surrounding wild-type cells by inducing apoptosis. As Yki up-regulates transcription of *Myc* (Neto-Silva, de Beco, and Johnston 2010; Ziosi et al. 2010), some part of cell competition driven by Hippo pathway is mediated by Myc. Indeed, Myc down-regulation in Yki-overexpressing clones suppress their super-competitive behavior (Neto-Silva et al. 2010; Ziosi et al. 2010). Yet, Hippo-dependent competition is not fully explained by Myc regulation, because Myc overexpression does not rescue the elimination of Yki mutant clones (Ziosi et al. 2010). Moreover, there is an additional key difference in macroscopic appearance between Hippo- and Myc-induced cell competitions. Myc-induced cell competition does not change final tissue size, whereas Hippo-induced competition does change and overcome organ size control (Vincent, Fletcher, and Baena-Lopez 2013). This difference might be due to Hippo pathway regulating contact inhibition, which is a mechanism to terminate growth at target size of organs (Gumbiner and Kim 2014). Therefore, some part of Hippo-induced competition is mediated by Myc, but it constitute other mechanisms.

In earlier examples, growth difference is always associated with cell competition. There are however, exceptions to this rule. Ectopic induction of hyper-proliferating clones, which activate insulin pathway (an effector of the insulin growth pathway; (Böhni et al. 1999)) or overexpress cell cycle regulators (Cyclin D and Cdk4), promotes growth activity, however, does not lead to elimination of surrounding cells (de la Cova et al. 2004). Additionally, cell competition occurs even in post-mitotic follicle cells in the adult *Drosophila* ovary (Tamori and Deng 2013). These findings indicate that growth difference does not always drive elimination of losers. Yet, we still do not know why most of the cell competition winners show higher growth activity than losers, and the role of growth difference in cell competition. Based on a recent finding that differential growth induces mechanical stress and eliminate slower proliferating cells during Ras^{V12}-induced competition (Levayer, Dupont, and Moreno 2016), differential growth would not be a general, but a parallel mechanism of cell competition (See Section 1.9.3 for the contribution of tissue mechanics in cell competition).

1.8.2. Cell polarity

Mutant cells for apico-basal determinants, Scribble (Scrib), Lethal giant larvae (Lgl) and Discs large (Dlg) have been linked to cell competition. In homotypic environment, these mutant cells are viable and proliferate indefinitely until forming a multilayered and massive neoplastic tumors with exhibiting Yki up-regulation (Bilder 2004; Chen et al. 2012; Doggett et al. 2011; Grzeschik, Parsons, Allott, et al. 2010; Sun and Irvine 2011). By contrast, in heterotypic environment, in which mutant cells are surrounded by wild-type cells, they become losers and eliminated by suppression of Yki activity through activation of Jun N-terminal kinase (JNK) signaling (Brumby 2003; Chen et al. 2012; Froldi et al. 2010; Grzeschik, Parsons, and Richardson 2010; Igaki et al. 2009; Menéndez et al. 2010; Ohsawa et al. 2011; Tamori et al. 2010). Other factors associating with polarity are also related to cell competition. Mutant cells with Mahjong (Mahj; a binding partner of Lgl) are eliminated through JNK-induced apoptosis as they confront with wild-type cells. Additionally, cells overexpressing the apical determinant Crumbs (Crb) were also eliminated by apoptosis when surrounded by wild-type cells, whereas *crumbs* mutant cells turn to become super-competitor and induce apoptosis of surrounding wild-type cells (Hafezi, Bosch, and Hariharan 2012).

In contrast to original cell competition (Minute- and Myc-induced competition; see Section 1.8.1), this type of competition derived from polarity defects is not a consequence of growth difference, because polarity-deficient loser cells are eliminated despite their tumorigenic potential with faster proliferation. Moreover, apoptosis of *lgl* mutant cells has been observed even when their growth was induced by Yki or Ras activation (Menéndez et al. 2010). Thus the mechanisms leading to cell competition are different from the original one.

1.8.3. Steep differences in signaling activity to affect survival factors

Cell competition has been shown to occur downstream of many different signaling pathways, leading to proposal of conserved signaling pathways to act as "survival factors", which determine cell survival depending on their dose; Such factors are essential for cells to stay alive, and cause death as being deprived of them. Those factors include BMP/Dpp, WNT/Wingless (Wg), JAK-STAT, and Ras/Raf/MAPK pathways.

For BMP/Dpp morphogen, which regulates growth and patterning (Hamaratoglu, Affolter, and Pyrowolakis 2014), cells with low levels of BMP/Dpp morphogen are eliminated as losers in *Drosophila* and in mammals (Burke and Basler 1996; Moreno, Basler, and Morata 2002; Sancho et al. 2013). For Another morphogen Wg, which regulates patterning, growth and cell survival (Clevers 2006), Wg-deficient cells become losers, whereas Wg-activated cells become super-competitors and triggers apoptosis in wild-type neighbors in *Drosophila* (Vincent et al. 2011). Similarly, for JAK-STAT pathway, which involves in the regulation of growth and tissue size (Arbouzova 2006; Li 2008), JAK/STAT-deficient cells become losers, whereas JAK/STAT-activated cells become super-competitors and induces apoptosis in surrounding wild-type cells in *Drosophila* (Rodrigues et al. 2012). Additionally, for Ras/Raf/MAPK pathway, which is known as a regulator of cell survival (Molina and Adjei 2006), MAPK signaling deficient cells are eliminated by wild-type neighbors, whereas cells expressing activated form of Ras produces super-competitors and eliminate their adjacent wild-type cells in *Drosophila* (Karim and Rubin 1998; Prober and Edgar 2000). These studies suggest that signaling pathway regulating survival factors are required for cell competitiveness.

1.9. Factors to determine cellular fitness

As described in the previous section 1.8, cell competition could be induced by many inputs, however, the output characteristics are similar. This is suggesting that the different signals share some common ground mechanisms. Here I describe the three proposed models to account for the context-dependent competition scenario: Ligand capture model (Section 1.9.1), Fitness comparison model (Section 1.9.2), and Mechanical model (Section 1.9.3).

1.9.1. Ligand capture model: Competition for survival factors

Ligand capture model hypothesize that cells are competing for the amount of secreted molecules required for their survival (namely, “survival factors”) (Raff 1992). If a cell has more receptors or high endocytosis rate, it capture higher amount of the factors, leading to killing the neighboring cells due to restriction of the factor to access. In the case of cell competition in *Drosophila* wing disc, Dpp ligand is proposed to play a role for the survival factor. This hypothesis was first suggested from the observation that loser cells of Minute- and Myc-induced competition show lower levels of Dpp signaling (Moreno and Basler 2004; Moreno et al. 2002; Tyler et al. 2007) and the elimination of losers can be rescued by the activation of the signaling pathway (Moreno and Basler 2004; Ziv et al. 2009). There is, however, some debates for this hypothesis due to some contradictory observations (see detailed debates for the reviews (Amoyel and Bach 2014)), suggesting the involvement of some other survival factors and/or other mechanisms for the context-dependent cell competition.

1.9.2. Fitness comparison model

The alternative model hypothesizes that cells compare their relative fitness levels by using secreted or membrane proteins as “fitness markers”. While it has not been identified the marker protein that functions universally in different kinds of competition scenario, some responsible molecules have been gradually apparent.

One of such marker proteins is transmembrane calcium channel Flower, which was identified by expression profiling analysis in Myc-dependent competition (Rhiner et al. 2010). Flower encodes three different splice isoforms, Flower$^{\mathrm{Ubi}}$, Flower$^{\mathrm{loseA}}$ and Flower$^{\mathrm{loseB}}$. Ubiquitous form *flower*^{Ubi} is expressed throughout normal tissue but down-regulated in losers during competition. In contrast, the other isoforms, *flower*^{loseA} and *flower*^{loseB}, are detected only in losers. The expression of *flower*^{lose} is required and sufficient for loser elimination. Importantly, this expression pattern of distinct isoforms was observed in competition induced by Myc, Minute, scribble mutant, and Dpp pathway. Additionally, the same expression profiling analysis revealed another marker for multiple types of losers, Sparc, which is a secreted extracellular matrix protein (Portela et al. 2010). Contrary to Flower$^{\mathrm{lose}}$, Sparc upregulation in losers protects them against apoptosis. These results suggest that the decision of loser elimination was tightly regulated by balancing the expression levels of proteins with opposite functions (pro-apoptotic vs protective).

Another proposed fitness marker protein has been identified by focusing on the conceptual similarities between innate immunity and cell competition (Meyer et al. 2014). In *Drosophila*, Toll and immune deficiency (IMD) signaling pathways govern the innate immune system to recognize pathogens as non-self. Interestingly, the pathways also mediate the recognition and elimination of loser cells during cell competition. In both of the widely studied two models of cell competition, Myc- and Minute-induced cell competition, Toll-related receptors (TRRs) and extracellular ligand Spätzle involve in the elimination of losers to induce NFκB transcription factor-dependent activation of pro-apoptotic genes. Moreover, the combination of signaling modules are different in accordance with two distinct types of competition. In Myc-induced competition, four of the nine TRRs encoded in *Drosophila* (Toll-2, Toll-3, Toll-8, Toll-9) and a NFκB factor (Relish) are required for loser elimination, whereas in Minute-induced competition, only two of TRRs (Toll-3, Toll-9) and NFκB factors (Dorsal and Dif) are required. Those results indicate that ancient innate immune defense response is adopted for measurement of internal tissue fitness during competition.

For tumor-suppressive cell competition induced by polarity-deficient cells, cell-surface ligand-receptor system was shown to function as fitness marker (Yamamoto et al. 2017). When wild-type winner cells encounter with polarity-deficient loser cells, the winners re-localize the ligand Sas to the lateral cell surface, which is normally localized at the apical surface of epithelial cells (Schonbaum et al. 1992). On the other hand, losers re-localize the receptor PTP10D to the lateral surface, which is also normally localized at the apical surface of epithelial cells. This lateral accumulation of Sas and PTP10D drives trans-activation of Sas-PTP10D signaling and leads to suppression of EGFR signaling in loser cells. This EGFR signaling suppression enables to activate JNK signalling in the loser cells to drive cell elimination. In contrast, in the absence of the Sas-PTP10D signaling, the elevated EGFR signaling cooperates with JNK signaling to inactivate Hippo pathway, leading to overgrowth of the polarity-deficient cells.

1.9.3. Mechanical model

The alternative possible mechanism of fitness sensing is triggered by mechanical stress. The model was first proposed from the study using a mathematical model, which suggested that mechanical stress induced by heterogeneous growth could feedback on the rate of cell division and apoptosis (Shraiman 2005): compression of slower dividing cells adjacent to faster dividing cells would trigger apoptosis during cell competition. Such mechanical effects on the elimination of cells from epithelia are experimentally observed in a non-competitive situation. In pupal notum of *Drosophila*, tissue overcrowding by proliferation induces cell delamination, which buffers epithelia against growth variation (Marinari et al. 2012). Another experimental observations in human, canine and zebrafish cells also show that extrusion occurs as a consequence of overcrowding (Eisenhoffer et al. 2012). These studies in a non-competitive situation was suggested that mechanical state of cells could be an important contributor to cell competition. Indeed, more recently, it has been shown that over-proliferation induced by activation of oncogenic *Ras* induces crowding into their surrounding wild-type cells, which results in death of the crowded cells (Levayer et al. 2016). Additionally, mechanical stress-induced cell competition has been reported in the competition between wild-type and *Scribble* knockdown cell population (Wagstaff et al. 2016). They showed in Madin-Darby canine kidney (MDCK) cells that *Scribble* knockdown cells are hypersensitive to cell compaction, and crowding induced by interaction with wild-type cells is sufficient to eliminate the *Scribble* knockdown cells. Thus, mechanical model could function as an alternative mechanism for eliminating less-fit cells during cell competition.

1.10. Role of cell competition in tissue homeostasis and tumor promotion

Cell competition is widely conserved between invertebrates and mammals. This suggests that the ability of cells for sensing the relative fitness is relevant to several fundamental physiological processes. One of the proposed roles of cell competition is tissue size control, because tissue final size undergoing *Minute*- and *Myc*-induced cell competition was not affected and was similar to control tissue size (de la Cova et al. 2004; Morata and Ripoll 1975). Indeed, inhibition of apoptosis in *Drosophila* wing tissue does not affect mean of the wing size, however, it leads to greater variability in wing size (de la Cova et al. 2004). This suggests that fixed size of final tissue is obtained by balancing the rate of growth and apoptosis through cell competition.

Another role of cell competition for ensuring tissue homeostasis is tumor suppression by eliminating the potentially cancerous cells as losers. This is applicable to the case of competition driven by polarity deficiency, in which wild-type cells eliminate oncogenic potential cells (Brumby 2003; Chen et al. 2012; Froldi et al. 2010; Grzeschik, Parsons, and Richardson 2010; Igaki et al. 2009; Menéndez et al. 2010; Norman et al. 2012; Ohsawa et al. 2011; Tamori et al. 2010). Because the polarity deficient cells have the ability to overgrowth and form a precancerous field in the absence of cell competition, the cell competition mechanisms to eliminate the abnormal cells would suppress tumorigenesis.

Contrary to these homeostatic functions, there is potentially a dark side of cell competition: If abnormal cells acquire a higher fitness than wild-type cells, they could eliminate wild-type neighbors, resulting in the promotion of tumor expansion rather than suppression. This paradigm is applicable to super-competition, where wild-type cells are killed (de la Cova et al. 2004; Moreno and Basler 2004; Rodrigues et al. 2012; Tyler et al. 2007; Vincent et al. 2011; Ziosi et al. 2010). Indeed, *myc*, a factor of inducing super-competition, has been shown to be frequently overexpressed in human cancers (Pelengaris, Khan, and Evan 2002). In addition, activity of Hippo pathway is also frequently deregulated in different human cancers (Harvey, Zhang, and Thomas 2013). The altered expression and regulation of these super-competitors in cancers suggest that super-competition can contribute to cancer progression. Additionally, super-competition has been also proposed to contribute to field cancerization (Rhiner and Moreno 2009), clinical observation in which multiple tumor foci appears within the same tissue (Slaughter, Southwick, and Smejkal 1953). Taken together, the fitness comparison mechanisms not only ensure tissue homeostasis, but also promote tumorigenesis when the mechanisms are hijacked by abnormal cells. Thus, the revealed insights of key parameters for cell competition help understanding many aspect of physiological processes, and provide therapeutic strategies for pathological development.

1.11. Aim of this thesis

The aim of this thesis is to understand how the cell-level behaviors (cell division, death, migration) influence on the physiological phenomenon observed at cell-population levels from a view point of tissue mechanics. In general, there are gaps between cell- and tissue-level behaviors *in vivo*, because many cell-level behaviors are entangled in a complex manner and produce tissue-level behaviors. In contrast to the *in vivo* case, theoretical model has advantage to separately control individual parameters of cell behaviors. Hence, in this thesis, I combined *Drosophila* experiments and cell vertex model simulations to study cell heterogeneity caused by difference in mechanical tension or cell growth. The *in silico* predictions and *in vivo* verifications are linked by quantitative analysis so as to provide the mechanistic ground of the cell behavior under heterogeneous population in a synergistic manner. In chapter 2, I present the competitive cell interactions leading to disruption of tissue homeostasis. In chapter 3, mechanical basis contributed to clone shape of distinct genotypes is identified by developing a pipeline to infer cell mechanics.

2. Competition for space controlled by apoptosis-induced change of local epithelial topology

Some experimental figures in this chapter (Fig. 2.1a, 2.2a', Fig. S2.1, S2.4d) were obtained in collaboration with my colleagues, Y. Sando and D. Umetsu. I clarified my own contribution in each caption.

2.1. Abstract

During the initial stage of tumor progression, oncogenic cells spread despite spatial confinement imposed by surrounding normal tissue. This spread of oncogenic cells (winners) is thought to be governed by selective killing of surrounding normal cells (losers) through a phenomenon called "cell competition" (i.e. supercompetition). Although the mechanisms underlying loser elimination are increasingly apparent, it is not clear how winner cells selectively occupy the space made available following loser apoptosis. Here, I combined live imaging analyses of two different oncogenic clones (Yki/YAP-activation and Ras-activation) in the Drosophila epithelium with computer simulation of tissue mechanics to elucidate such a mechanism. Contrary to the previous expectation that cell volume loss after apoptosis of loser cells was simply compensated for by the faster proliferation of winner cells, I found that the lost volume was compensated for by rapid cell expansion of winners. Mechanistically, the rapid winner-dominated cell expansion was driven by epithelial junction remodeling following apoptosis, which causes re-connection of local cellular connectivity (cell topology) in a manner that selectively increases winner apical surface area. In silico experiments further confirmed that repetition of loser elimination accelerates tissue-scale winner expansion through topological changes over time. The proposed mechanism for linking loser death and winner expansion provides a new perspective on how tissue homeostasis disruption can initiate from an oncogenic mutation.

2.2. Introduction

Primary tumors originate from a single transformed cell containing oncogenic mutations despite being spatially confined by surrounding normal tissue. It is increasingly apparent that oncogenic cell spread within tissue is driven not only simply by a higher rate of proliferation, but also by a phenomenon called "cell competition" (Eichenlaub et al. 2016; Suijkerbuijk et al. 2016). Cell competition is a process in which "winner" cells (e.g., certain oncogenic mutant cells) induce apoptosis in neighboring "loser" cells (e.g., normal host cells), and thus spread their territory (Eichenlaub et al. 2016; Johnston et al. 1999; de la Cova et al. 2004; Levayer et al. 2016; Moreno and Basler 2004; Suijkerbuijk et al. 2016; Tyler et al. 2007). Because inhibiting loser apoptosis is sufficient to halt winner spread

(Eichenlaub et al. 2016; Li and Baker 2007; Martin, Herrera, and Morata 2009; Moreno and Basler 2004; Suijkerbuijk et al. 2016), loser apoptosis seems to play an active role in promoting winner spread within the tissue. However, it is unclear how loser apoptosis impacts surrounding cells to produce selective occupation by winner cells.

Cell competition can be considered as processes of destruction (loser apoptosis) and reconstruction (winner takeover) of the epithelial tissue structure (Bove et al. 2017; Clavería et al. 2013; Eichenlaub et al. 2016; Igaki et al. 2009; Johnston et al. 1999; Kajita et al. 2014; de la Cova et al. 2004; Levayer et al. 2016; Levayer, Hauert, and Moreno 2015; Li and Baker 2007; Li, Kale, and Baker 2009; Martin et al. 2009; Moreno and Basler 2004; Ohsawa et al. 2011; Simpson 1979; Simpson and Morata 1981; Suijkerbuijk et al. 2016; Tyler et al. 2007; Wagstaff et al. 2016; Yamamoto et al. 2017). Epithelial tissue consists of a sheet of tightly packed cells connected with adhesive junctions. This local cell-cell connectivity ("cell topology" (Farhadifar et al. 2007; Gibson et al. 2006)) is represented by a distribution of the number of sides (adherent neighbors) of each cell. Because the side number positively correlates with the apical surface area (known as Lewis's law conserved in epithelial tissue (Farhadifar et al. 2007; Lewis 1928)), topological change is associated with cellular expansion or contraction. In the case of cell competition, apoptosis could change the topology of neighboring cells through cell delamination or extrusion, which is followed by consecutive junctional remodeling (cell intercalation) between a dying cell and its surviving neighbors (Levayer et al. 2016; Marinari et al. 2012). Topological change driven by loser apoptosis might therefore allow winner cells to spread with increasing their side number. This idea prompted us to investigate whether cell topology changes in the vicinity of apoptotic cells contribute to winner takeover during competition.

Using generalized mechanical simulations and *in vivo* imaging of *Drosophila* oncogenic clones, I show when and how winner cells selectively expand to compensate for local tissue volume loss after apoptosis of a loser cell. Following induction of locally overgrowing winners, slowly dividing normal cells adjacent to rapidly dividing winners show anisotropic distortion, as reported previously (Legoff, Rouault, and Lecuit 2013; Mao et al. 2013; Pan et al. 2016; Vincent et al. 2013). Immediately following apoptosis of the anisotropic normal cell, the space previously occupied by the apoptotic loser cell was filled by rapid cell expansion of adjacent winner cells. The winner cell expansion was unexpected, because previous studies mostly focused on cell division as the compensatory mechanism to fill space (e.g. "compensatory proliferation") (Di Gregorio, Bowling, and Rodriguez 2016; Levayer and Moreno 2013; Li et al. 2009; Pellettieri and Alvarado 2007; Tamori and Deng 2011). As a mechanism underlying this compensatory cell expansion of winners, I found that apoptosis of anisotropic losers adjacent to winners causes directionally biased cell intercalations, which re-establishes local cellular connectivity (cell topology) in a manner that selectively increases the apical surface area of winners. Importantly, such topological dynamics were verified with *in silico* and *in vivo* experiments in two different oncogenic genotypes (activated-Yki and Ras), where the over-proliferating population triggers apoptosis in surrounding cells with slower proliferation. Furthermore, repetition of topological changes through the apoptosis of losers in immediate contact with winners, as observed in many cell competition systems (Amoyel and Bach 2014), accelerates the tissue-scale expansion of winners *in silico*. Such rapid cell turnover via topological changes may disrupt tissue homeostasis to facilitate tumor initiation.

2.3. Material and Methods

2.3.1. Drosophila strains and genetics

Strains used for imaging fluorescently-labeled mitotic clones (Lee and Luo 1999; Xu and Rubin 1993) in fixed larval imaginal discs (Fig. 2.1a–c, S2.1h–i'): *ubxFLP; Act>y*$^{+}$*>Gal4, UAS-GFP; FRT82B, Tub-Gal80* (82B tester), *ubxFLP; FRT42D, Tub-Gal80; Act>y*$^{+}$*>Gal4, UAS-GFP* (42D tester), *ubxFLP; Tub-Gal80, FRT40A; Act>y*$^{+}$*>Gal4, UAS-GFP* (40A tester). Additional strains used were as follows: *wts*^{X1} (from T. Xu), *hpo*$^{42\text{-}47}$ (from D.J. Pan), *UAS-sqh-RNAi* (Bloomington Stock Center 32439), *UAS-shg-RNAi* (Vienna Drosophila Resource Center #27081). Strains used for notum live imaging (Fig. 2.2, 2.4, 2.5, S2.1, S2.4): *y, w, hs-flp; DE-Cad::GFP; Act>CD2>GAL4, UAS-CD8.mCherry, P{tubP-GAL80ts}20* (Bloomington Stock Center 7019), *UAS-Yki:V5*^{S111A,S168A,S250A} (Bloomington Stock Center 28817), *UAS-Ras*^{V12} (from T. Xu).

2.3.2. Immunohistochemistry and fixed-sample imaging

Cross and offspring were kept at 25°C until dissection. Larval tissues were stained with standard immunohistochemical procedures using rat anti-*Drosophila* E-cadherin antibody DCAD2 (Developmental Studies Hybridoma Bank (dshb.biology.uiowa.edu), 1:20) and Alexa 647-conjugated phalloidin (Molecular Probes, 1:50). Specimens were mounted with 4',6-diamidino-2-phenylindole (DAPI)-containing SlowFade Gold Antifade Reagent (Molecular Probes). Images were taken on Leica TCS-SP8 or Zeiss LSM700 confocal microscopes. Images shown in Fig. 2.1a, S2.1h, i are sum projections.

2.3.3. Calculation of cell shape anisotropy

To evaluate cell shape anisotropy, I used two calculation method, "cell anisotropy" and "clone-boundary-oriented cell anisotropy". Cell anisotropy was calculated from the inertial tensor of each cell using the positions of the vertices (Fletcher et al. 2013). The anisotropy α_i of a cell *i* is represented by the length of long axis *l* and short axis *s* calculated from the eigenvalues of the tensor:

$$\alpha_i = \frac{l-s}{l+s} \qquad \text{Eq. (2.1)}$$

Clone-boundary-oriented cell anisotropy c_i of a cell *i* is represented by the product of cell anisotropyα_i (Eq. 2.1) and cosine θ_j, angle of its long axis relative to the clone boundary edges *j*:

$$c_i = \alpha_i < cos2\theta_j >_j \qquad \text{Eq. (2.2)}$$

where $< >_j$ denotes the average for all boundary edges belonging to cell i.

2.3.4. Analysis of cell area and shape in fixed-sample imaging

Positions of vertices (junctions) of wild-type cells located at the clone boundary were manually extracted with ImageJ or Fiji. Because epithelial cells in the wing disc are columnar in shape, each vertex was measured at the focal plane of the apical surface, identified by anti-E-cadherin or phalloidin staining. The cell area was calculated from the positions of the vertices by considering a cell a polygon. Strength of cell shape anisotropy was calculated using Eq. 2.1 (Fig. 2.1a, b, S2.1h', i').

2.3.5. Live imaging of pupal notum

Live imaging was performed in the pupal notum rather than the wing disc because the notum does not require *ex vivo* cultivation and is easy to handle. Cross and offspring were kept at 18°C for 7–9 days and then subjected to heat shock at 33°C or 34°C for 30 minutes to induce somatic clones. Larvae were then kept at 18°C. 78.5–81.5 hours or 94–98 hours after heat shock, white prepupae (WPP) were collected. Collected WPPs were switched to 29°C to express the *UAS-Yki:V5*^{S111A,S168A,S250A} transgene, while WPPs were raised for 8 hours at 18°C and switched to 29°C to express the *UAS-Ras*^{V12} following earlier studies (Levayer et al. 2016). The pupae were then imaged at 29°C between 15.5–33.5 hours (Yki) or 16–27 hours (Ras^{V12}) after temperature shift. Pupae for image acquisitions were prepared using a modified previously described protocol (Koto, Kuranaga, and Miura 2009) or (Umetsu, Aigouy, et al. 2014). The pupal case of the staged pupae was carefully removed at the top of the notum. The exposed notum was placed directly on a coverslip and imaged. The nota close to the scutum region were taken on Leica TCS SP5 or SP8 confocal laser scanning microscopes. Z-stacks (0.8 µm/slice) were taken every 4 minutes. Images shown in Figs. 2.2a, a', b, 2.4c, 2.5c, S2.4d, e were maximum projections. For Fig. 2.2a' and S2.4d, the maximum projection was performed by subdividing the picture in 256×256-pixel windows to avoid reflecting cuticle wrinkles in the projected image. Tissue-scale images shown in Fig. 2.2a, a', 2.4c, S2.4d were processed through the subtract background function in Fiji.

2.3.6. Cell delamination analysis in live imaging

Temporal change in cell area for apoptotic cells and surrounding cells (Fig. 2.2, 2.4, 2.5, S2.4) was quantified by segmentation in Fiji plugin Tissue Analyzer (Aigouy et al. 2010; Aigouy, Umetsu, and Eaton 2016). When cells surrounding a dying cell were delaminated or underwent mitosis during quantification (40 minutes before until 24 minutes after delamination complete), the contribution of a single apoptotic event on the captured area of surviving neighbors cannot be precisely determined; therefore, I excluded the apoptosis event from the quantification analysis. I also exclude apoptosis inside of the midline [inside of the two most central lines of sensory organ precursors (SOP)], where spontaneous cell delamination occurs independently of cell competition. Cell anisotropy (Fig. S2.4a, b, c, g) was calculated using Eq. 2.1. Clone-boundary-oriented cell anisotropy (Fig. 2.2g–h', 2.5a', a'', d', d'', S2.4g') was calculated using Eq. 2.

The normalized frequency of each type of intercalation (Fig. 2.5d'–g', d''–g'') was obtained by dividing the number of occurrences of each intercalation type by the total number of intercalations during a single apoptosis event (Fig. 2.5b). When multiple intercalations (T1 transition) and/or T2 transition take place at a time (during a single time interval: 4 minutes), the type of cell intercalations were distinguished by estimating intercalated edges from the arrangement of cell neighbor relations. When more than two types of edges are estimated, the probability for occurrences for each intercalation type was calculated as n/n_{ALL} (n: number of estimated edges for a given intercalation type, n_{ALL}: total number of estimated edges). See Fig. S2.4e–f for details. Note that, when additional intercalations were observed soon after apoptosis (from 16 to 24 minutes after delamination complete), the cell topologies were not stably determined; therefore, the apoptosis events from the current intercalation analysis were excluded.

2.3.7. Analysis of cell shape, topology, and delamination in live imaging

Clonal cells were identified in the Tissue Analyzer and projected onto the segmented image (Fig. 2.2a, a', 2.4d, S2.4d). Cell anisotropy (Fig. 2.2a, a' right, "cell-stretch" in "Viewer" tab), side number (Fig. 2.4e, S2.4d, "packing-no cutoff" in "Viewer" tab) and cell area (Fig. 2.4f, S2.4d, "image color coder" in "Misc" tab) were visualized by Tissue Analyzer. For the plots of normalized area as a function of side number (Fig. 2.4g, S2.4d'), SOPs and their primary neighbors and pupal midline region were excluded from the data. In addition, I did not plot data points when the sample number was less than 10. Note that the definition of cell anisotropy in Fig. 2.2a, a' (see (Aigouy et al. 2010)) is different from the one shown in Fig. S2.4a, b, c, g (see Eq. 2.1) and Fig. 2.2h, h', 2.5a', a'', d', d'', S2.4g' (see Eq. 2.2).

2.3.8. Statistical analysis

Scatter plots: Error bars represent standard deviation (s.d.) or standard error (s.e.) of the mean as specified in figure legends. Box plots: The upper/lower hinge and middle line represent the 25th/75th and 50th percentiles ("boxplot" function in R environment). Statistical test: Fisher's exact test (two-sided), Wilcoxon rank sum test (two-sided), Wilcoxon signed rank test (two-sided), Welch's t-test (two-sided, normality and homoscedasticity were tested by Kolmogorov-Smirnov test and F-tests, respectively). Smirnov-Grubbs testing was performed to detect outliers (P-values $< 10^{-4}$). Correlation coefficients and significance test were based on Pearson's product-moment correlation coefficient. All calculations and plots were performed with Microsoft Excel or R environment.

2.3.9. Vertex model formulation

The cell-vertex model quantitatively accounts for the packing geometry of normal epithelial cells and predicts the forces that act at cell-cell interfaces, where cell configurations are described as polygons whose vertices form tricellular junctions that are subject to mechanical force (Farhadifar et al. 2007; Gibson et al. 2011; Honda 1983). Cells change their shape based on the force balance of cell packing. The primary model used here is represented by the ordinary differential equations of the position vector of each vertex (Gibson et al. 2011):

$$\frac{d\vec{x_i}}{dt} = F_{tension} + F_{pressure} = \sum_{<j\in E(i),\ \alpha\in F(i)>} \left(G_{ij}(d_{ij} - l_0) + \frac{n_H d_{ij}}{A_\alpha}\right) \qquad \text{Eq. (2.3)}$$

E(i) is the set of edges incident to vertex *i*, and *F(i)* is the set of faces to which vertex *i* belongs. The tensional force $F_{tension}$ is exerted to a vertex *i* by the connecting edges between vertices *i* and *j*, where the edge length d_{ij} converges to the preferred length l_0. The internal pressure $F_{pressure}$ is exerted on a vertex *i* by the cell face *α* to which a vertex *i* belongs, where $F_{pressure}$ increases as the area of cell *α* (A_α) decreases and the edge length (d_{ij}) increases. The magnitude of $F_{tension}$ and $F_{pressure}$ are controlled by the parameters G_{ij} and n_H, respectively. For all figures in this paper, except for Fig. S2.1f, g, S2.3a–f, i (examining the parameter dependency) and Fig. S2.2 (using the other model formulation), the parameter values were set at $G_{ij} = 5$, $l_0 = 0.0001$, and $n_H = 1$. The parameter accounted for cell packing geometry in *Drosophila* (Fig. S2.1a, b), and did not dramatically affect the emergence of cell deformation due to differential proliferation rates (Fig. S2.1f, g, S2.3a–b) or asymmetric area expansion induced by apoptosis (Fig. S2.3c, e, i).

To test validity of the numerical results independent of the model details, I also examined another vertex model (Farhadifar et al. 2007) assuming three types of forces, $F_{area\ elasticity}$, $F_{tension}$, and $F_{contractility}$:

$$\begin{cases} \dfrac{d\vec{x}_i}{dt} = F_{area\ elastisity} + F_{tension} + F_{contractility} = -\dfrac{\partial E}{\partial \vec{x}_i} \\ \qquad E = \frac{1}{2}\sum_\alpha (a_\alpha - 1)^2 + \bar{\Lambda}\sum_{<i,j>} l_{ij} + \frac{\bar{\Gamma}}{2}\sum_\alpha {l_\alpha}^2 \end{cases} \qquad \text{Eq. (2.4)}$$

The area elasticity $F_{area\ elasticity}$ is exerted on a vertex *i* by the face *α* to which a vertex *i* belongs, where area of cell *α* (a_α) approaches the normalized preferred area of unity. The tension $F_{tension}$ is exerted on a vertex *i* by the connecting edges between vertices *i* and *j*, where $F_{tension}$ increases as the edge length between vertices *i* and *j* (l_{ij}) increases. The contraction $F_{contractility}$ is exerted to a vertex *i* by the contractility of cell perimeter l_α, which is provided by actomyosin contractile force. The parameters were set to $\bar{\Lambda} = 0.06$ and $\bar{\Gamma} = 0.02$ (Fig. S2.1a, b, and S2.2).

Both models (Eq. 2.3 and Eq. 2.4) were integrated numerically using the Euler method with free boundary conditions. To achieve a mechanical equilibrium of tissue state, the position vector of each vertex was calculated after each step until the total velocity of all vertices dropped below a threshold of 1.0. Cell intercalation was incorporated when edges with a length below the threshold 0.001 were maintained for 8.3×10^{-4} normalized time [/loser cell cycle], noting that the intercalation during apoptotic cell delamination was introduced independent of this rule (see Section “Apoptosis simulations”).

2.3.10. Proliferation in simulations

Each cell divides when the residence time *t* in the cell cycle becomes zero. Total duration of cell cycle obeys gamma distribution with the following probability densities:

$$p(t) = t^{k-1}\frac{\exp(-\frac{kt}{\bar{T}})}{(\bar{T}/k)^k\Gamma(k)} \qquad \text{Eq. (2.5)}$$

where $\Gamma(k)$ is the gamma function with k = 25.0, following an earlier report (Wartlick et al. 2011). The average and the standard deviation are given by $\bar{T}$ and $\bar{T}/\sqrt{k}$, respectively, with $\bar{T}$ = 6 for slower dividing cells ($\overline{T_{slow}}$). In case of the differential proliferation, the average cell cycle of slower dividing cells ($\overline{T_{slow}}$) divided by that of faster dividing cells ($\overline{T_{fast}}$) represents a ratio of the division rates of clones (i.e., $\overline{T_{slow}}/\overline{T_{fast}}$). The simulation time is represented in normalized time [/loser cell cycle], which is divided by $\overline{T_{slow}}$ (loser cell cycle). Although the cell area decreases to half of the original cell area after cell division, it increases subsequently as the cell achieves mechanical equilibrium, following the model formulations (Eq. 2.3 and Eq. 2.4). The orientation of the mitotic cleavage plane obeys the long axis rule (Gibson et al. 2011), where the plane passing through the shorter axis is defined by calculating inertial tensor of each cell using the position of the vertices (Fletcher et al. 2013).

2.3.11. Apoptosis in simulations

For apoptotic cell delamination, several cell intercalation (T1) events were introduced sequentially (Levayer et al. 2016; Marinari et al. 2012) to incorporate the loss of junctional neighbors (1 intercalation / 1.7×10^{-3} normalized time [/loser cell cycle]). As the apoptotic cell becomes triangular in shape, it is eliminated by the T2 transition (Farhadifar et al. 2007; Honda 1983**).** The intercalation was preferentially introduced on the shorter edge of the apoptotic cell, following the probability P_i (except for Fig. 2.6b and Fig. S2.6b, b’):

$$P_i = \frac{e^{-\beta l_i}}{\sum_j e^{-\beta l_j}} \qquad \text{Eq. (2.6)}$$

where l_i and β are the length of edge i and a parameter, respectively. The denominator is a normalization factor of summation of every edge j in an apoptotic cell. P_i for each edge was recalculated at every time before intercalation. The parameters were set to β = 10 for (Eq. 2.3; except for Fig. 2.7, randomized intercalation) and β = 9.4 for (Eq. 2.4) to ensure equal probability between of two formulations. For randomized intercalation in Fig. 2.7, I set β = 0 to provide the same probability for any edge with variable length. Vertex model parameters (G_{ij} and n_H in Eq. 2.3) during the delaminating process were kept constant (delamination type I), except for delamination type II in Fig. S2.3d–f. In delamination type II, apical surface of dying cells shrink rapidly by increasing the line tension parameter G_{ij} (Eq. 2.3) and/or decreasing the pressure parameter n_H (Eq. 2.3) before repeated cell intercalation. For the repetitive induction of apoptosis into multiple loser cells in Fig. 2.7, S2.7, apoptotic cells were randomly selected from a target region of slower dividing cells. A single apoptosis event occurred every five cell divisions in faster dividing clones.

2.4. Results

2.4.1. Differential proliferation induces local anisotropic distortion in slower dividing cells at the clone boundary and compression in faster dividing cells

To examine the cellular interaction during cell competition from a geometric perspective, clones of green fluorescent protein (GFP)-expressing Hippo pathway-mutant cells (winners; *wts*^{X1}) that rapidly proliferate and outcompete surrounding normal cells (losers; wild-type) in *Drosophila* wing discs (Tyler et al. 2007) was induced in collaboration with my colleague, Y. Sando. Quantitative image analysis of apical cell shapes revealed two geometric alterations. First, wild-type cells directly adjacent to *wts*^{X1} clones showed significantly larger anisotropic distortions (Fig. 2.1a, orange) than those directly adjacent to wild-type control clones (Fig. 2.1a, blue and 1b; see Methods for the fly strains and cell anisotropy definition), which was consistent with earlier reports (Legoff et al. 2013; Mao et al. 2013)**.** Second, the apical cell area of *wts*^{X1} clones was smaller than that of wild-type clones (Fig. 2.1c), indicating that Hippo pathway-mutant cells surrounded by wild-type cells are packed at a higher density.

I next examined whether the ectopic induction of over-proliferating cells was sufficient to cause these two geometric alterations (Fig. 2.1b, c) in the vertex model. The vertex model is widely used to study mechanical deformation of multicellular tissue in response to cell bond tension and apical area contraction (Farhadifar et al. 2007; Fletcher et al. 2013; Gibson et al. 2011; Honda 1983; Lee and Morishita 2017) (Eq. 2.3 in Methods, Fig. S2.1a, b). I introduced two clonal cell populations with different division rates into the model (Fig. 2.1d, Fig. S2.1c)**.** I confirmed anisotropic deformation of slower dividing cells localized at the clone boundary (Fig. 2.1d middle, 1e, Fig. S2.1d), which is consistent with the wild-type cells directly adjacent to the *wts*^{X1} clone in the *Drosophila* experiment (Fig. 2.1b) and earlier simulation studies (Mao et al. 2013; Pan et al. 2016). In addition, faster dividing cells were smaller than surrounding slower dividing cells (Fig. 2.1d bottom, 2.1f, Fig. S2.1e), similar to the *wts*^{X1} cells in the *Drosophila* experiment (Fig. 2.1c). These results were consistent irrespective of different mechanical parameter values (Fig. S2.1f, g) or formulations (another often used type Eq. 2.4; Fig. S2.2a–c). These deformations were never observed when two cell populations had identical division rates (Fig. 2.1d, leftmost), and they were more apparent with greater differences in cell division rates (Fig. 2.1e, f). These simulations suggest that differential proliferation rates are sufficient to reproduce two geometrical alterations in the *Drosophila* epithelium (Fig. 2.1b, c).

I also examined the anisotropic cell deformation in the setting of differential tension between clonal and non-clonal cells since juxtaposition of wild-type and aberrant cells often affects junction mechanics (Bielmeier et al. 2016; Bosveld, Guirao, et al. 2016). *In silico* experiments with all tension conditions showed that slower dividing cells at the clone boundary always exhibited higher anisotropy than those with identical proliferation rates (Fig. S2.3a–b), demonstrating that differential tension does not have considerable influence on the cell anisotropy. Consistently, *in vivo* observation showed that the wild-type cell anisotropy beside clone was maintained even under modulation of junction contractility or adhesion in Hippo pathway mutant clones (Fig. S2.1h–i). Collectively, these results suggest that localized over-proliferation induces anisotropic deformation in slower dividing cells at the clone boundary under differential tension.

2.4.2. Winner cells expand into spaces originally occupied by apoptotic loser cells with higher cell anisotropy

Live imaging of cell competition was performed (Bove et al. 2017; Kajita et al. 2014; Levayer et al. 2016, 2015; Ohsawa et al. 2011) in the *Drosophila* pupal notum to examine how space previously occupied by apoptotic loser cells is replaced. I induced faster dividing winner clones overexpressing an activated Yki (*UAS-Yki:V5*^{S111A,S168A,S250A}; hereafter called Yki clones) (Oh and Irvine 2009), a transcriptional co-activator that acts downstream of the Hippo pathway (Fig. 2.2a left). I observed that wild-type loser cells near Yki winner clones progressively took on anisotropic shapes (Fig. 2.2a, right, Fig. S2.1j), especially those between the Yki clones. The wild-type loser cells were subsequently eliminated from the tissue (Fig. 2.2b) by sequential cell intercalations from the shorter edges of a dying cell (Fig. 2.2c, d). Upon repetitive loser apoptosis, compacted Yki winner cells, which might be due to their rapid proliferation, appeared progressively larger. At the level of individual apoptosis, winner cells adjacent to apoptotic cells selectively replaced the space originally occupied by apoptotic loser cells through cell expansion; the area of faster dividing winner cells surrounding a dying cell increased, whereas the change in the area of slower dividing loser cells was negligible (Fig. 2.2e, f). In collaboration with my colleague, D. Umetsu, I examined another oncogenic winner-clone induced by an activated form of Ras (*UAS-Ras*^{V12}), which proliferates rapidly and outcompetes surrounding wild-type cells in *Drosophila* (Karim and Rubin 1998; Levayer et al. 2016). The *Ras*^{V12} winner cells also expanded to compensate for wild-type loser cell apoptosis (Fig. 2.2a’, d’, f’). The compensatory cell expansion of winners following apoptosis was unexpected considering the accepted hypothesis that lost territory is replaced as a result of winner-cell proliferation (Di Gregorio et al. 2016; Levayer and Moreno 2013; Pellettieri and Alvarado 2007; Tamori and Deng 2011). Moreover, I found that the winners’ expansion was mediated by the anisotropic deformation of dying loser cells (Fig. 2.1b); the acquired area of Yki or Ras^{V12} winner cells positively correlated with anisotropy of dying loser cells (Fig. S2.4a, g) that were oriented in parallel to the clone boundary (hereafter I call "clone-boundary-oriented anisotropy"; Fig. 2.2g, h, h', Fig. S2.4g').

I then applied a vertex model to determine whether winners used cell expansion to compensate for the volume lost after apoptosis of anisotropic loser cells. I incorporated apoptosis into the simulation based on the following experimental observations (Fig. 2.2): (1) the target of apoptosis was slower dividing cells directly adjacent to faster dividing clones, (2) dying cell removal was induced by junctional loss due to sequentially introduced cell intercalations (Levayer et al. 2016; Marinari et al. 2012) from the shorter edges of dying cells (Fig. 2.3a, see Methods for the settings to simulate apoptosis). Consistent with the previous experiments, the surrounding winner cells dominated expansion following apoptosis (Fig. 2.3b). This winner-cell expansion was repeatedly observed in independent simulations that separately induced apoptosis in each individual loser cell at the clone boundary under differential proliferation rates (Fig. 2.3c, Fig. S2.5a), but it did not occur in the setting of identical proliferation rates (Fig. 2.3c', Fig. S2.5a). This winner-cell expansion was consistently observed in several different model setups [formulation (Eq. 2.4; Fig. S2.2d), delamination process (Fig. S2.3d–f), and differential tension conditions in clonal and non-clonal cells (Fig. S2.3c)]. Moreover, consistent with *in vivo* experiments, the rapidly dividing winner cells increasingly expanded as clone-boundary-oriented anisotropy of dying loser cells increased (Fig. 2.3d, Fig. S2.2e, e', S2.3g). I note that the rapid proliferation of winners in itself was not directly involved in the compensation process following apoptosis, because winner cells took over the territory of apoptosis despite ceasing all cell proliferation during the apoptotic simulation (Fig. S2.3i). Therefore, I concluded that the emergent property under differential proliferation (i.e., local anisotropic distortion of apoptotic loser cells (Fig. 2.1)), rather than differential proliferation in itself, has a key role in the compensatory expansion of winner cells.

2.4.3. Local topological change near apoptosis accompanies winner-dominated cell expansion

I then focused on cells immediately adjacent to an apoptotic cell to examine their contribution to winner-dominated cell expansion, because the territory lost to apoptosis was primarily occupied by the immediate neighbors, and cells located more than two cell distances away from the apoptotic cell acquired much smaller area (Fig. S2.3h, h'). I initially hypothesized that rapid winner-cell expansion was the result of a local compression difference between winner and loser cells surrounding the apoptosis (compression hypothesis; Fig. 2.4a), because more compressed cells (Fig. 2.1c, f) may generate stronger outward pushing forces that are enough to increase their cell area. To address this hypothesis, I tested whether compressed smaller cells adjacent to apoptosis were more likely to expand than larger cells. This hypothesis, however, seems not to be the case, because I observed that the cell area before apoptosis and their acquired area after apoptosis only correlated weakly, both *in silico* (Fig.

2.4a') and in *in vivo* experiments with Yki and Ras^{V12} (Fig. 2.4a'', a'''). Additionally, in simulation, winner cells still took over the territory of apoptotic losers even if the tissue-scale pushing forces globally generated by release of winner-clone compression was suppressed during apoptosis by reducing the pressure parameter of all cells in winner clone (Fig. S2.3i). These results suggested that local and global compression was insufficient to drive the process of rapid compensatory expansion of winner cells, while winner compression was required for anisotropic deformation of loser cells (Fig. 2.1).

As another hypothesis that locally mediates expansion, I focused on changes in local cellular connectivity (cell topology) driven by junctional remodeling (cell intercalation) upon apoptosis (Fig. 2.2b, 2.3a). In epithelial cells in non-competitive tissue, there is a positive correlation between cell area and the side number representing local cellular connectivity (Lewis's law; Fig. S2.1b) (Farhadifar et al. 2007; Heller et al. 2016; Lewis 1928). Based on this Lewis's law, an increase or decrease of side/edge number in each cell adjacent to apoptosis would be associated with cell area expansion or contraction (topology hypothesis; Fig. 2.4b). I first confirmed that both winner (Yki or Ras^{V12}) and loser (wild-type) cells in competitive tissues obey this law (Fig. 2.4c–g, Fig. S2.4d, d'), similar to non-competitive normal tissue. I then examined the topological changes following apoptosis and found that cells adjacent to apoptosis showed a strong positive correlation between the captured area and change in side number after apoptosis both *in silico* (Fig. 2.4b') and in *in vivo* experiments with Yki and Ras^{V12} (Fig. 2.4b'', b'''). This suggests that cell intercalations during delamination lead to simultaneous increases in the side number and area of winner cells. These results prompted us to further test the topology hypothesis as a possible mechanism for winner-cell compensatory expansion.

2.4.4. Occurrence of directionally biased cell intercalation upon apoptosis correlates with winner-specific increase in cell area.

To understand how intercalations following apoptosis selectively increase winner side number and area, I first analyzed where cell intercalations took place relative to the clone boundary. Pupal notum junctions are reportedly subject to stochastic fluctuations of edge length that trigger cell intercalations by chance as edge lengths decrease to zero (Curran et al. 2017). This framework suggests that shorter junctions are more likely to undergo intercalation, and *in vivo* observations consistently showed a higher probability of intercalation at shorter edges (Fig. 2.2d, d'). In anisotropic dying cells caused by differential proliferation rates (Fig. 2.1), edges perpendicular to the clone boundary were shorter than other edge types (Fig. 2.5a, a', a'', Fig. S2.4b, S2.5b; see Fig. 2.5b for edge classification), suggesting that these perpendicular edges were more likely to be eliminated by cell intercalation. Indeed, both *in silico* and *in vivo* experiments with Yki and Ras^{V12} indicated that cell intercalation likely occurred in a manner to eliminate the perpendicular edges (perpendicular intercalation) during anisotropic loser cell delamination (Fig. 2.5d, d', d'', Fig. S2.2f, f', S2.4c, S2.5c; see Fig. 2.5b, c, Fig. S2.4e–f for the definition of normalized frequency of cell intercalation). Moreover, the increased frequency of perpendicular intercalation during an apoptotic event increased the side number and area of winner cells after apoptosis, but not that of loser cells (Fig. 2.5g, g', g'', Fig. S2.2i, S2.4h'', S2.5f). I did not observe this effect for the two other types of intercalation that occurred at boundary and non-boundary edges (Fig. 2.5e–f'', Fig. S2.2g, h, S2.4h, h', S2.5d, e). Thus, perpendicular intercalation frequency during each apoptosis event uniquely correlates with selective increases in winner side number and occupied area.

2.4.5. Perpendicular intercalation directly drives winner-compensatory cell expansion

I next asked how the perpendicular intercalation selectively drives winner-cell expansion. Of the four cells involved in intercalation upon apoptosis (one dying cell and three surviving cells; Fig. 2.6a, upper), two surviving cells gain a single side, whereas the other surviving cell and the dying cell each lose a side after an intercalation event (Fig. 2.6a, upper). Based on this rule, I comprehensively calculated topology changes (side number) in winner and loser cells for all geometrically possible intercalations (Fig. 2.6a, lower). Notably, perpendicular intercalation uniquely increases winner-cell side number, whereas boundary and non-boundary intercalations mainly increase for loser cells. *In silico* experiments were performed to determine whether perpendicular intercalation is sufficient to drive winner-dominated cell expansion. In the simulation, I introduced a directionally biased event of boundary, non-boundary, or perpendicular intercalation upon apoptosis under identical proliferation conditions (Fig. 2.6b, Fig. S2.5i) where intercalation is typically unbiased (Fig. S2.5g, h). This allowed us to examine the contribution of directionally biased intercalation to winner-cell expansion (topology hypothesis; Fig. 2.4b) in the absence of winner compression (compression hypothesis, Fig. 2.4a). By introduction of biased perpendicular intercalation during apoptosis, clonal cells directly in contact with apoptosis consistently increased both their side number and area averaged for each apoptotic event, whereas non-clonal cells in direct contact with apoptosis did not (Fig. 2.6b, right). In contrast, neither side number nor area of clonal cells increased upon the prioritized induction of boundary and non-boundary intercalations (Fig. 2.6b, left and middle). This indicates that frequent perpendicular intercalation upon apoptosis directly increases side number and area in winner cells.

2.4.6. Repetitive topological change by perpendicular intercalation accelerates tissue-scale occupation by winners

Finally, I examined the long-term topological change upon sequential induction of apoptosis in multiple loser cells at clone boundaries (Fig. 2.7a). After simulating repetitive apoptosis where intercalations occur from shorter edges according to *in vivo* regular rule as shown in Fig. 2.2d, d', winner clones took over almost 100% of the total cell area that was lost to apoptosis (Fig. 2.7d, purple), and consequently, winner cells spread more rapidly than in the absence of apoptosis (middle and left panels of Fig. 2.7b; Fig. 2.7c, purple and black). This long-term expansion of winner cells was ensured by stably maintaining anisotropy of loser cells during multiple apoptosis events (Fig. 2.7e) in which loser cells that were newly faced with clone boundaries after apoptosis subsequently became **anisotropic** (Fig. S2.6). Due to the maintenance of a high-degree of cell anisotropy, the frequency of perpendicular intercalation remained high during apoptosis (Fig. 2.7f). This allowed winner cells at the outermost layer of the clone persistently increased their side number and area for a long-term during clone development (Fig. S2.7a–c). Additionally, winner cells inside clones (i.e., more than two cell distances away from the clone boundary) also slightly expanded on a longer time scale (Fig. S2.7e, inside) without changing side number (Fig. S2.7d, inside), possibly due to an accumulation of minor relaxations of mechanical compression (Fig. S2.3h, acquired area of winner cells localized to two- or three cells away from apoptotic cells). I note that this increase in cell area by mechanical relaxation was relatively modest compared to the dramatic area expansion as a result of cell topological change at the clone border (Fig. S2.7d, e). These results suggest that topological change driven by frequent perpendicular intercalation is still critical for long-term winner-clone spreading. Accordingly, I incorporated random directionality into intercalations following apoptosis under differential proliferation rates to assess whether winner-clone spreading is disrupted by the unbiased occurrence of three intercalation types (randomized intercalation; right panels of Fig. 2.7b). I found that clone spreading speed was reduced (Fig. 2.7c, light-blue) due to equal and simultaneous increases in the side number and cell area of both winner and loser cells (Fig. S2.7b, c bottom panel). As such, the net increase in winner-clone area after loser apoptosis was reduced to approximately 50% of the total area lost to apoptosis (Fig. 2.7d, light-blue), confirming that topological change at the clone boundary significantly contributed to winner-clone spreading.

Because topological change due to apoptosis is limited to cells in direct contact with apoptotic cells, loser death restricted nearby winner clones, as seen in many cell competition systems (Amoyel and Bach 2014), would promote winner-clone spreading. I examined *in silico* whether the restricted death actually improves winner expansion by comparing it to a scenario in which apoptotic cells were spatially scattered in slower dividing cell population. I found winner clones most effectively occupied the apoptotic territory when loser apoptosis was restricted to the clone boundary (Fig. S2.7f–h, up to 1-cell distance). On the other hand, occupation efficiency was reduced when apoptosis had a more scattered spatial distribution (Fig. S2.7f–h, up to 3- or 5-cell distance), and further dropped down to baseline (no apoptosis) when death had a completely random distribution (Fig. S2.7f–h, all slower dividing cells). Collectively, I can conclude that repetitive cell topology changes due to frequent perpendicular intercalation at the clone periphery accelerates tissue-scale occupation by winner cells.

2.5. Discussion

It has long been acknowledged that loser apoptosis is limited to within several cell diameters away from winner clones in many cell competition systems (Amoyel and Bach 2014). However, it was unclear how this localized apoptosis influences subsequent winner tissue occupation. Here, I showed that localized apoptosis adjacent to the clone boundary efficiently accelerates winner-clone expansion through cell topological changes, indicating that regulating topology might have a major contribution to tissue takeover by winners (Fig. 2.7, Fig. S2.7). I also identified the mechanisms underlying these topological alterations (Fig. 2.7g): Anisotropic loser cells driven by localized overgrowth (Fig. 2.1) undergo apoptosis, producing a non-cell-autonomous increase in the side numbers and areas of surrounding winner cells (Fig. 2.2, 2.3). Such selective winner expansion is regulated by directionally biased cell intercalation (Fig. 2.5, 2.6), which occurs as a consequence of perpendicular edge shortening in anisotropic apoptotic cells (Fig. 2.2d, d', 2.5a, a', a''). Although polarized actomyosin-dependent mechanical tension is well known to bias intercalation direction in many morphogenetic processes (Guirao and Bellaïche 2017; Heisenberg and Bellaïche 2013), the Hippo pathway mutant clone in the *Drosophila* epithelium did not accumulate myosin II or increase tension at the radial junction (i.e., perpendicular edge), but did at the circumferential junction (i.e., non-boundary edge) of wild-type cells surrounding clones (Legoff et al. 2013; Mao et al. 2013). The compensatory expansion of winner cells upon apoptosis should therefore be achieved by stochastic junction loss at the shorter perpendicular edges rather than greater tension due to active myosin enrichment.

In addition to perpendicular intercalation, theoretical analysis indicates that a specific boundary intercalation subtype increases winner-cell side number and area following apoptosis (top row of Table in Fig. 2.6a). Because the subtype only occurs when all surviving cells involved in the intercalation were winners, it should be frequent when an apoptotic cell shares more sides with winner cells. This situation in which the boundary intercalation subtype is more frequent than perpendicular intercalation might be rare in Yki- or Ras-activating clones with fewer shared sides due to cell sorting (Bosveld, Guirao, et al. 2016), but frequent in Myc- or Minute-dependent competition, where winner and loser cells actively mix to increase their shared sides (Kale, Rimesso, and Baker 2016; Levayer et al. 2015; Li et al. 2009). Moreover, regarding the expansion process, intercalation-mediated space filling does not require cell division (Fig. S2.3i). This fact is supported by live notum imaging that shows winner expansion even after growth arrest. Therefore, intercalation-mediated winner expansion might contribute to the competition scenario without proliferation (e.g., post-mitotic tissue (Tamori and Deng 2013)). Future examination of the relative contributions of intercalation subtypes in various cell competition scenarios would clarify the topological dynamics that lead to selective winner expansion.

Given the knowledge that a striking increase in cell apical area stimulates proliferation through feedback regulation by mechanical signaling pathways in non-competitive tissue (Aragona et al. 2013; Gudipaty et al. 2017), I expected that the dramatic increase in winner-cell area that follows loser apoptosis (Fig. 2.7b) would facilitate winner proliferation. As such, the increase in cell area by topological change is transformed into the increase in cell number, which could further accelerate long-term clone expansion. It was recently suggested that mechanical or morphological consequences of cell loss affect the division orientation of winner cells, which colonize lost territory (Kale et al. 2016; Li et al. 2009). Therefore, examination of the contribution of positive feedback on winner division rate and orientation *in silico* (Lee and Morishita 2017) and *in vivo* would provide a more comprehensive understanding of winner-clone spreading. Although it was difficult to detect this positive feedback effect on cell division with live imaging in notum, due to growth arrest during terminal differentiation, it will be interesting to monitor the contribution of cell expansion to division in actively growing tissue.

2.6. Figures

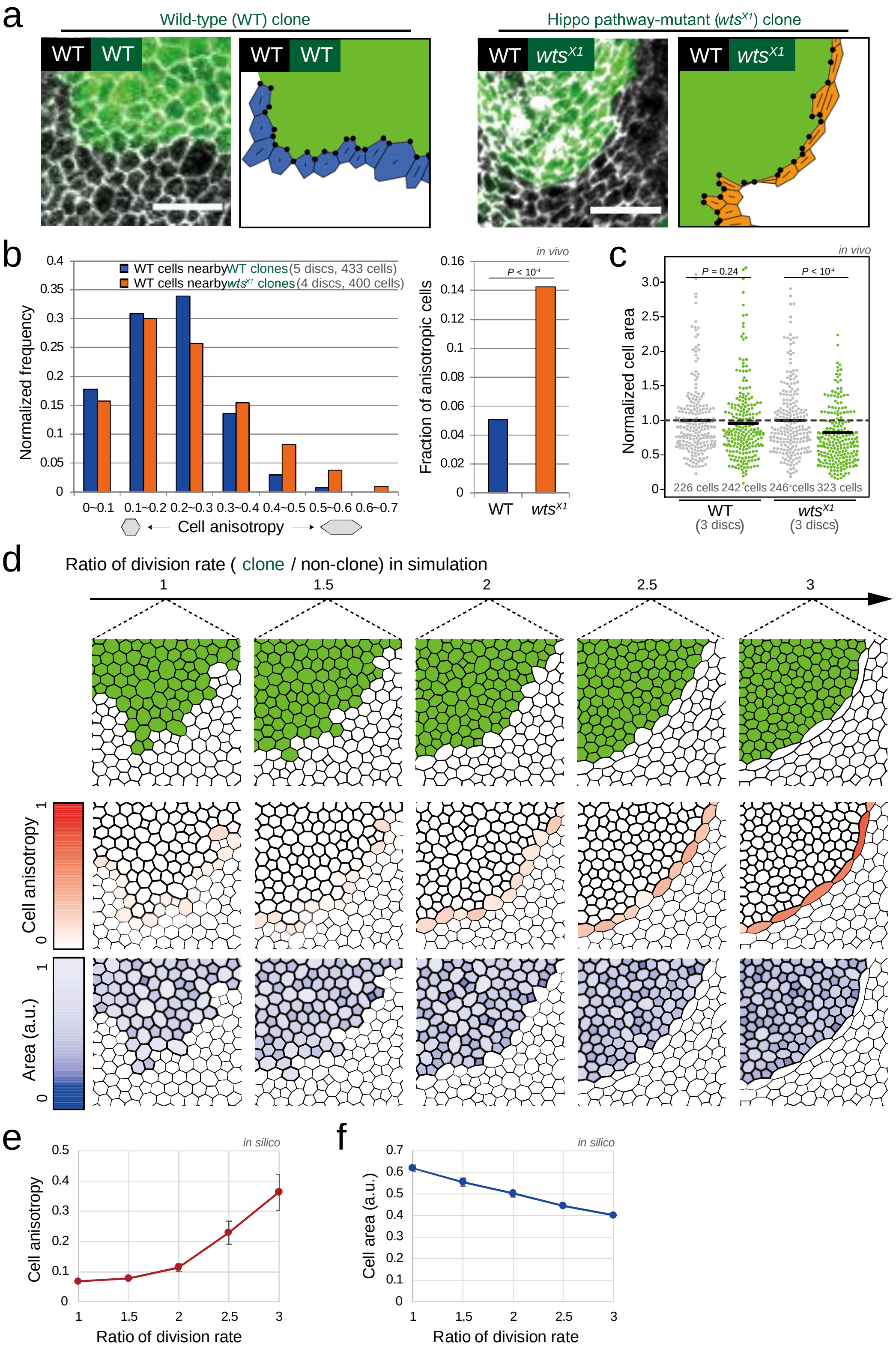

Fig. 2.1. Differential proliferation induces local anisotropic distortion in slower dividing cells at

the clone boundary and compression in faster dividing cells.

(a) Apical cell-cell junctions are marked by E-cad in the hinge region of *Drosophila* wing discs in representative clones: green fluorescent protein (GFP)–expressing cells are wild-type (WT clone, left) and *wts*^{X1} (*wts*^{X1} clone, left) cells, respectively, whereas non-GFP-expressing cells are wild-type cells (WT clone and *wts*^{X1} clone, left). Scale bar, 10 μm. Wild-type cells directly adjacent to the GFP-expressing clones were extracted, with black vertices representing tricellular junctions at the clone boundary and bars representing cell anisotropy (WT clone, right, blue and *wts*^{X1} clone, right, orange). The samples were prepared by Y. Sando and imaged by Y. Sando and me. **(b)** Left: The distribution of cell anisotropy directly adjacent to wild-type and *wts*^{X1} clones. Right: The fraction of cells whose anisotropy value is greater than 0.38. This threshold value was ranked in the top 5% of the value in the case inducing wild-type clones. Fisher's exact test was performed. **(c)** Plot of apical area of non-GFP-expressing (gray) and GFP-expressing (green) cells at the clone boundary normalized to the average area of the non-GFP-expressing cells. Wilcoxon rank sum testing was performed. **(d)** Top: Close-up images of simulated clone at the indicated division rate ratios [clone (green) / non-clone (white)] when the number of clonal cells (green) is 1000. Middle: Anisotropy of non-clonal cells (top, white) along the clone boundary in the same field. Bottom: Cell area of clonal cells (top, green) in the same field. **(e, f)** Average anisotropy of non-clonal cells along the clone boundary (e) and average area of clonal cells directly adjacent to the clone boundary (f) were plotted as a function of the division rate ratio. Simulation setup is identical to panel d. Error bars represent s.d. for 10 clones simulated at each division rate ratio. a.u., arbitrary unit.

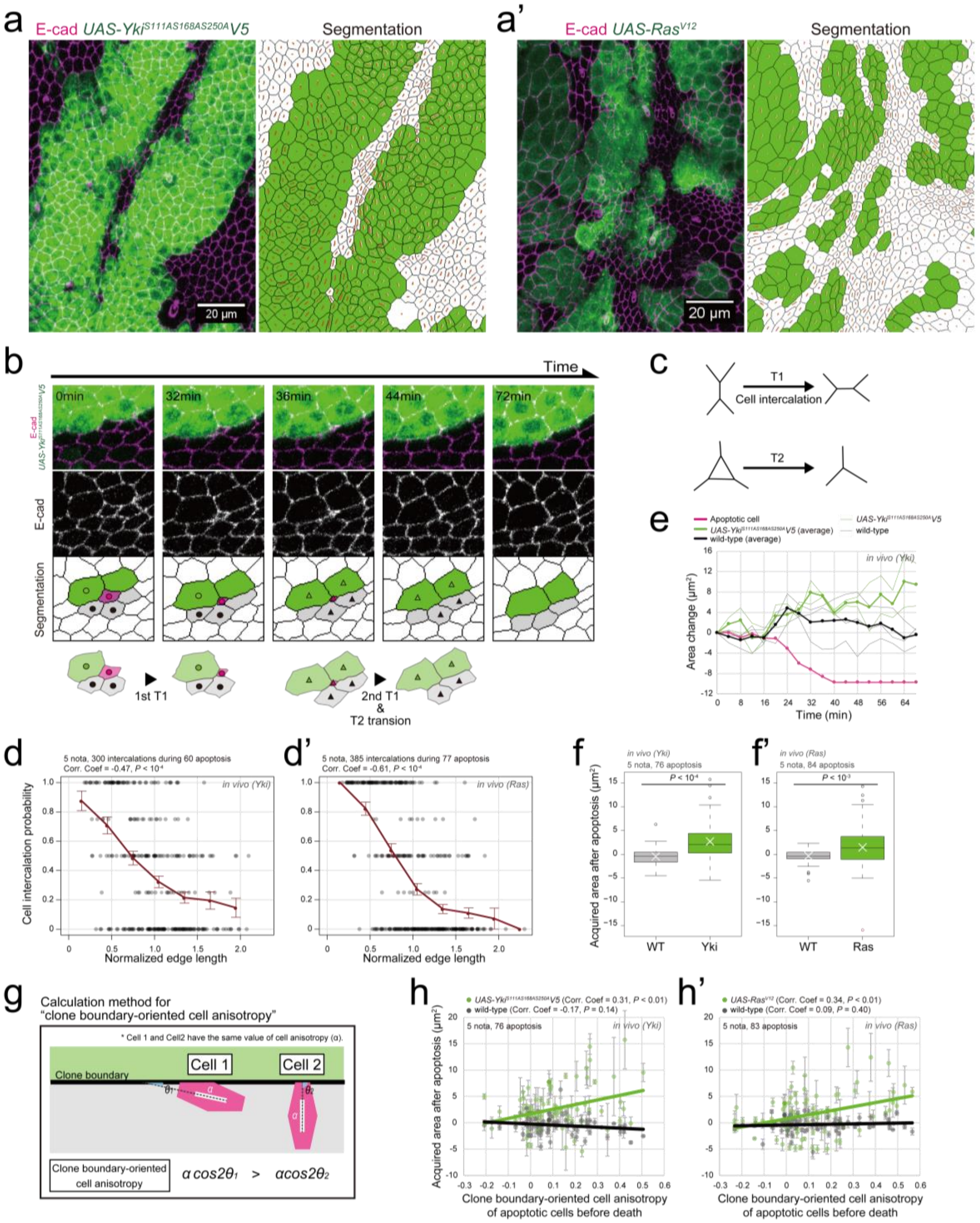

Fig. 2.2. Winner cells expand into spaces originally occupied by apoptotic loser cells with higher cell anisotropy in *Drosophila*.

(a, a') Left: Z projection of a snapshot (22.47 hours after Gal4-mediated transcription activation) taken during live imaging of pupal notum (anterior direction along the anterior-posterior axis is upward) with adherens junctions (indicated by E-cad::GFP; magenta) and clones overexpressing Yki:V5^{S111A,S168A,S250A} (green, a: *y, w, hs-flp; DE-Cad::GFP; Act>CD2>GAL4, UAS-CD8.mCherry* ×

P{tubP-GAL80ts}20; UAS-Yki:V5^{S111A,S168A,S250A}) or Ras^{V12} (green, a': *y, w, hs-flp; DE-Cad::GFP; Act>CD2>GAL4, UAS-CD8.mCherry* × *P{tubP-GAL80ts}20; UAS-RasV12*). Right: Image segmentation based on adherens junction localization shown in left panel. Strength and orientation of cell anisotropy (Aigouy et al. 2010) are indicated by brown. The sample preparations and imaging were done by me for (a) and D. Umetsu for (a'). For both panels (a, a'), investigation of experimental conditions and constructions of fly lines were performed by me. **(b)** Time course of a loser delamination through repeated cell intercalations (known as D1-type delamination [7,20]). Schematic drawings (lower panels) represents intercalations (○, ●, △, ▲). Fly genotype is the same as in a. **(c)** Schematic of cell intercalation (T1 transition) and T2 transition. **(d, d')** Cell intercalation probability as a function of edge length in dying cells 40 minutes before completion of apoptosis next to clones overexpressing Yki:V5^{S111A,S168A,S250A} (d) or Ras^{V12} (d'). Each edge length was normalized to the averaged edge length of its belonging dying cell. Cell intercalation probability was determined whether intercalation occurred (probability = 1) or not (probability = 0) (see more details in Fig. S2.4e–f). Each black point represents data calculated from a single cell intercalation event. Red dots represent binning of the averaged cell intercalation probability for every 0.3 normalized edge lengths. Error bars represent s.e. **(e)** Temporal change in cell area subtracted from value observed 40 minutes before delamination complete [Time = 0 (min)] was plotted for adjacent *UAS-Yki:V5*^{S111A,S168A,S250A} (thin green line), wild-type cells (thin gray line) and an apoptotic cell (magenta line) in (b). The averaged acquired area is shown for faster (thick green line) and slower (thick black line) dividing cells. **(f, f')** Box plots of acquired area after apoptosis, which was obtained by averaging temporal change in cell area (e, thick lines) from 16 to 24 minutes after delamination complete, upon induction of clones overexpressing Yki:V5^{S111A,S168A,S250A} (f) or Ras^{V12} (f'). The upper and lower hinges and middle line represent the 25th, 75th, and 50th percentiles, respectively. White Xs represent the averaged value. Wilcoxon signed rank testing was performed after excluding a dataset of outlier [a red dot in (f', Ras)] detected with the Smirnov-Grubbs test. All subsequent Ras analyses were performed excluding the outlier dataset. **(g)** Schematic of clone-boundary-oriented cell anisotropy (Eq. 2.2 in Methods), which considers both anisotropy strength (α; Eq. 2.1) and its orientation relative to the clone boundary (θ). **(h, h')** Acquired area after apoptosis (f, f') was plotted as a function of the clone-boundary-oriented anisotropy of apoptotic cells (Eq. 2.2 in Methods) 40 minutes before delamination completion and upon induction of clones overexpressing Yki:V5^{S111A,S168A,S250A} (h) or Ras^{V12} (h'). Error bars represent s.d. for data collected 16 to 24 minutes after delamination completion.

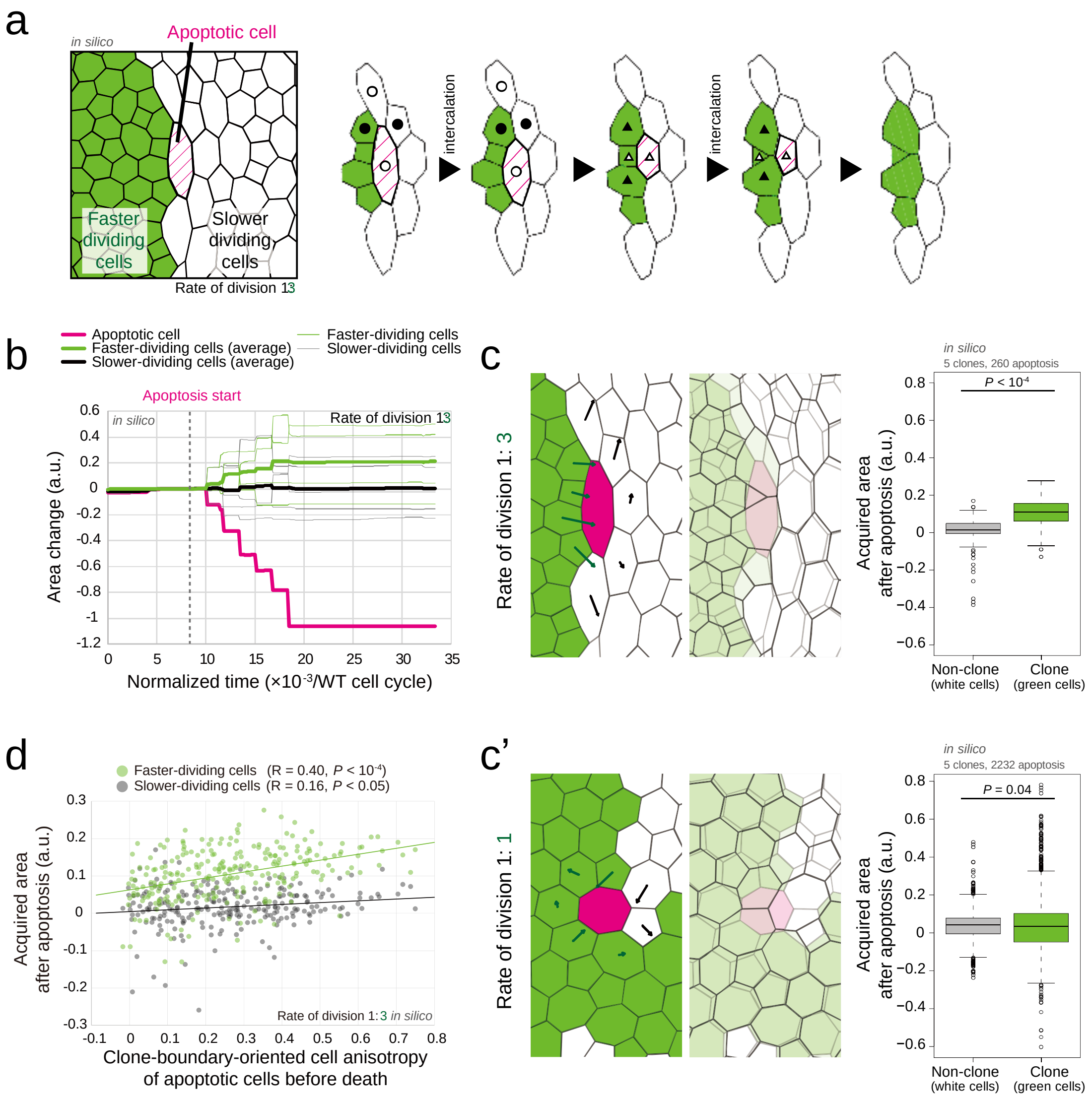

Fig. 2.3. Winner cells expand into spaces originally occupied by apoptotic loser cells with higher cell anisotropy in simulations.

(a) Time course of an apoptotic delamination with repeated cell intercalation (○, ●, △, ▲). Apoptosis (magenta) was induced in a slower dividing cell (white) directly adjacent to the clone boundary when the number of faster dividing cells (green) was 1000. **(b)** Temporal change in cell area subtracted from pre-apoptosis value (normalized time [/loser cell cycle] = 8.3×10^{-3}) was plotted for adjacent faster (thin green line), slower (thin gray line) dividing cells and an apoptotic cell (magenta line) in a. The averaged acquired area for faster (thick green line) and slower (thick black line) dividing cells is shown. The step-like decreases in apoptotic cell area indicate six intercalation events. **(c, c')** Differential (c) and identical (c') proliferation rates. Left: Displacement of cells surrounding apoptotic cell at the time before and after apoptosis is shown by arrows; the ends of the arrows show the position of cell centroids at normalized time [/loser cell cycle] = 8.3×10^{-3} (tail end of arrow) and 2.5×10^{-2} (arrowhead).

The displacement of clonal cells (green) was oriented toward the apoptotic cell (magenta) with differential proliferation rates (c) and randomly oriented with identical proliferation rates (c'). Middle: Overlay of pre- and post-apoptotic images at normalized time [/loser cell cycle] = 8.3×10^{-3} (light gray) and 2.5×10^{-2} (dark gray), respectively. Right: Averaged acquired area (b, thick lines) after apoptosis completion (normalized time [/loser cell cycle] = 2.5×10^{-2}) when apoptosis was independently introduced into all non-clonal cells (white) directly adjacent to clone boundary. Wilcoxon signed rank testing was performed after excluding datasets of outliers [three and four red dots in upper and bottom panels, respectively] detected with the Smirnov-Grubbs test. Subsequent simulation analyses were performed excluding the outlier datasets. **(d)** Averaged acquired area after apoptosis (c, right) plotted as a function of clone-boundary-oriented anisotropy (Eq. 2.2 in Methods) of apoptotic cells immediately before cell death (normalized time [/loser cell cycle] = 8.3×10^{-3}). As shape anisotropy of apoptotic cells increased, the dominance of winner-cell expansion became more pronounced. The division rate ratio (green/white) = 3 for (a, b, c, d) and 1 for (c').

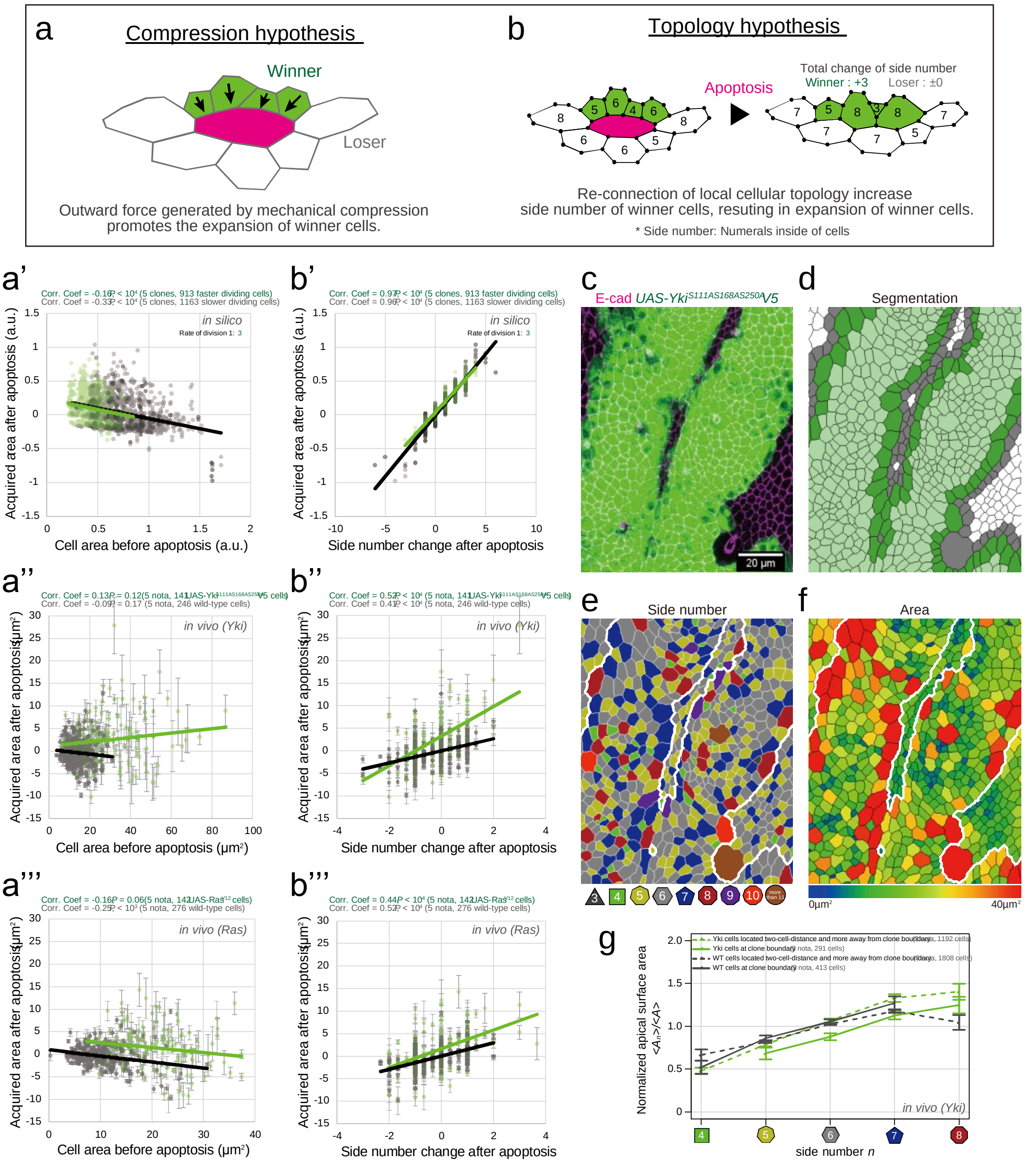

Fig. 2.4. Two hypothetical mechanisms of winner-dominated cell expansion

(a) Compression hypothesis. Compressed, faster dividing winner cells (green) should occupy the space left by the apoptotic cells (magenta) because the apical area of these compressed cells is smaller than their preferred area. Therefore, the winner cells (green) are more likely than the non-compressed loser cells (white) to expand when space becomes available. **(a', a'', a''')** Compression hypothesis testing (a). Area acquired by individual surviving cells directly in contact with apoptotic cells as a function of initial pre-apoptotic area of the surviving cells, which reflects degree of mechanical compression. The pre-apoptotic area was measured at a normalized time [/loser cell cycle] = 8.3×10^{-3} *in silico* (a') and 40 minutes before apoptosis completion *in vivo* [Yki:V5^{S111A,S168A,S250A} (a''), Ras^{V12} (a''')]. Temporal average of the acquired areas of cells directly in contact with apoptosis and s.d. (error bars) *in vivo* were calculated 16–24 minutes after apoptosis completion. See the definition of acquired area for Fig. 2.2e or 2.3b (thin lines). Corr. coef., Pearson correlation coefficient. **(b)** Topology hypothesis. Winner-specific increase in number of cell sides should lead to takeover of the space left by the apoptotic cells (magenta) according to Lewis's law (Lewis 1928). The numerals indicate the number of cell sides. **(b', b'', b''')** Topology hypothesis testing (b). Area acquired by individual surviving cells directly in contact with apoptotic cells as a function of side number change, which was calculated by subtracting the initial side number {normalized time [/loser cell cycle] = 8.3×10^{-3} *in silico* (b'), 40 minutes before apoptosis completion *in vivo* [Yki:V5^{S111A,S168A,S250A} (b''), Ras^{V12} (b''')]} from the final side number [normalized time [/loser cell cycle] = 2.5×10^{-2} *in silico* (b'), average for 16–24 minutes after apoptosis completion *in vivo* (b'', b''')]. The y-axis value is the same as that in (a', a'', a'''). Corr. coef., Pearson correlation coefficient. **(c)** Z projection of a live pupal notum upon induction of clones overexpressing Yki:V5^{S111A,S168A,S250A} (25 hours after Gal4-mediated transcription activation). Fly genotype and image frame is the same as in Fig. 2.2a; the anterior direction is upward. **(d)** Image segmentation for adherens junctions shown in c. Green and gray cells represent Yki-overexpressing and wild-type cells at clone boundary, whereas light green and white cells represent Yki-overexpressing and wild-type cells located two cell distances or more away from clone boundary. **(e, f)** Side number (e) and area (f) of each cell shown in c are indicated by colors. White line represents clone boundary. **(g)** Averaged area of cells with n-sides (A_n) normalized by that of all cells for each cell category (A) (i.e. A_n/A where < > denotes the population average) at 25–26 hours after Gal4-mediated transcription activation. Cells were classified into four categories: green and gray solid lines are Yki-overexpressing and wild-type cells, respectively, at the clone boundary (green and gray cells in d), whereas green and gray broken lines are Yki-overexpressing and wild-type cells, respectively, located at a distance of two cells or more away from the clone boundary (light green and white cells in d). Error bars represent s.e.

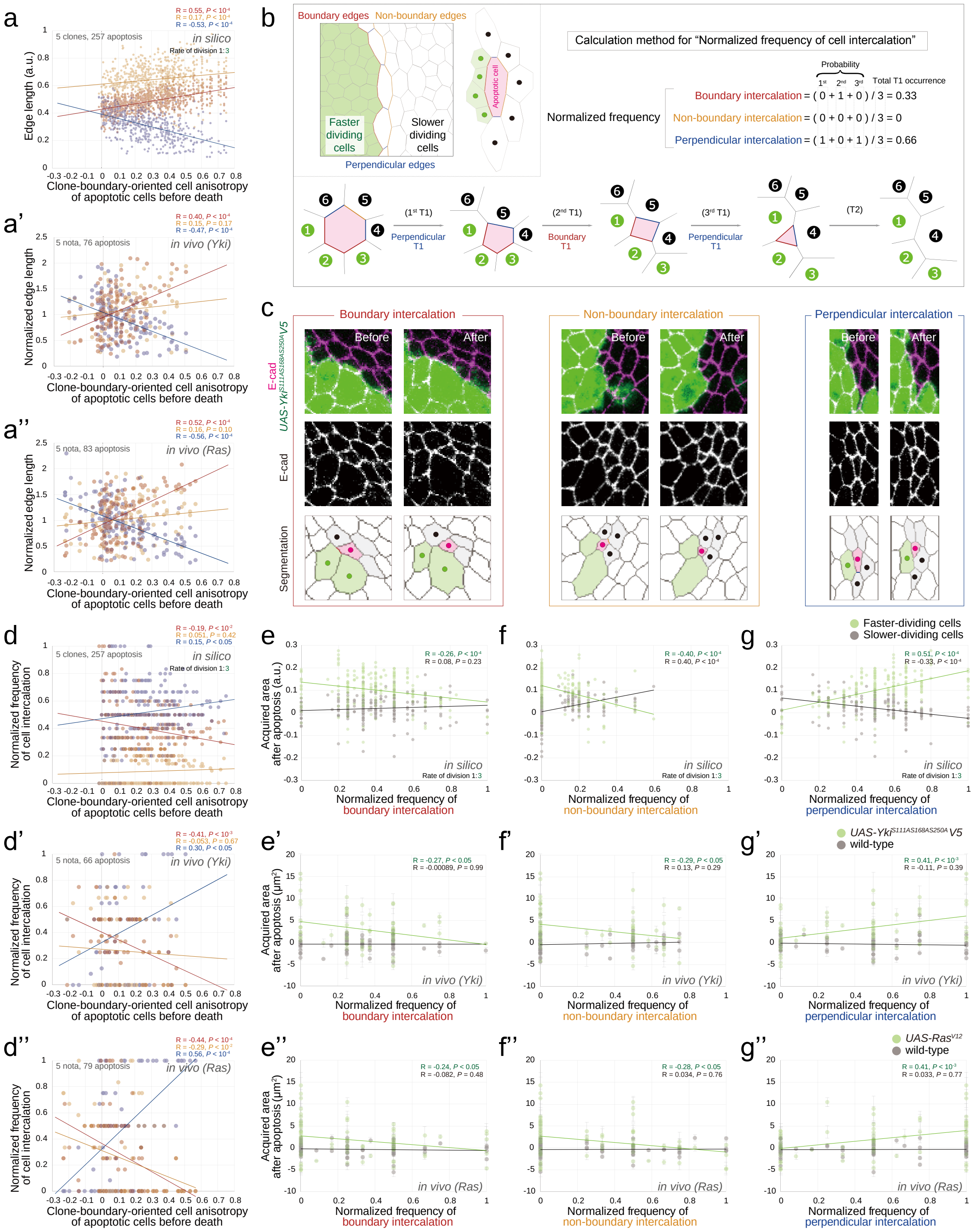

Fig. 2.5. Topological change by directionally biased cell intercalation upon apoptosis correlates with winner-specific increase in cell area.

(a, a’, a”) The length distribution of three types of edges introduced in (b, inset) as a function of anisotropy of an apoptotic cell before death. The x-axis values are the same as that in Fig. 2.2h, h’ for experiments and in Fig. 2.3d for simulation. The y-axis values of experiment [Yki:V5^{S111A,S168A,S250A} (a’), Ras^{V12} (a”)] are the same as those in the x-axis of Fig. 2.2d, d’. **(b)** A calculation example for the “normalized frequency of cell intercalation” for each type used in d–g”. Green circled numbers 1, 2, and 3 indicate clonal cells, whereas black circled numbers 4, 5, and 6 indicate non-clonal cells. The normalized frequency was calculated by dividing the sum of the probability of each intercalation event by the total number of intercalation events. The classification of edges was determined each time after an intercalation. Inset: Classification of edges belonging to apoptotic loser cells (right, magenta cell). Boundary edge (red): edges on the clone boundary. Non-boundary edge (orange): edges between the two vertices, neither of which are at the clone boundary. Perpendicular edge (blue): edges located perpendicular to clone boundary. **(c)** Examples of three types of cell intercalation, which are classified according to the types of disappearing edges (b, inset), in pupal notum. Fly genotypes are the same as in Fig. 2.2a. **(d, d’, d”)** Normalized frequency of three intercalation types observed in a single apoptosis event as a function of anisotropy of an apoptotic cell before death. The x-axis values for simulation (d) and experiment [Yki:V5^{S111A,S168A,S250A} (d’), Ras^{V12} (d”)] are the same as in (a, a’, a”). **(e, e’, e”, f, f’, f”, g, g’, g”)** Averaged acquired area of winner cells (green) and loser cells (gray) as a function of normalized frequency of boundary (e, e’, e”), non-boundary (f, f’, f”), and perpendicular (g, g’, g”) intercalation in simulations (e, f, g) and experiments [Yki:V5^{S111A,S168A,S250A} (e’, f’, g’), Ras^{V12} (e’’, f’’, g’’)]. The x-axis values are the same as the y-axis (d) for simulations and in (d’, d”) for experiments, whereas the value and error bars in the y-axis corresponds to y-axis in Fig. 2.3d for simulation and a subset of Fig. 2.2h, h’ for experiment.

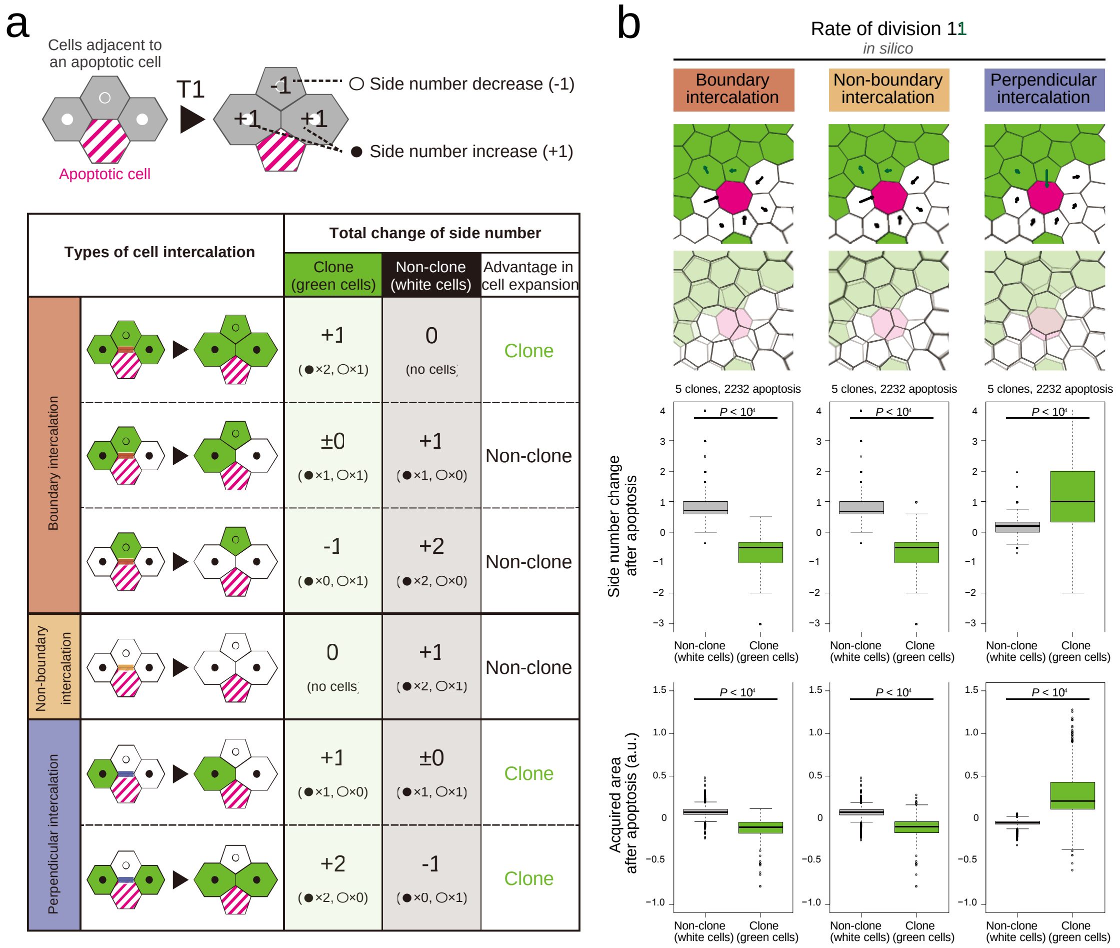

Fig. 2.6. Topological change by perpendicular intercalation drives winner-dominated cell expansion.

(a) Upper: Schematic diagram of the topological changes in three cells directly in contact with the apoptotic cell (magenta) that are directly involved in cell intercalation during apoptotic delamination (Fig. 2.3a). After intercalation, side number is reduced by one for one adjacent cell (-1, open circles), but is increased by one for the other two cells (+1, filled circles). Lower: Three types of cell intercalation (Fig. 2.5c) were divided into six subtypes based on all possible combinations of cell configuration. Total change in side number after intercalation is shown for clonal (green columns) and non-clonal (gray columns) cells. Advantage in cell expansion represents cells with a greater increase in total side number. All topological changes are maintained whenever side number of apoptotic cell is more than 4 before apoptosis. **(b)** Top, schematic representation of the indicated intercalation types. Lower boxplots, change in side number (upper boxplots) and cell area (bottom boxplots) averaged for each apoptotic event. Apoptotic simulation was performed with a predetermined order of directionally biased cell intercalation under identical division rate conditions. The simulation setup (except for the directional bias in intercalation) and figure preparation were the same as for Fig. 2.3c'. Wilcoxon signed rank testing was performed.

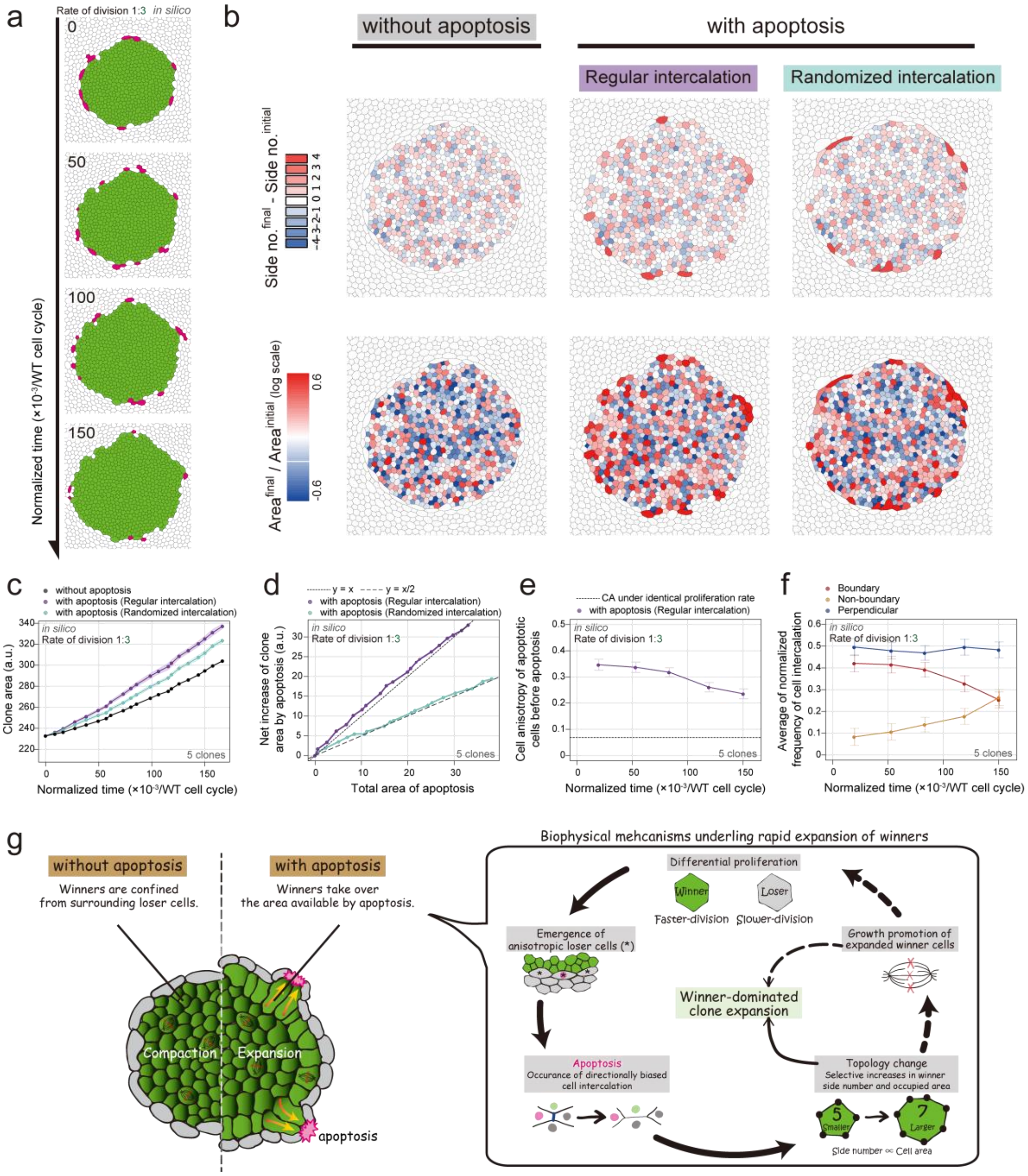

Fig. 2.7. Robust repetition of topological change by perpendicular intercalation accelerates the tissue-scale occupation by winners.

(a) Loser cells that will start to undergo apoptosis within the next 50 (normalized time [/loser cell cycle]) are shown in magenta. Apoptosis was induced in about 40 cells adjacent to winners while the number of faster dividing winner cells (N_{faster}, green) increased from 500 to 700 cells. **(b)** Close-up of colored winner-clone when N_{faster} is 700. Change in side number is shown by subtracting initial (N_{faster} = 500) from final (N_{faster} = 700) side number (upper 3 panels). The log of the ratio of the final cell area over initial cell area is shown (lower 3 panels). Simulation setups were without apoptosis (left); with apoptosis where intercalations occur from shorter edges according to *in vivo* regular rule as shown in Fig. 2.2d, d' (middle; regular intercalation); and with apoptosis where three intercalation types occur randomly (right; randomized intercalation). The number of winner-cell divisions and initial clone (a, normalized time = 0 [/loser cell cycle]) were the same for the three simulation setups. **(c)** Temporal change in clone area with no apoptosis (black), apoptosis with regular intercalation (purple) and apoptosis with randomized intercalation (light-blue). Error bars represent s.d. **(d)** Net increase in clone area as a result of apoptosis calculated by subtracting clone area from that value in the absence of apoptosis as a function of total area of apoptosis. Dashed/dotted lines indicate cases in which winner clones capture 100%/50% of the territory made available by apoptosis. **(e)** Temporal change in anisotropy of apoptotic cells (measured at 1.7×10^{-3} normalized time [/loser cell cycle] before starting to undergo apoptosis). The values were clearly larger than those under conditions of identical proliferation rate without apoptosis (dashed line). Error bars represent s.e. **(f)** Temporal change in normalized frequencies of three types of cell intercalation (see calculation method in Fig. 2.5b, S2.4e–f), which were averaged for every 33.3×10^{-3} (normalized time [/loser cell cycle]). Error bars represent s.e. Division rate ratio (green/white) = 3 for all panels. **(g)** Schematic diagram of the winner-dominated expansion toward the space of apoptosis. Inset: Solid lines are based on my findings, whereas dashed lines represent speculation suggested in previous reports.

2.7. Supporting figures

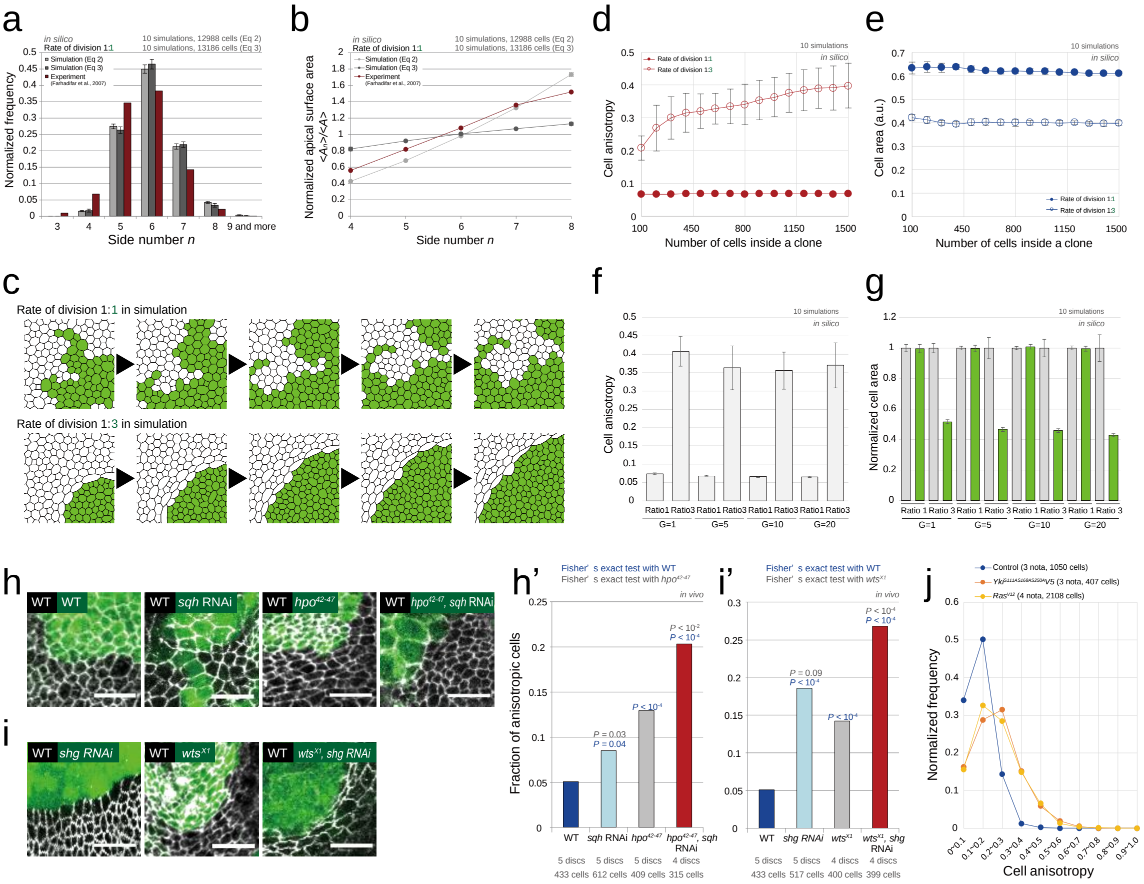

Fig. S2.1. Cell deformation due to differential proliferation rates robustly appeared *in silico* and *in vivo* (related to Fig. 2.1).

(a, b) Cell packing topologies under conditions of identical division rate in simulations (Eq. 2.3 and Eq. 2.4) account for that of normal epithelial cells in *Drosophila* (Farhadifar et al. 2007). Frequency distribution of side number (i.e., *n*-side cells) (a). Average area of cells with *n*-side (A_n) normalized to that of all cells (A) (i.e., A_n/A where < > denotes the population average) (b). Error bars represent s.d. for 10 simulations. **(c–g)** Additional simulation analysis for Fig. 2.1 using Eq. 2.3. **(c)** Time course of the simulated proliferation process under conditions of identical (upper) or differential (lower) proliferation rate, where the number of clonal cells (green) is 100 (far left), 300, 500, 700, or 900 (far right). **(d, e)** Cell anisotropy of non-clonal cells located directly adjacent to the clone boundary (d) and area of clonal cells (e) as a function of number of cells inside of a clone, under conditions of identical (closed circles) and differential (open circles) proliferation rate. Error bars represent s.d. for 10 simulations of each clone at each of the tested times and division rate ratios. **(f, g)** Robustness of cell deformation under identical and differential proliferation rate (representing “Ratio 1” and “Ratio 3,” respectively) with respect to model mechanical parameters: Four different line tension parameter values (G_{ij} = 1, 5, 10, 20) were examined, while the other parameters were kept constant (n_H = 1, l_0 =

0.0001). Cell anisotropy of non-clonal cells (white cells in c) directly adjacent to the clone boundary (f). Area of clonal cells (green cells in c) beside the clone boundary, which is normalized by that of non-clonal cells (white in c) beside clone (g). Increased cell anisotropy and decreased area under differential proliferation rate were reproducible on all tested parameters. Error bars represent s.d. for 10 simulations. The number of clonal cells was 1000 in the simulation. **(h, i, h', i')** Additional experimental analysis for Fig. 2.1a, b. Hippo pathway mutant clones induce anisotropy in slower dividing wild-type cells directly adjacent to the clone even with modulation of junction contractility or adhesion in *Drosophila* wing disc hinge region. Genotypes of clones (green) are shown at top of panels in (h) and (i). Images for WT (h) and *wts*^{X1} (i) are identical to those in Fig. 2.1a (left). See Methods for the strain preparation. The samples were prepared by Y. Sando and imaged by Y. Sando and me. Scale bar, 10 μm. **(h', i')** Fraction of cells whose anisotropy values if greater than 0.38 (see Fig. 2.1b right for definition). Values for WT (h', i') and *wts*^{X1} (i') are identical to those in Fig. 2.1b (right). Statistical test is a Fisher's exact test compared with WT (h',i', blue), *hpo*$^{42\text{-}47}$ (h', gray), or *wts*^{X1} (i', gray). **(j)** Additional experimental analysis for Fig. 2.2a, a'. The distribution of cell anisotropy of wild-type cells directly adjacent to clones overexpressing *P{tubP-GAL80ts}20* (control, blue), *P{tubP-GAL80ts}20; UAS-Yki:V5*^{S111A,S168A,S250A} (*Yki:V5*^{S111A,S168A,S250A}, Orange), and *P{tubP-GAL80ts}20; UAS-Ras*^{V12} (*Ras*^{V12}, Yellow) in *Drosophila* pupal notum.

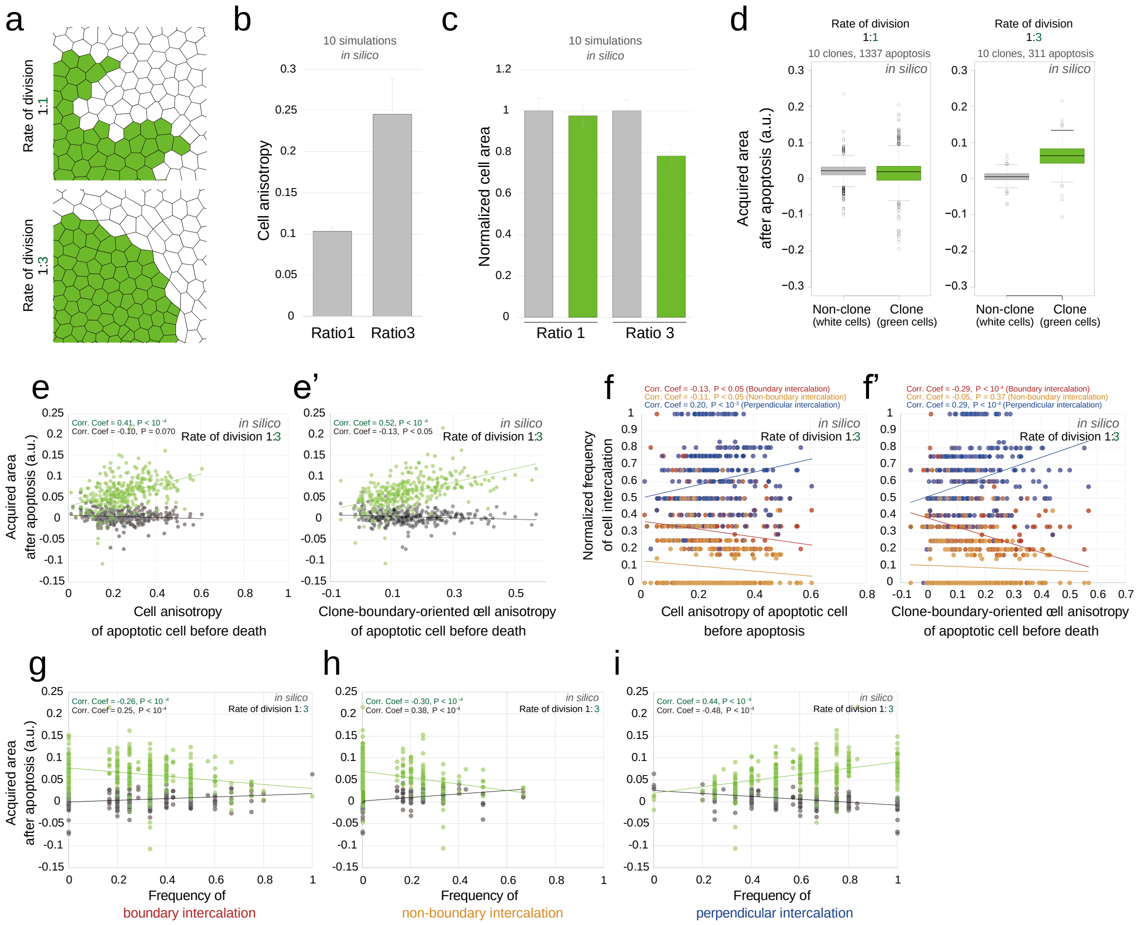

Fig. S2.2. All the series of events leading to winner-dominated cell expansion robustly occurred in another well-used type of cell-vertex model simulation (related to Fig. 2.1, Fig. 2.3, and Fig. 2.5).

(a–i) All results in this figure were obtained in Eq. 2.4. **(a–c)** Cell deformations under identical and differential proliferation rate [representing "Ratio1" and "Ratio3", respectively, in (b) and (c)]. Consistent with the results shown in Fig. S2.1f,g (using Eq. 2.3), anisotropy of slower dividing cells directly adjacent to the clone boundary increased (b) and the normalized area of faster dividing cells at the clone boundary decreased (c). See Fig. S2.1f, g for definition of these measures. Error bars represent s.d. of 10 simulations of each clone at each tested division rate. **(d–i)** Apoptosis simulation. **(d)** Median of averaged acquired area of clonal cells (green) was larger than that of non-clonal cells (white) at division rate ratio = 3 (Wilcoxon signed rank test; $P < 2.2\times10^{-16}$), whereas it was smaller at division rate ratio [clone (green) / non-clone (white)] = 1 (Wilcoxon signed rank test; $P = 1.1\times10^{-4}$). **(e, e')** The positive correlation between winner-cell expansion and shape anisotropy of apoptotic cells was consistent with the results obtained using Eq. 2.3 [Fig. S2.3g for (e), Fig. 2.3d for (e')]. The y-axis values in (e) and (e') are the same. **(f, f')** Frequency of boundary (red), non-boundary (orange), and perpendicular (blue) intercalations observed in a single event of apoptosis as a function of shape anisotropy of an apoptotic cell before death were consistent with the results obtained using Eq. 2.3 [Fig. S2.5c for (f), Fig. 2.5d for (f')]. The y-axis values in (f) and (f') are the same. **(g–i)** The acquired area averaged over faster dividing cells adjacent to apoptosis was plotted as a function of the frequency of cell intercalation. This tendency was consistent with Fig. 2.5e–g. See corresponding legends in main figures for method and plot setup. Unless noted (upper panel of a, "Ratio1" in b and c, left panel of d), the division rate ratio [clone (green) / non-clone (white)] = 3 for all panels. The number of clonal cells (green) was 200 for all panels. Corr. coef., Pearson correlation coefficient.

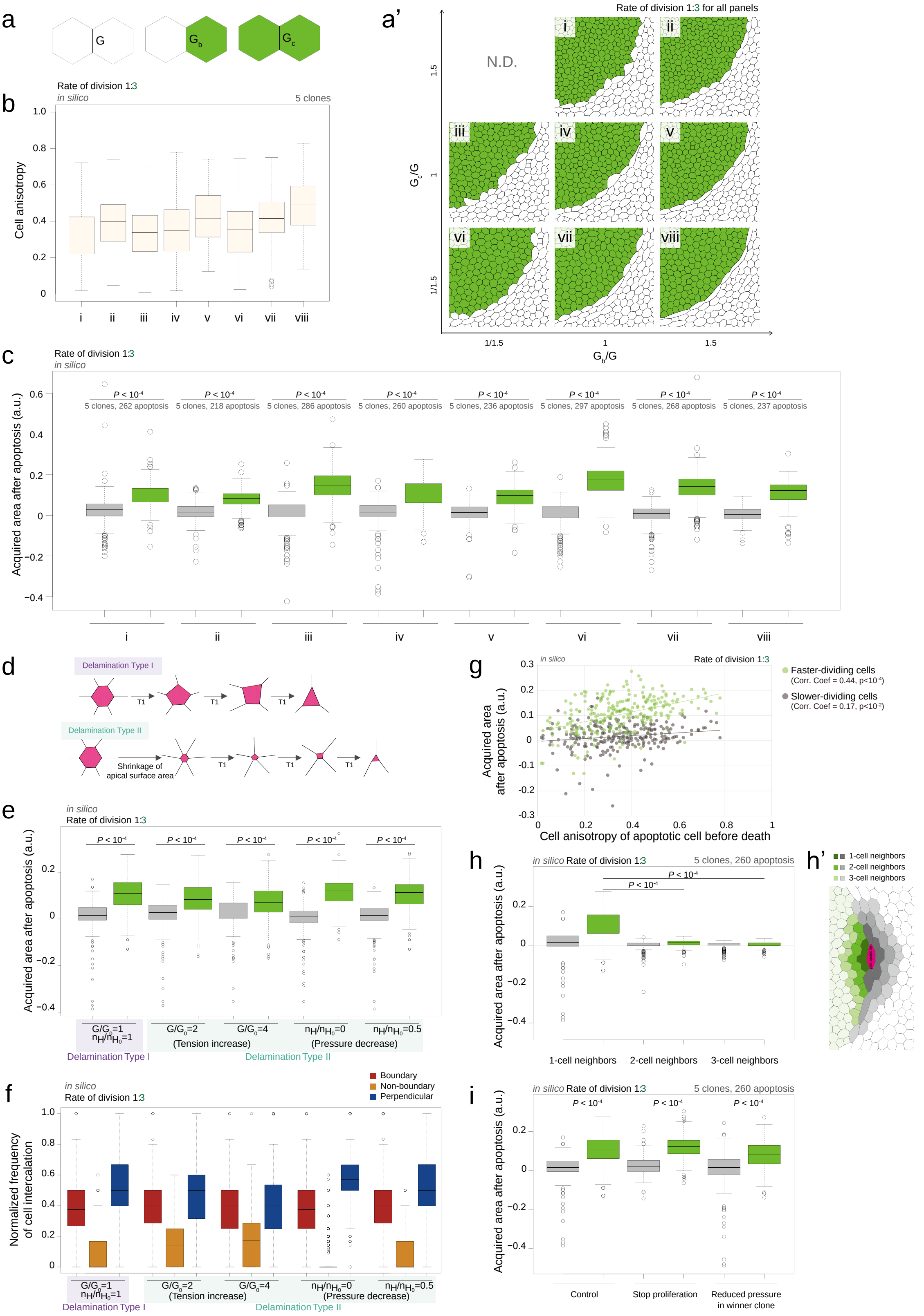

Fig. S2.3. Robust expansion of winner cells occurred with different mechanical parameters between clonal and non-clonal cells and in different apoptosis conditions in simulation (related

to Fig. 2.1, Fig. 2.3, and Fig. 2.5).

(a–c) Simulations under different combinations of relative line tension parameters (G_b / G and G_c / G; Eq. 2.3) with the conditions of differential proliferation rate. **(a)** G is default tension parameter at edges between non-clonal cells (white) (left); G_b is clone boundary tension parameter at edges on clone boundary (middle); and G_c is inner clonal tension parameter at edges between clonal cells (green) (right). **(a')** Close-up images of clone boundary. Note that the model did not work at the parameter indicated by N.D. due to divergence of simulations. **(b, c)** Cell anisotropy of slower dividing cells (white cells in a') directly adjacent to clone boundary (b) and averaged acquired area after apoptosis of slower and faster dividing cells directly in contact with apoptotic cells (gray and green box plots, respectively) (c). Numerals (i–viii) correspond to those in a'. Wilcoxon signed rank testing was performed. All simulations were conducted with 1000 faster dividing cells (green). The division rate ratio [clone (green) / non-clone (white)] = 3 for all panels. **(d–f)** Simulations with respect to different model settings of apoptosis (Eq. 2.3). **(d)** Two types of cell-delaminating processes were numerically simulated. The area of the apoptotic cell (magenta) was decreased through junctional loss by repeated cell intercalation (red edges) while (1) keeping the mechanical parameter values constant (delamination type I; model for the D1 delamination (Levayer et al. 2016; Marinari et al. 2012)), or (2) either increasing the value of the line tension parameter (G_{ij}) or decreasing the value of the pressure parameter (n_H) (Eq. 2.3) before repeating the cell intercalation (delamination type II; model for the D2 delamination (Levayer et al. 2016; Marinari et al. 2012)). Note that while D2 delamination leads to transitory rosette formation after rapid apical surface shrinkage (Marinari et al. 2012), the model I used did not reproduce the intermediate rosette structure due to model limitation on tricellular junctions. **(e)** Averaged acquired area after apoptosis of slower and faster dividing cells directly in contact with apoptotic cells (gray and green box plots, respectively). G and n_H represent parameters of apoptotic cells, whereas G_0 and n_{H0} represent those of non-apoptotic cells. Both delaminating processes showed winner-dominated cell expansion. The measurement method and box plot setup are identical to Fig. 2.2f, f'. Plots of delamination type I (e, the two leftmost boxplots) are identical with Fig. 2.3c. Wilcoxon signed rank testing was performed. **(f)** Normalized frequency of boundary (red), non-boundary (orange), and perpendicular (blue) intercalations observed during apoptosis. As the anisotropic shape of dying cells was maintained during delamination type II, perpendicular intercalation dominated similarly to that which occurred during delamination type I. All apoptotic simulations were conducted with 1000 faster dividing cells (green). The division rate ratio [clone (green) / non-clone (white)] = 3. **(g)** Winner cells expanded more dominantly with increasing anisotropy (Eq. 2.1) of dying loser cells. The y-axis value is the same as Fig. 2.3d. Corr. coef., Pearson correlation coefficient. **(h, h')** Averaged acquired areas after apoptosis of cells directly adjacent to apoptotic cells (1-cell neighbors; h') and cells at two or three cells away from the apoptotic cell (2-cell neighbors or 3-cell neighbors; h'). Slower and faster dividing cells are shown in gray and green box plots, respectively. The plot setup is identical to that in Fig. 2.2f, f'. **(i)** Averaged acquired area after apoptosis of slower and faster dividing cells directly adjacent to apoptotic cells (gray and green box plots, respectively) under simulation with ceasing all cell proliferation during apoptosis (represented by "Stop proliferation"), or simulation reducing pressure in the faster dividing clone during apoptosis [represented by "Reduced pressure in winner clone"; $n_H^{Clone} / n_H^{Non\text{-}clone} = 0.72$, where n_H^{Clone} and $n_H^{Non\text{-}clone}$ represent pressure parameters (Eq. 2.3) of clonal (faster dividing) and non-clonal (slower dividing) cells]. The box plots represented by "Control" are the same as in Fig. 2.3c, which was obtained without additional parameter manipulations. Winner cells still dominated expansion in the absence of the global tissue-scale pushing force generated by winner cells. Wilcoxon signed rank testing was performed for (h) and (i).

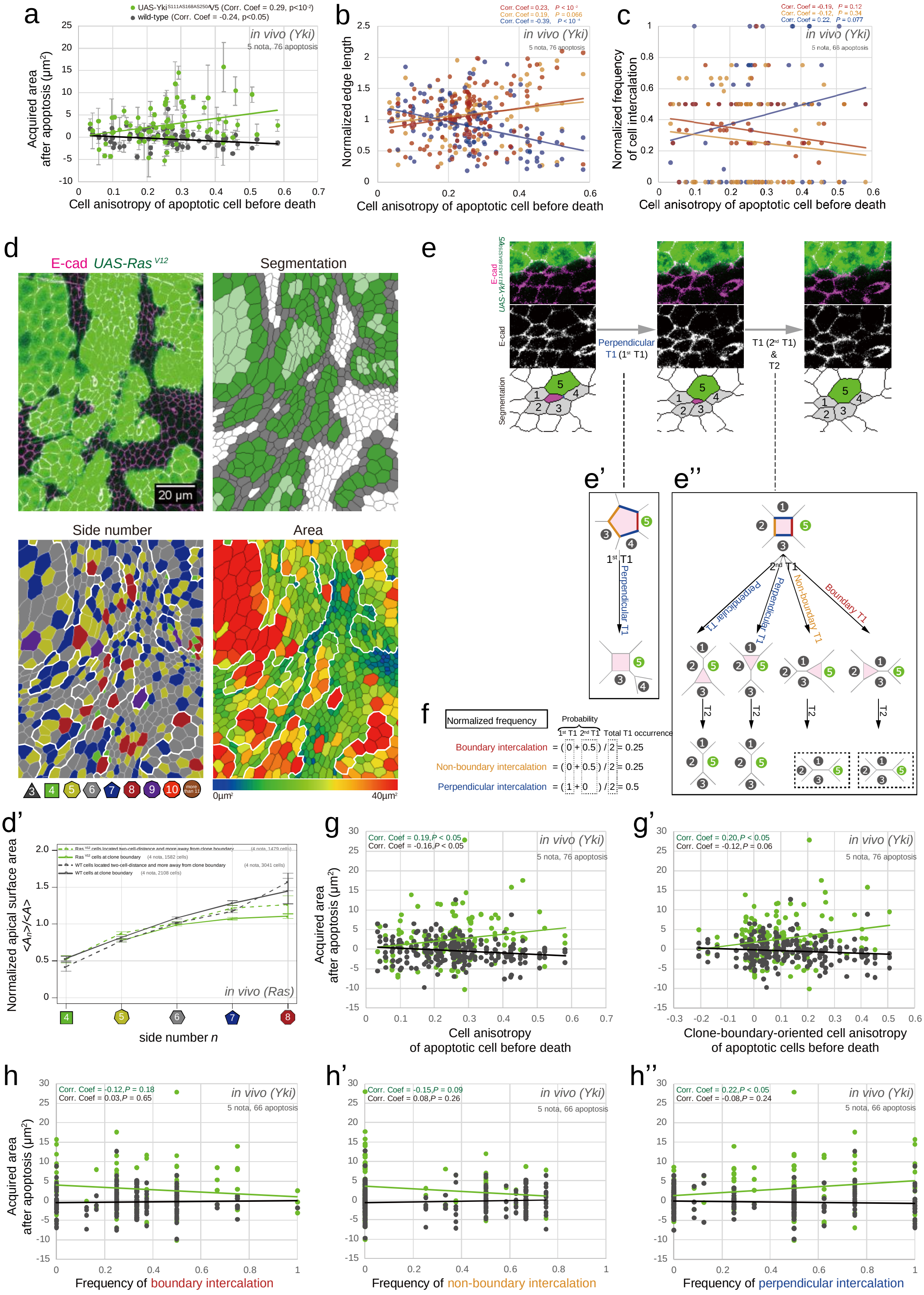

Fig. S2.4. The dynamics of winner-dominated cell expansion *in vivo* (related to Fig. 2.2, Fig. 2.4 and Fig. 2.5).

(a-c) Acquired areas after apoptosis (a), length distributions of three edge types (b), and normalized frequencies of three intercalation types observed in a single apoptosis event (c) were plotted as a function of anisotropy (Eq. 2.1 in Methods) of apoptotic cells 40 minutes before complete delamination. The averaged values and error bars on the y-axes are the same as Fig. 2.2h for (a), Fig. 2.5a' for (b), and Fig. 2.5d' for (c). **(d)** Top-left: Z projection of a live pupal notum (25 hours after Gal4-mediated transcription activation). The fly genotype and image frame are the same as in Fig. 2.2a'; the anterior direction is upward. The sample preparations and imaging were done by D. Umetsu. Top-right: Image segmentation for adherens junctions. Green and gray cells represent Ras^{V12}-overexpressing and wild-type cells at the clone boundary, and light green and white cells represent Ras^{V12}-overexpressing and wild-type cells located two-cell-distance or more away from the clone boundary. Bottom: Side number (left) and area (right) of each cell are indicated with colors. The white line represents the clone boundary. **(d')** Averaged area of cells with n-sides (A_n) normalized by that of all cells for each cell category (A) (i.e. A_n/A where < > denotes the population average) 24–25 hours after Gal4-mediated transcription activation. Cells were classified into four categories: green and gray solid lines are Ras^{V12}-overexpressing and wild-type cells, respectively, at the clone boundary (green and gray cells in d, Top-Right), and green and gray broken lines are Ras^{V12}-overexpressing and wild-type cells, respectively, located two cells or more away from the clone boundary (light green and white cells in d, Top-Right). Error bars represent s.e. **(e–f)** Inference method of intercalated edges when multiple intercalations (T1 transition) and/or T2 transition occurred simultaneously. **(e, e')** An example of cell intercalation upon apoptosis. Pentagonal dying cell (magenta in bottom panels of e) is delaminated by sequential occurrence of two T1 transitions (intercalations) and one T2 transition. The first T1 transition is a perpendicular intercalation (i.e., an edge belonging to cell "4" in (e) is lost; e'), whereas the type of second T1 transition cannot be distinguished due to the simultaneous occurrence of T1 and T2 transitions among the four cells (cells "1", "2", "3", and "5"). Fly genotype is the same as in Fig. 2.2a. **(e'')** All geometrically possible combinations of cell rearrangement during the latter half of the delaminating process (right two panels in e), in which the quadrangular dying cell disappears through a second T1 transition and a T2 transition. Because the quadrangular cell has four edges, there are four possible patterns of rearrangement. Four candidate rearrangements are narrowed down to two (black dashed boxes) that are consistent with cell geometry after delamination complete (rightmost panels in e): boundary or non-boundary intercalation is estimated to occur in the second T1 transition. Numerical cell labels correspond to those in the bottom panels of e. **(f)** Method of calculation of normalized frequency for each type of intercalation. Dashed box labeled "1st T1" or "2nd T1" represents the probability of each type of intercalation for each T1 event. Probability of perpendicular intercalation at 1st T1 is 1, whereas that of boundary and non-boundary intercalations in the second T1 is 0.5 because the number of candidates is two (e''). Dashed box labeled "Total T1 occurrence" represents total number of T1 events (1st and 2nd) during apoptosis. **(g, g', h–h'')** The y-axis values for all panels are the acquired areas after apoptosis without averaging for individual apoptosis events (thin lines in Fig. 2.2e). The x-axis values are the same as Fig. S2.4a for (g), Fig. 2.2h for (g’), Fig. 2.5e’ for (h), Fig. 2.5f’ for (h’), and Fig. 2.5g’ for (h’’).

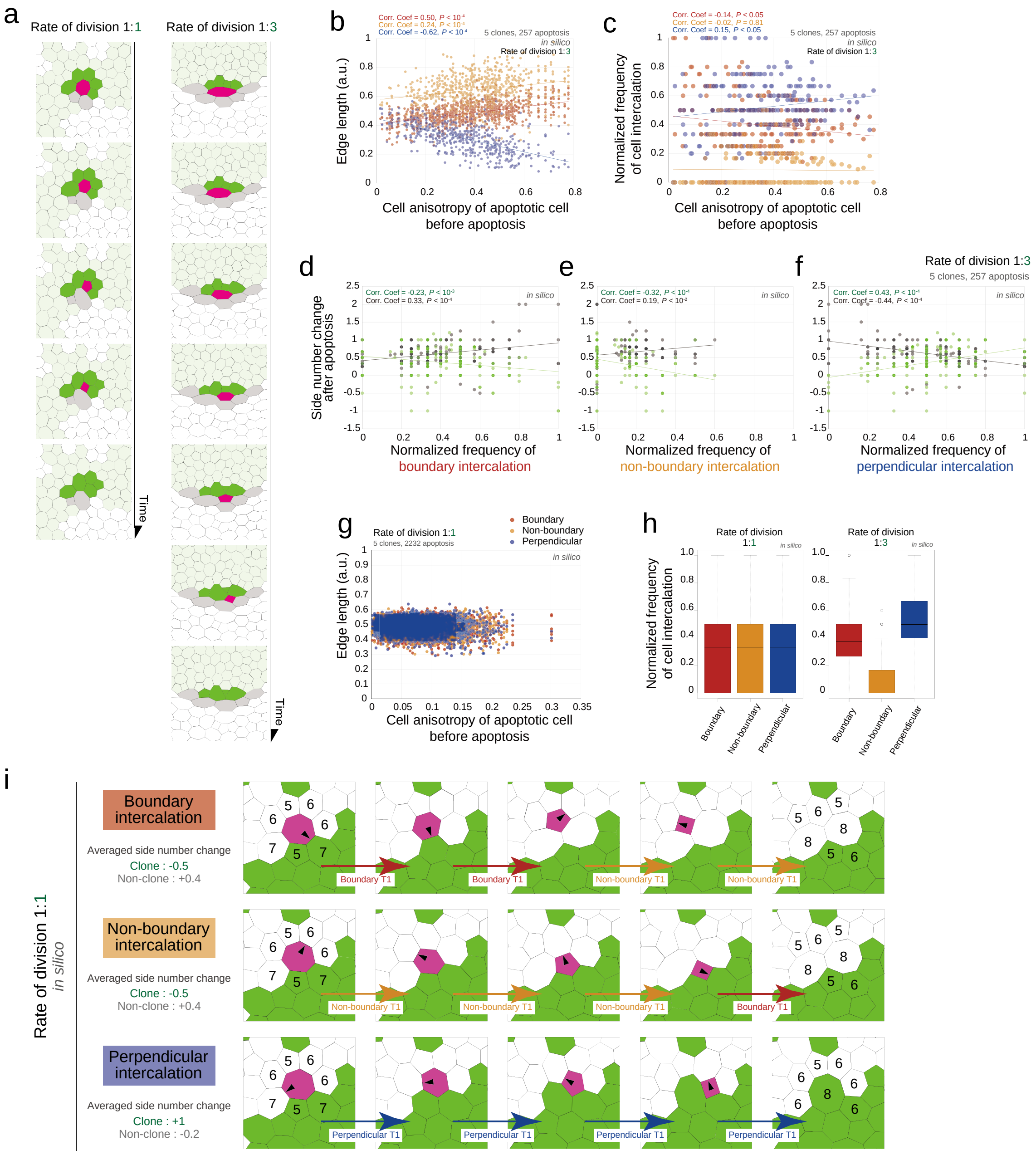

Fig. S2.5. *In silico* examination of the contribution of biased cell intercalations upon apoptosis (related to Fig. 2.3, Fig. 2.5 and Fig. 2.6).

(a) Time course of apoptosis under identical and differential proliferation rates shown in Fig. 2.3c', c, where the figures were rotated 90 degrees. **(b, c)** Length distributions of three edge types (b), and normalized frequency of three intercalation types observed in a single apoptosis event (c) was plotted as a function of cell anisotropy (Eq. 2.1 in Methods) of apoptotic cells immediately before cell death (normalized time [/loser cell cycle] = 8.3×10^{-3}). The y-axis values are the same as in Fig. 2.5a for (b) and Fig. 2.5d for (c). **(d–f)** Change in side number of winner cells (green) after apoptosis was positively correlated with the normalized frequency of perpendicular intercalation (f), but not with that of boundary and non-boundary intercalation (d, e). The correlation of loser cells (gray) was generally opposite that of winner cells. The values of normalized frequency of each type of intercalation is the same as in Fig. 2.5e–g. The division rate ratio [clone (green) / non-clone (white)] = 3 for all panels. **(g)** The length distribution of three types of edges as a function of cell anisotropy of an apoptotic cell immediately before death (normalized time [/loser cell cycle] = 8.3×10^{-3}) under conditions of identical division rate is shown. The distributions were nearly identical for the three types of edges. **(h)** Normalized frequency of boundary (red), non-boundary (orange), and perpendicular (blue) intercalations when apoptosis was independently introduced into all non-clonal cells directly adjacent to clones with 1000 clonal cells. Data for identical (left) and differential (right) proliferation rate are shown. Normalized frequency of the three types of intercalation was nearly identical under identical division rate (left). **(i)** Apoptotic simulations with a predetermined order of directionally biased cell intercalations with identical division rates. Time course of apoptosis with biased occurrences of boundary (upper), non-boundary (middle) and perpendicular (lower) intercalation shown in Fig. 2.6b. Arrowheads indicate the shortest edge in each edge type that is lost via cell intercalations in the next frame. The numerals within cells indicate the numbers of cell sides. Under perpendicular intercalation, one of the two clonal cells decreased the side number (from 7 to 6; i.e. -1), but the other cell increased (from 5 to 8; i.e. +3). Thus, the clonal cells increase their side number on average [i.e. +1 (= (-1+3) / 2)]. Likewise, the averaged side number change (left end) was calculated for non-clones and clones for each intercalation type. Note that with a bias favoring boundary intercalation, dying cells have only non-boundary edges after experiencing sequential induction of boundary intercalations; therefore, only non-boundary intercalations take place after that (upper, right three panels). Under a bias favoring non-boundary intercalation, dying cells only have boundary and perpendicular edges after experiencing sequential induction of non-boundary intercalations; therefore, boundary and/or perpendicular intercalations take place after that (middle, right two panels).

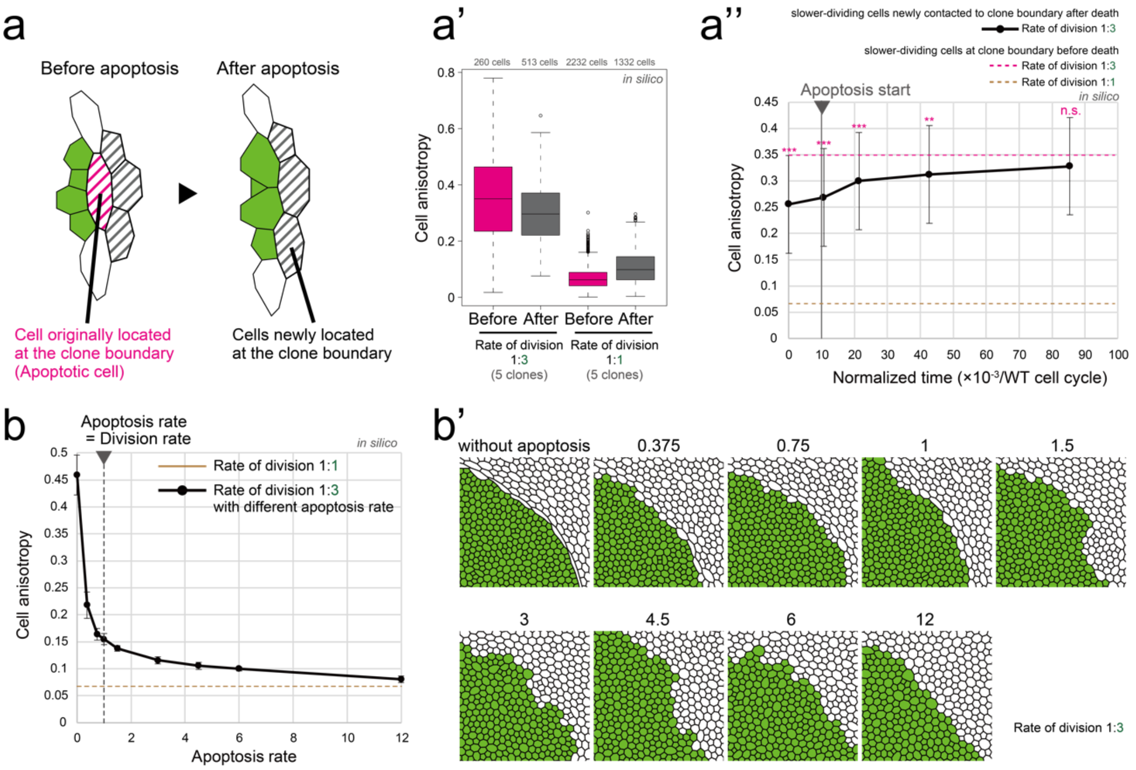

Fig. S2.6. Anisotropic distortion of loser cells at the clone boundary is maintained despite repeated apoptosis (related to Fig. 2.7).

(a–b') Differential proliferation-induced cell anisotropy was maintained in the presence of apoptosis. **(a, a')** To analyze the effects of apoptosis on the emergence of anisotropic cells, I compared the anisotropy of slower dividing cells in contact with the clone boundary at time points "before" (a left; normalized time [/loser cell cycle] = 8.3×10^{-3}) and "after" (a right; normalized time [/loser cell cycle] = 2.5×10^{-2}) apoptosis. The cell originally in contact with the clone boundary before apoptosis (apoptotic cell; magenta) and the slower dividing cells newly in contact with the clone boundary after apoptosis (gray) are shown (a'). Anisotropy immediately after apoptosis (gray) was slightly reduced compared with that before apoptosis (magenta) (a', left two plots), but still higher than that under conditions of identical division rate (a', right two plots). The number of clonal cells was 1000. **(a'')** The average anisotropy of gray cells in (a) increased over time up to that of the apoptotic cell immediately before death (magenta broken line). Division rate ratio [clone (green) / non-clone (white)] = 3. Error bars represent s.d. of 260 independent apoptosis simulations. *P*-values are based on Welch's *t*-test at the indicated times compared with the apoptotic cell immediately before death (normalized time [/loser cell cycle] = 8.3×10^{-3}; magenta broken line); n.s. (not significant), $P > 0.01$; $^{**}P < 10^{-3}$; $^{***}P < 10^{-4}$. **(b)** Robustness of cell anisotropy as a function of apoptosis rate (number of apoptosis events/cell cycle/cell). Note that apoptosis was not induced at apoptosis rate = 0. Apoptosis was simulated by incorporation of cell delamination in slower dividing cells (white cells in b') directly adjacent to the clone boundary under conditions of differential proliferation rates (division rate ratio [clone (green) / non-clone (white)] = 3), while the number of faster dividing winner cells increased from 1 to 3000 cells. Apoptotic cell delamination was simulated by repeating cell intercalation from the shortest edge in an apoptotic cell. When the apoptosis rate is lower than cell division rate (black solid line), anisotropy of slower dividing cells directly adjacent to the clone boundary (black circles with solid line) was 2-fold higher than that of the control (brown line, which represents anisotropy under identical division rate without apoptosis). Error bars represent s.d. of 10 simulations of each clone at each tested apoptosis rate. Anisotropy was measured when the number of clonal cells (green) = 3000 in simulations. **(b')** Close-up snapshots of clone boundary under different apoptosis rates in simulations, where the numerals indicate apoptosis rate given in b. Division rate ratio [clone (green) / non-clone (white)] = 3.

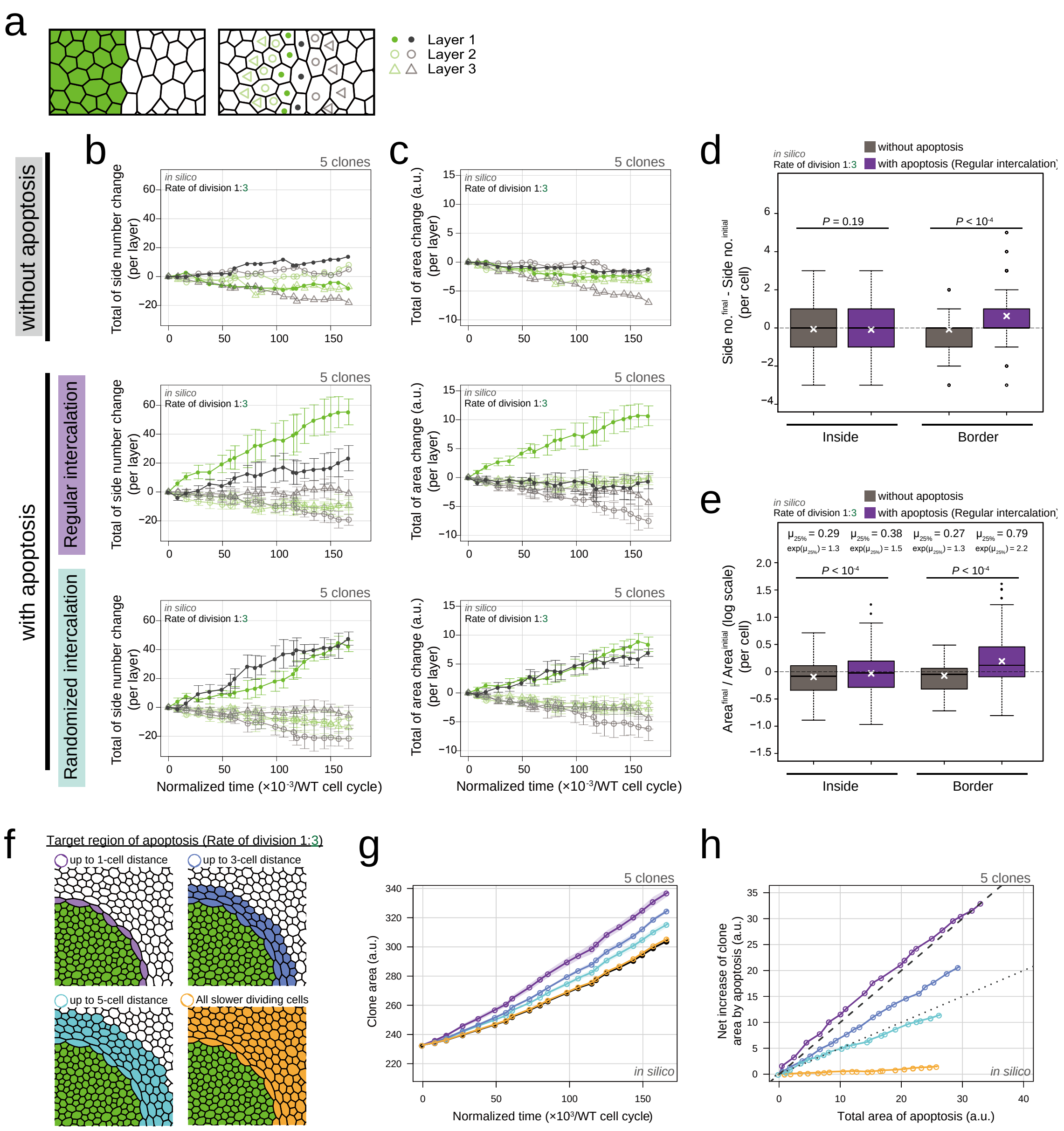

Fig. S2.7. Robust expansion of winner cells occurred under repetitive apoptosis during long-term clone development (related to Fig. 2.7)

(a–e) Apoptosis simulations, with the setting described in Fig. 2.7. **(a–c)** Sum of changes in side number (b) and cell area (c) per indicated layers, which are classified according to the location in relation to clone boundary (a), with layer 1 (cells located immediately adjacent to the clone boundary), layer 2 (cells next to layer 1), and layer 3 (cells next to layer 2). **(b, c)** Green and gray lines represent faster and slower dividing cells and different markers represent different layers defined in (a). Layers are identified at every time point. Error bars represent s.d. of five simulations of each clone at each simulation setup. **(d, e)** Difference between the final and initial side number per cell (d) and fold change in cell area per cell (e; log scale) in the presence and absence of apoptosis. See the definition of the criteria and simulation setups for Fig. 2.7b. Box plot setup is identical to that in Fig. 2.2f, f'. $\mu_{25\%}$ is average of the values ranked in the top 25% for each box plot in e. Wilcoxon rank sum testing was performed. **(f–h)** Winner-clone expansion varied depending on the spatial distribution of apoptosis. The division rate ratio (clonal/non-clonal = 3) and total numbers of apoptosis events (about 40 cells) were the same for all panels. Simulation setups other than the target regions of apoptosis were the same as in Fig. 2.7. **(f)** Slower dividing cells for targeting apoptosis are marked in purple (directly adjacent to clone boundary), blue (up to 3-cell distance away from clone boundary), light-blue (up to 5-cell distance away from clone boundary), and orange (all slower dividing cells). Apoptotic cells were randomly selected from these regions. All faster dividing cells are marked in green. **(g)** Temporal change in clone area. The line colors (purple, blue, light-blue, orange) are as in (f). The black line is the case without apoptosis, which is the same as in Fig. 2.7c. **(h)** The net increase in clone area due to apoptosis was calculated by subtracting the clone area from that value in the absence of apoptosis as a function of total area of apoptosis. Dashed/dotted lines indicate cases in which winner clones capture 100%/50% of the territory made available by apoptosis.

3. Inference of Cell Mechanics in Heterogeneous Epithelial Tissue Based on Multivariate Clone Shape Quantification

Some figures in this thesis (Fig. 3.1, Fig. S3.1, S3.2, S3.4, S3.11) were obtained in collaboration with my colleague, D. Umetsu. I clarified my own contribution in each caption.

3.1. Abstract

Cell populations in multicellular organisms show genetic and non-genetic heterogeneity, even in undifferentiated tissues of multipotent cells during development and tumorigenesis. The heterogeneity causes difference of mechanical properties, such as, cell bond tension or adhesion, at the cell–cell interface, which determine the shape of clonal population boundaries via cell sorting or mixing. The boundary shape could alter the degree of cell–cell contacts and thus influence the physiological consequences of sorting or mixing at the boundary (e.g., tumor suppression or progression), suggesting that the cell mechanics could help clarify the physiology of heterogeneous tissues. While precise inference of mechanical tension loaded at each cell–cell contacts has been extensively developed, there has been little progress on how to distinguish the population-boundary geometry and identify the cause of geometry in heterogeneous tissues. In collaboration with D. Umetsu, I developed a pipeline by combining multivariate analysis of clone shape with tissue mechanical simulations. Clones with four different genotypes within Drosophila wing imaginal discs was examined: wild-type, *tartan* (*trn*) overexpression, *hibris* (*hbs*) overexpression, and *Eph* RNAi. Although the clones were previously known to exhibit smoothed or convoluted morphologies, their mechanical properties were unknown. By applying a multivariate analysis to multiple criteria used to quantify the clone shapes based on individual cell shapes, I found the optimal criteria to distinguish not only among the four genotypes, but also non-genetic heterogeneity from genetic one. The efficient segregation of clone shape enabled us to quantitatively compare experimental data with tissue mechanical simulations. As a result, the mechanical basis contributed to clone shape of distinct genotypes was identified. The present pipeline will promote the understanding of the functions of mechanical interactions in heterogeneous tissue in a non-invasive manner.

3.2. Introduction

There are intrinsic differences among cells within any population, even in genetically uniform populations such as clonal populations of bacteria, yeasts, and undifferentiated plant and animal cells (Eldar and Elowitz 2010; Elowitz 2002; Itzkovitz et al. 2011; Meyer and Roeder 2014; Raj and van Oudenaarden 2008; Raser 2004). The non-genetic (isogenic) heterogeneity stems from intrinsic noise due to stochastic fluctuations in gene expression and extrinsic noise due to stochastic changes in upstream signal transduction (Paulsson 2004; Shibata and Fujimoto 2005). Theoretical and experimental discrimination between intrinsic and extrinsic noise (Elowitz 2002; Swain, Elowitz, and Siggia 2002) promoted an understanding of not only the molecular mechanisms but also the functional significance of the non-genetic heterogeneity (Eldar and Elowitz 2010; Raj and van Oudenaarden 2008). Genetic heterogeneity in tissues arises from spontaneous mutations in cell lineages. The emergence of cellular heterogeneity in epithelial tissues alters the morphology of the boundaries between neighboring populations and thereby affects the cellular geometry in the tissue. Alterations of the geometrical cellular configuration between clonal populations (clones) often have physiological consequences. Clonal segregation caused by Eph receptors has been shown to play a tumor-suppressive role in colorectal cancer by compartmentalizing the cancer cells and thereby limiting their invasion into normal tissues (Cortina et al. 2007; Porazinski et al. 2016). In the context of the cell competition, known as the tissue homeostatic system, to eliminate unfit cells from heterogeneous populations (Amoyel and Bach 2014; Morata and Ballesteros-Arias 2015; Vincent et al. 2013), the intermingling of cells at clonal boundaries facilitates the competition by increasing the contact length between competing genotypes, so-called winner and loser cells (Levayer et al. 2015; Levayer and Moreno 2016). Those insights suggest the potential to predict physiological consequences (e.g., tumor malignancy) based on the quantification of clone shapes. Therefore, the establishment of a pipeline that combines the quantification of clone shapes with an analysis of the physical mechanisms underlying the clone shapes would be beneficial.

A major contributing factor for clone shape is mechanical interactions at the cell-cell interface. Cell-cell adhesion mediated by adhesion molecules and contractility exerted by the actomyosin network contribute to the tension on the cell-cell interface (Lecuit and Lenne 2007). The differential adhesion and contractility among genetically heterogeneous cells have been experimentally shown to play a major role in cell segregation by driving or guiding cell rearrangements (Krieg et al. 2008; Maitre et al. 2012; Maître et al. 2016; Nose, Nagafuchi, and Takeichi 1988). The role of such mechanical cell-cell interactions on cell sorting has been also theoretically studied using computer simulations of tissue mechanics (Brodland 2002; Graner and Glazier 1992). More recently, experimental evidence in combination with models has shown that the alteration of boundary morphology can be explained by the tissue anisotropy of mechanical tension at the cell-cell interface (Aliee et al. 2012; Landsberg et al. 2009; Monier et al. 2010; Rudolf et al. 2015). The relative strength of such mechanical tension (or stress) has been estimated non-invasively from time lapse of cell shape dynamics (Brodland et al. 2010; Chiou, Hufnagel, and Shraiman 2012; Ishihara and Sugimura 2012; Nier et al. 2016) or images of fixed tissue (Brodland et al. 2014), and invasively using physical perturbation (e.g., laser ablation of cell junctions) [(Sugimura, Lenne, and Graner 2016), and reference therein]. Moreover, a recent study showed that the “clone tension,” which is defined by the average strength of the junctional tension inside and on the border of the clone relative to that on the outside, uniquely distinguishes smoothed and convoluted clone shapes (Bosveld, Guirao, et al. 2016). Hence, reliable quantification of clone shape should make it possible to identify the averaged strength of tensions in heterogeneous tissue.

Although several quantification methods for clone shape, such as circularity (Chang et al. 2011; Milán, Pérez, and Cohen 2002) and cell mixing index (Levayer et al. 2015; Umetsu, Aigouy, et al. 2014), have been established, each has been applied only independently. It is not known whether those methods can be applied to any clone shape or are suited for some particular clone shape. Moreover, it has been unknown whether such methods are sufficient to distinguish clone shapes or the other methods (e.g. cell area) are required. The combinatorial use of multiple quantitative methods would more reliably evaluate the clone shapes of various genotypes.

This study provides a pipeline to quantify the clone shape difference and identify the cause of the difference by combining a multivariate quantitative analysis of clone shape with computer simulations of tissue mechanics (Fig. 3.1A). Using fixed *Drosophila* wing imaginal discs, I and my colleague D. Umetsu examined four genotypes (wild-type control, *tartan* (*trn*) overexpression, and *Eph* RNAi, *hibris* (*hbs*) overexpression), which exhibit smoothed or convoluted clone morphologies yet have unknown cell mechanical properties. Clones that overexpress *Drosophila trn*, which encodes leucine rich repeat-containing transmembrane proteins (Milán et al. 2001, 2002; Sakurai et al. 2007), adopt a smooth shape. The knockdown of *Eph*, which encodes tyrosine kinases of the Eph receptor protein family, also generates round clones (Umetsu, Dunst, and Dahmann 2014). In contrast, the overexpression of *hbs*, an immunoglobulin superfamily member, leads to the separation of the *hbs*-overexpressing cells and their partial mixing into surrounding cells (Bao et al. 2010), resulting in a convoluted clone morphology. I used multiple cell-based criteria to quantify the clone morphology. While no single criterion alone was able to distinguish all four genotypes, by combinatorial use of multiple criteria, I distinguished the four genotypes with optimal criteria. Based on the quantitative criteria, I compared experimental results with vertex model simulations, which I explored in a wide range of differential tensions. The comparison enabled us to estimate different contribution of clone tensions and tension parameters to clone morphologies of distinct genotypes, noting that the force inference of individual cells over entire tissue is beyond the scope of the present paper. The present multivariate clone shape quantification could be extended to estimate genetic and non-genetic cell mechanics of heterogeneous populations (e.g. tumorigenic environment) in a non-invasive manner.

3.3. Material and Methods

3.3.1. *Drosophila* strains and genetics

y w hs-flp; DE-Cad::GFP; Act>CD2>GAL4, UAS-DsRed was used as the tester-stock genotype in experiments. The tester stock with RNAi lines were crossed and raised the offspring at 25 °C for 3 days. The offspring were subjected to heat shock at 37 °C for 40 min to induce somatic clones (Fig.

3.1K). The larvae were subsequently kept at 25 °C for 3 days before dissection. The following transgenic strains were used in this study: UAS-*trn* (Sakurai et al. 2007), UAS-*hbs* (Dworak et al. 2001), and UAS-ds-*Eph* (Vienna stock center, 4771). The construction of strains and cross experiments were performed by my collaborator Dr. D. Umetsu. Hereafter, I refer to the *Drosophila* tester-stock clone as the wild-type.

3.3.2. Immunohistochemistry

Larvae were hand dissected to obtain wing imaginal discs, which were fixed in PBS with 4% formaldehyde for 40 min at room temperature. The fixed samples were washed three times with PBT (PBS with 0.1 % triton) and mounted them on a glass slide. Immunohistochemistry experiments were performed by my collaborator Dr. D. Umetsu.

3.3.3. Imaging and image processing

Images were obtained with a Leica SP8 confocal scanning microscope with a 40× NA 1.30oil objective. Adherens junctions were visualized with the localization of a GFP knock-in for DE-Cadherin (Huang et al. 2009) and used them for image segmentation. The GFP signals derived from columnar cells of the wing pouch were manually selected before making a z-stack projection. The z-stack images were projected by the maximum projection in Fiji (http://fiji.sc) and used them for further quantitative analysis. Average pixel size for each cell junction was 8.4 (Fig. S3.11).

3.3.4. Clone shape quantification

Segmentation, cell tracking, and bond tracking (Fig. 3.1P-S) were performed using the ImageJ plugin Tissue Analyzer (Aigouy et al. 2016). The clones were projected onto the segmented images and identified cells in the clones using Tissue Analyzer. Possible error rates were roughly estimated by having 5 unexperienced individuals hand-correct a segmentation mask for one of the images used in this study. The error rate was estimated in 4 ways as follows (Fig. S3.4); 1) the mean rate of hand-corrections made after auto-segmentation (0.84 % of all cell junctions), 2) the mean rate of hand-corrections made by another person after the 1st round of hand-correction (0.28 % of all cell junctions), 3) the mean rate of hand-correction made by 1st and 2nd round of hand-correction in total (1.12 % of all cell junctions), and 4) the mean final discrepancy rate between 2 individuals (0.23 %, max. 0.44 %). Note that the correction rate highly depends on original image quality therefore the rate would be variable among images.

The clone shapes was quantified using multiple criteria. Circularity is a measure that calculates the ratio between the perimeter and the area of a clone and has been used to evaluate clone shapes (Fig. 3.1C). The following cell-based criteria were also used: cell area (Fig. 3.1D), cell edge length (Fig. 3.1E), clone boundary angle (Fig. 3.1F), and three types of cell mixing index (Fig. 3.1G) [i.e., mutant

(MT; Fig. 3.1H), boundary of mutant (BDMT; Fig. 3.1I), and boundary of wild-type (BDWT; Fig. 3.1J)].

3.3.5. Principal Component Analysis (PCA)

I performed PCA of the multi-dimensional criteria for clone shape using the R environment for statistical computing (R Development Core Team 2015) with the “prcomp” function. The results were plotted using the “ggbiplot” function (R package version 0.55. http://github.com/vqv/ggbiplot). PCA was applied to both open and closed clones in the wing imaginal discs using the six criteria (Fig. 3.1D–J) excluding circularity. I standardized the variables to have zero mean and unit variance before the analysis. Factor loadings (Fig. 3.3K), which were given by the correlation coefficient between observed variables (criteria) and principal components (PCs), represent the contribution of criteria on PCs. The range of the value is -1.0 to 1.0. The value of -1.0 and 1.0 for the criteria indicates a perfect negative and positive correlation with the PCs, respectively.

3.3.6. Cell vertex model

The cell vertex model quantitatively accounts for the packing geometry of normal epithelial cells and predicts the forces that act at cell-cell interfaces, where cell configurations are described as polygons whose vertices form tri-cellular junctions subjected to mechanical force [(Farhadifar et al. 2007; Gibson et al. 2011; Honda 1983); Fig. 3.1A]. The model can reproduce stable force balance configurations of the adherens junctions network, which depend on mechanical parameters characterizing the cell bond tension and apical area contraction. Cells change their shape based on the force balance of cell packing. The model is represented by balance of three types of mechanical force exerted on a vertex (Farhadifar et al. 2007):

$$\frac{d\vec{x_\iota}}{dt} = F_{area\ elastisity} + F_{tension} + F_{contractility} = -\frac{\partial E}{\partial \vec{x_\iota}}$$

$$E = \frac{1}{2}\sum_{\alpha}(a_\alpha - 1)^2 + \gamma \sum_{<i,j>} l_{ij} + \frac{\eta}{2}\sum_{\alpha} {l_\alpha}^2 \qquad (1),$$

where x_i and E are the position vector of each vertex and the energy function. $F_{area\ elasticity}$ denotes the area elasticity, which decreases as the area of cell α (a_α) approaches the normalized preferred area of unity. The line tension ($F_{tension}$) between vertices i and j (l_{ij}) is provided by the cell-cell adhesion mediated by adhesion molecules and the contractility exerted by actomyosin. The contraction ($F_{area\ elasticity}$) of the cell perimeter l_α is provided by actomyosin ring. I set the contractility parameter η = 0.04 and the line tension parameter γ = 0.12 as the control values to account for the cell packing geometry in *Drosophila* wild-type clones (Farhadifar et al. 2007). The line tension at the clone boundary (γ_b) and at the inner clonal edges (γ_c) can differ from γ. Each clone was generated from a single cell by dividing them to be 40 cells in total, which is close to the average number of cells in *Drosophila* wild-type clones. I performed 5 independent simulations for each parameter by changing the seed of the random number generator.

I integrated the vertex model numerically using the Euler method with free boundary conditions. To achieve a mechanical equilibrium of the tissue state, I calculated the position vector of each vertex after each step until the total velocity of all vertices dropped below a threshold of 1.0. The cell division time (cell cycle) t of each cell in the cell vertex model obeys a Gamma distribution with the following probability densities: $p(t) = t^{k-1}exp(-kt/\bar{T})(\bar{T}/k)^{-k}/\Gamma(k)$, where $\Gamma(k)$ is the gamma function with k = 25.0 (Mumcu 2011). The average and standard deviation are given by $\bar{T}$ and $\bar{T}/\sqrt{k}$, respectively. Cells were divided when the residence times in the cell cycle became zero. Although the cell area decreases to half the original cell area after cell division, it increases as the cell achieves a mechanical equilibrium of energy (Eq. 3.1). The mitotic cleavage-plane orientation obeys the long axis rule (Bosveld, Markova, et al. 2016; Gibson et al. 2011), where the plane passing through the shorter axis is defined by calculating the inertial tensor of each cell using the positions of the vertices (Fletcher et al. 2013). Cell intercalation (T1 transition) was incorporated when the edge length dropped below a threshold of 0.01. Apoptosis (T2 transition) was introduced into triangular cells (containing 3 vertices) whose area became below a threshold of 0.03 to replace them by a single vertex. In addition, cells which were squeezed and reduced their cell area below a threshold of 0.001 were eliminated by repeating the cell topological changes (T1 and T2 transition) even if the cells containing more than 3 vertices. The number of apoptotic events (during proliferation of a clone from a single cell to 40 cells) depends on the model parameters as seen in earlier studies on homogeneous tissue (Farhadifar et al. 2007). The apoptotic rate (number of apoptotic events/cell cycle) was 0 (γ_b/γ=0.5, γ_c/γ=1.0, Fig. 3.4A(i)), 1.5 (γ_b/γ=1.0, γ_c/γ=1.8, Fig. 3.4A(ii)), 0 (γ_b/γ=0.5, γ_c/γ=1.0, Fig. 3.4A(iii)), 0 (γ_b/γ=1.0, γ_c/γ=1.0, Fig. 3.4A(iv)), 0.08 (γ_b/γ=1.6, γ_c/γ=1.0, Fig. 3.4A(v)), 0 (γ_b/γ=1.0, γ_c/γ=0, Fig. 3.4A(vi)), 0 (γ_b/γ=1.6, γ_c/γ=0, Fig. 3.4A(vii)).

3.3.7. Clone tension

Clone tension is given by the balance of line tension parameters (Eq. 3.1) at the three types of edges represented by γ, γ_b, and γ_c (Bosveld, Guirao, et al. 2016):

$$\hat{\sigma} = \frac{\partial E}{\partial L} = \gamma_b - \frac{\gamma+\gamma_c}{2} \qquad (2).$$

It represents the energy cost E (Eq. 3.1) per unit length of changes in the clone boundary length L (Fig. 3.1C) followed by cell intercalation. Because the differential of elastic energy $\partial E/\partial L$ should be negative to satisfy a stable equilibrium, the sign of the clone tension $\hat{\sigma}$ influences the evolution of the clone boundary length L. At negative $\hat{\sigma}$, boundary length change δL should be positive to increase the contact between different cell populations, leading to a convoluted clone boundary. In contrast, at positive $\hat{\sigma}$, δL should be negative to decrease the contact between different cell populations, leading to a smoothed clone boundary. I used dimensionless clone tension $\sigma = \hat{\sigma}/\gamma$ (Bosveld, Guirao, et al.

2016) in this study.

3.3.8. Projection of the simulation data onto the PCA space of the experimental data

To quantitatively compare the multivariate clone shape data from genetic experiments with the vertex model simulations in the PCA space constructed from the experimental data (Fig. 3.1A), the simulation clones (see Section "Cell Vertex Model" for induction of clones) were quantified by an identical set of quantitative criteria with experiments (Fig. 3.1D-J). Subsequently, I subtracted the clone shape dataset for each criterion in simulations from the mean of that in the four genotypes and divided the subtracted values by the standard deviation of that in the genotypes. I calculated the first PC scores (Y_1) of the scaled simulation data ($X_1, X_2, \ldots., X_n$) by $Y_1 = a_{11}X_1 + a_{12}X_2 + \ldots + a_{1n}X_n$, where $a_{11}, a_{12}, \ldots, a_{1n}$ are the weights (Table S3.1 in Supporting Materials) of four genotypes with $n = 6$ (number of criteria; Fig. 3.1D–J). The weights are given by the first column of the PC matrix, which contains variable loadings whose values are returned by "rotation" in the prcomp function in R. The second PC scores are given in the same way by using the second column of the matrix. I projected the calculated first and second PC scores onto the experimental PCA space using the "ggplot2" function in R (Wickham 2009). The PC scores in simulation were averaged over the clones categorized by the number of consisting cells (every 5 cells) since the clone size was varied due to fragmentation of a single clone caused by T1 transitions in a simulation.

3.3.9. Estimation of the mechanical parameters of the genetic experiments in the PCA space

I determined the estimated mechanical parameters by simulation plots inside a confidence ellipse, which I drew by assuming that the experimental plots of each genotype followed the multivariate normal distribution. I selected the best representative parameters for each genotype by identifying the shortest Mahalanobis distance from the center of the confidence ellipse.

3.4. Results

3.4.1. Clone shape quantification

I adopted several geometrical indicators (Fig. 3.1B–J, S3.1, S3.2) to quantitatively evaluate the shape of mosaic clones of distinct genotypes induced in the wing discs (Fig. 3.1K–O). First, I calculated the circularity of each clone (Section "Clone Shape Quantificatio"; Fig. 3.1C, 3.2, and S3.1). The average circularity of the *trn*-overexpression clones, which exhibited a round shape with a smooth border (Fig. 3.1M), was significantly greater than that of the wild-type clones, as reported previously (Fig. 3.3A; (Milán et al. 2002)). In the other genotype, *hbs*-overexpression clones, circularity was distinct from that of the wild-type clones (Fig. 3.3A). The cells overexpressing *hbs*, however, scattered into many single-cell clones (Fig. 3.1O and S3.3), so the circularity of the single-cell clones represented merely the shape of cells, and not that of clones. Moreover, circularity cannot be applied to open clones located at the edges of the images, because the perimeter length and area of those clones cannot be precisely determined (Fig. 3.2, uppermost panels and white-colored clone in Circularity panels). Circularity can be applied only for clones with closed circumference and is therefore measurable only for those clones with a relatively small number of cells located in the middle of the tissue, and the entire clone should lie within the image frame (Fig. 3.2, uppermost panels). In the *Drosophila* wing discs, which are frequently used for mosaic clone analysis, approximately half of the clones were open clones (46.4% for wild-type clones). Therefore, a cell-based analysis to quantify the clone shape was needed.

In order to quantify clone shape at the single-cell level, the individual cell shapes were precisely traced (segmented) and labeled using Tissue Analyzer [(Aigouy et al. 2016); Section “Clone Shape Quantificatio”; Fig. 3.1P–S], which has a sufficiently low error rate of image segmentation (Fig. S3.4). For the segmented images, I measured the cell mixing index, which has been used to quantitatively evaluate how much a single cell shares junctions with a neighboring population (Levayer et al. 2015; Umetsu, Aigouy, et al. 2014)(Fig. 3.1G–J, 3.2, and S3.1; MT, BDMT, and BDWT). Remarkably, the MT and BDMT of the *hbs*-overexpression clones were significantly higher than those of the wild-type clones (Fig. 3.3E–F). In order to test whether the cell mixing index is sensitive enough to distinguish clone shapes with different smoothness, I compared *Eph*-RNAi clones (Fig. 3.1N, R) with *trn*-overexpression clones (Fig. 3.1M, Q); however, none of the indices (MT, BDMT, and BDWT) was able to distinguish between the *Eph*-RNAi clones and the *trn*-overexpression clones (Fig. 3.3E–G). The boundary angle (Fig. 3.1F) was also unable to separate the *Eph*-RNAi and *trn*-overexpression clones, although it could distinguish the *Eph*-RNAi or *trn*-overexpression clones from the wild-type clones (Fig. 3.2 and 3.3D). The edge length (Fig. 3.1E) was not able to distinguish between any pair of genotypes (Fig. 3.2 and 3.3B). The cell area (Fig. 3.1D) could uniquely distinguish the *Eph*-RNAi clones from the *trn*-overexpression clones but not from the wild-type clones (Fig. 3.3C). In summary, there was no single cell-based criterion that could separate the four genotypes. The combinatory use of multiple criteria may provide a better resolution to distinguish the clone shapes of the genotypes, which could ultimately infer mechanical parameters of each genotype (Fig. 3.1A).

3.4.2. PCA separated sources of phenotypic heterogeneity

The combinatorial use of multivariate (6-dimensional) dataset increases information of data sets required for the complete separation, while the multi-dimensional information is too complex for us to intuitively extract some important criteria for the efficient separation. Therefore, multi-dimensional analysis generally has a trade-off between the merits and demerits. The principal component analysis (PCA) can optimize the trade-off: It can provide criteria to maximize the variance of the data and compresses multi-dimensional information into lower dimensions while retaining most of the original information. PCA has been extensively developed in the field of morphometrics of individual cells (Lacayo et al. 2007; Pincus and Theriot 2007), organs (Iwata 2002; Klingenberg 2011), and individual bodies (Zelditch, Swiderski, and Sheets 2012), but not of clones in multicellular tissue. I applied PCA to the data set of the six criteria for the four genotypes (n = 84 clones from six discs for wild-type, n = 61 clones from five discs for *Eph* RNAi, n = 53 clones from five discs for *trn* overexpression, n = 215 clones from six discs for *hbs* overexpression; Fig. 3.3H–K, S3.5 and S3.6). I averaged over the set of clones in each wing disc before applying PCA to analyze genetic variation separately from non-genetic variation. I found that more than 80% of the information was compressed into only two principal components (PC1 = 49.4%, PC2 = 31.9%, PC3 = 12.7%; Fig. 3.3H–J). Each genotype was separated mainly in PC1 without overlap (Fig. 3.3H), while the *Eph*-RNAi and *trn*-overexpression clones were also efficiently separated in PC2 and PC3 (Fig. 3.3H–J). The major criteria with higher factor loading on PC1 (> 0.85; see "Principal Component Analysis (PCA)" for the definition of factor loading) were MT, BDMT, and boundary angle, while some other criteria such as cell area and edge length showed a high contribution on PC2, and BDWT contributed relatively on PC1 and PC3 (Fig. 3.3K and S3.5; Table S3.1 for exact weight of each criterion on PCs). Both the separation of genotypes mainly in PC1 and the contribution of each criterion on PC1–PC2 were nearly the same "with averaging" or "without averaging" within the discs (Fig. 3.3H–K and S3.6).

Note that PCA without averaging within the discs showed that the variation within a genotype was mainly distributed in PC2, while each genotype was separated in parallel with PC1 (Fig. S3.6A). Since the variation occurred in an identical combination of clone (e.g, *Eph* RNAi) and non-clone genotypes (wild-type), hereafter I call it "non-genetic" heterogeneity (Fig. S3.1 and S3.7A, middle panels). Interestingly, PC2 had a positive correlation with the distance from the center of the disc (Fig. S3.7B), indicating that the non-genetic heterogeneity in PC2 encoded the positional information of each clone. That might be caused by spatial gradients of the expression of several genes in the *Drosophila* wing pouch (e.g, *spalt*, *optomotor-blind*, *Distalless*, and *vestigial*; (Affolter and Basler 2007; Milán et al. 2002; Swarup and Verheyen 2012). Therefore, genetic as well as non-genetic heterogeneities were efficiently segregated in lower dimensions in the PC space, allowing us to estimate the mechanical basis of the genetic heterogeneity using PCA.

3.4.3. Vertex model simulations with differential line tension

I analyzed how the mechanical cell-cell interactions contribute to the characteristic clone shapes (Fig. 3.1L–S) by comparing *Drosophila* experiments to computer simulations (Fig. 3.1A). I utilized the cell vertex model, which quantitatively accounts for the packing geometry of epithelial cells (Section "Cell Vertex Model", Eq. 3.1). Clone shape has been shown to be modulated mainly by the combination of line tension parameters at three types of edges: γ (default tension in Eq. 3.1), γ_b (clone boundary tension), and γ_c (inner clonal tension; Fig. 3.4A, right bottom panel for the classification of edges) (Brodland 2002; Graner 1993; Graner and Sawada 1993). Therefore, as a pilot study for the multivariate inference of mechanical parameters for each genotype, I presupposed that γ_b and γ_c

relative to γ are the main causes of clone formation, although other parameters such as the rate of cell proliferation might potentially influence the clone boundary shape (see Fig. S3.3 for detailed data on the numbers of cells and clones). I numerically explored the role of the different combinations of line tension parameters γ_b and γ_c in the formation of clones. As the tension parameter for clone boundary γ_b increased relative to the control tension parameter γ, cells were sorted out so that the clone boundary became smoothly rounded (Box1 in Fig. 3.4C), as seen previously (Aliee et al. 2012; Bosveld, Guirao, et al. 2016; Landsberg et al. 2009; Monier et al. 2010; Rudolf et al. 2015). I observed a similar tendency to generate smooth clones by decreasing the inner clonal tension parameter γ_c relative to γ, which is equivalent to increasing adhesion between the inner clonal cells (Box2 in Fig. 3.4C). Conversely, cell mixing occurred to form convoluted clones as γ_b decreased or γ_c increased relative to γ (Fig. 3.4C). Those results indicate the differences between the default tension (γ) and the one at the clone boundary and inside the clone (γ_b and γ_c) reflect cell sorting and cell mixing. As a measure to distinguish between cell sorting and mixing, I examined the dimensionless clone tension, which is represented by γ, γ_b, and γ_c (σ in Section "Clone Tension") (Bosveld, Guirao, et al. 2016). I confirmed that negative and positive values of the clone tension (Fig. 3.4B, grey and light-grey, respectively) mainly distinguished convoluted and rounded clone morphologies, respectively (Fig. 3.4C).

3.4.4. Inference of tension parameters by comparison between experiments and simulations in the PC space

I quantitatively compared the clone shapes generated by vertex model simulations using the control parameters [$\gamma = \gamma_b = \gamma_c$, Fig. 3.4A(iv)] to those of *Drosophila* wild-type clones by projecting the simulated clones onto the PC1 and PC2 space of the experimental data (Fig. 3.3H). The simulated control clones (Fig. 3.5A, black octagonal asterisk at PC1 ~ 1.07, PC2 ~ 0.56) were consistently similar to the wild-type clones in the PC space (Fig. 3.5A red confidence ellipse). I inferred the wild-type tension parameters from the simulations plotted inside the 68% confidence ellipse of the wild-type clones (Section "Estimation of the Mechanical Parameters of the Genetic Experiments in the PCA Space"). The estimated parameters of the wild-type clones were distributed around the control parameters of the simulation (Fig. 3.5B, red), where the clone tension was nearly zero (Fig. 3.5B, solid line, and 5C, red), indicating that the vertex model could closely coordinate with the PCA of static tissue images to non-invasively estimate the mechanical parameters of the wild-type clone based only on the clone morphology.

Likewise, when I simultaneously projected simulation data from a wide range of tension parameter sets (all marks in Fig. 3.4B) onto the PC space, I found that the two-dimensionality of the parameter space of the line tension (γ_c/γ and γ_b/γ; Fig. 3.4B) was maintained in the PC1-PC2 space (Fig. 3.5A), indicating a quantitative link between the tension parameters at the cell-cell interface and the clone boundary geometry of heterogeneous populations. Therefore, following the methods applied to the wild-type clone, I estimated the mechanical parameters of the other three genotypes (*Eph* RNAi, *trn* overexpression, and *hbs* overexpression). I found that the estimated regions of the mechanical parameters for each genotype (plotted inside the 68% confidence ellipses in Fig. 3.5A) were distributed in parallel to the contour lines of the clone tension (Fig. 3.5B). For the *Eph*-RNAi and *trn*-overexpression clones, which had a rounded morphology (Fig. 3.1M, N), the tension of both clones was higher than that of the wild-type clone (Fig. 3.5C). The *hbs*-overexpression clones had a negative value for clone tension (Fig. 3.5C), which was consistent with their convoluted morphology (Fig. 3.1O). The ascending order of clone tension (*hbs* overexpression < wild-type < *Eph* RNAi < *trn* overexpression; Fig. 3.5C) perfectly agreed with that of PC1 (Fig. 3.3H), indicating that the value of PC1 reflects the difference in clone tension. To more directly relate the clone tension to the PCA, I projected the PC scores onto the parameter space of the vertex model simulations (Fig. 3.5D). The contour of the PC1 scores was almost parallel to that of the clone tension (Fig. 3.5D, red solid line), whereas that of the PC2 scores was rather perpendicular to that of the clone tension (Fig. 3.5D, dark grey solid line), indicating that the clone tension was the mechanical basis of PC1.

To better estimate the tension parameters γ_b and γ_c, I defined the simulation plots closest to the centers of the confidence ellipses (Fig. 3.5A) as the best representative combinations of line tension parameters for each genotype (pentagonal asterisks in Fig. 3.5B; Fig. 3.6). I confirmed that the representative parameters γ_b and γ_c in simulations quantitatively reproduced experiments of each genotype according to all clone shape criteria used in PCA (Fig. S3.8A and S3.9A, left most panels). The representative parameters indicated that the cause of the higher clone tension was different between the *Eph*-RNAi clones and the *trn*-overexpression clones. The difference was mainly caused by dominantly reduced γ_c relative to γ for the *Eph*-RNAi genotype and both reduced γ_c and increased γ_b relative to γ for the *trn*-overexpression genotype (Fig. 3.5B). The lower clone tension of the *hbs*-overexpression clones was caused by dominantly increased γ_c relative to γ (pentagonal asterisk in Fig. 3.5B).

At a constant clone tension for each genotype estimated by PC1, PC2 is sensitive to the combination of γ_b and γ_c (e.g., $-4 \leqq \mathrm{PC2} \leqq 2$ at clone tension = -0.2 in Fig. 3.5D), so that the dominant change of γ_b or γ_c relative to γ was determined according to PC2 value of each genotype. The underlying mechanics how PC2 distinguished the dominance can be understood from the mechanical equilibrium of vertex model; edge length at clone boundary and cell area inside clones, which had higher contribution to PC2 (Fig. 3.3K), become smaller as line tension strength γ_b and γ_c at constant clone tension increase in simulations (Fig. S3.10). Thus, the mutual projection of the mechanical parameter space and the PC space could efficiently and quantitatively estimate the distinct mechanics of the various clone morphologies.

3.5. Discussion

3.5.1. Multivariate analysis of clone shapes

First a PCA of clone shapes in heterogeneous cell populations was developed, which efficiently segregated clones of each genotype in the PC space. No single cell-based criterion of clone shape was able to perfectly segregate all four genotypes (Fig. 3.3). In addition, because most of the conventional ways to quantify clone shape used in previous studies can only apply to closed clones (e.g., circularity, Fig. 3.1C), much information regarding open clones (e.g., white clones in Fig. 3.2) was previously lost during the quantification process. Open clones are frequently observed, however, in tissue specimens. The cell-based criteria that I used (Fig. 3.1D–J) can apply to not only closed clones but also open clones, so they can be used widely and independently on the clone shapes and its location in the tissue. Furthermore, the average pixel size for each cell junction was only 8.4 (Fig. S3.11), suggesting the relatively low resolution imaging data is sufficient to distinguish clones of different genotypes with a minimal manual correction (1.12%, Section “Clone Shape Quantificatio” and Fig. S3.4). Therefore, this cell-based quantification provides a robust method for the clone shape quantification.

Both genetic and non-genetic heterogeneities influence tumorigenesis (Cortina et al. 2007; Porazinski et al. 2016), cell competition, and other events. Elimination of loser cells at the clone boundary during cell competition has been shown to be driven by genetic heterogeneity (Amoyel and Bach 2014; Morata and Ballesteros-Arias 2015; Vincent et al. 2013), while not all of loser cells are eliminated indicating the non-genetic heterogeneity due to local cell-cell contacts and gene expression levels in tissues might affect the elimination (e.g, Fig. 3.1 in (Levayer et al. 2015); (Chen et al. 2012; Froldi et al. 2010; Kajita et al. 2014)). The PCA applied to individual clones efficiently separated the genetic heterogeneity mainly in PC1, while the non-genetic heterogeneity was distributed in PC2 (Fig. S3.6 and S3.7), indicating that PC1 and PC2 encode genetic and non-genetic heterogeneities, respectively. That in turn indicates that the criteria with high contributions on PC1 (BDMT, MT, and boundary angle) and PC2 (BDWT, cell area, and edge length; Fig. S3.6D) optimally indicate the genetic and non-genetic heterogeneity, respectively, for the four genotypes in this study. The determination of whether those criteria commonly distinguish between genetic and non-genetic heterogeneity in other genotypes in the future will give clues as to how to separately evaluate genetic and non-genetic contributions to physiological functions of heterogeneous tissue.

3.5.2. Non-invasive estimation of cell mechanics

I non-invasively estimated the mechanical parameters (i.e., clone tension and line tensions) of each genotype by integrating in a PC space the results of vertex model simulations and the quantified clone shapes in static images of cells (Fig. 3.5A and S3.12). As a case study for rounded clones, I revealed that *trn*-overexpression clones have greater clone tension than *Eph*-RNAi clones (Fig. 3.5C). Despite the patterned expression and the known, spatially graded function of *trn* in the wing pouch (Milán et al. 2002), this method successfully captured the characteristic features of *trn* overexpression, which are significantly distinct from those of *Eph* knockdown (Fig. 3.3H–K). That suggests that this method can be applied to the coarse classification of clones with distinct genotypes even in the presence of non-genetic variation derived from a spatial gradient.

I also confirmed that the clone tension of the wild-type was nearly zero (Fig. 3.5C). In addition, the range of clone tension for the other genotypes was also close to that measured previously ($0 < \sigma < 0.6$) (Bosveld, Guirao, et al. 2016), despite the fact that different genotypes was used (Fig. 3.5C). In addition, difference of the estimated clone tension (asterisk of Fig. 3.5C) among genotypes was larger than the variation within each genotype (box height of each plot in Fig. 3.5C), which was also confirmed by the estimation precision of clone tension [±0.15 (wild-type), under ±0.1 (*Eph*), ±0.1 (*hbs*), ±0.2 (*trn*) calculated from estimation precision of γ_b and γ_c in Fig. S3.8 and S3.9 using Equation 2]. The results indicate that the estimated values were roughly correct and that this method works well to estimate the mechanics. Moreover, this study first showed *in vivo* that negative clone tension causes a convoluted morphology by inducing *hbs*-overexpression clones (Fig. 3.5C).

Our study revealed the cell mechanics, relative contributions of γ_b or γ_c to the increase or decrease in clone tension. By examining the underlying cell mechanics, I found that the relative contributions of the line tension parameters γ_b and γ_c were different among genotypes, even when the sign of the clone tension was the same. Estimation precision of γ_b/γ for each genotype was evaluated by a limit to how much shift of γ_b/γ from the best representative (pentagonal asterisks in Fig. 3.5B) simulation could reproduce experimental data; It was at most ±0.2 [under ±0.1 (*Eph, hbs*), ±0.1 (wild-type), and ±0.2 (*trn*)] (Fig. S3.8), whereas estimation precision of γ_c/γ was at most ±0.3 [±0.1 (*Eph*), ±0.2 (*hbs, trn*), and ±0.3 (wild-type)] (Fig. S3.9). The estimated parameter variation of γ_b/γ and γ_c/γ for each genotype (68% confidence, dark and light colors in Fig. 3.5B) was consistently smaller than difference of the best representative parameters between genotypes (pentagonal asterisks in Fig. 3.5B). The *Eph*-RNAi clone had decreased bulk line tension, whereas the *trn*-overexpression clone had both increased boundary tension γ_b and decreased γ_c (pentagonal asterisks in Fig. 3.5B), resulting in positive clone tension. The *hbs*-overexpression clone, which showed cell mixing due to negative clone tension, mainly had increased γ_c (pentagonal asterisk in Fig. 3.5B). Cell mixing caused by increased γ_c was reported previously in *myc*-induced cell competition (Levayer et al. 2015). The inference on the dominance of γ_b or γ_c for each genotype should be verified by estimation of the mechanical tension by physical perturbation in the future (e.g., laser cutting of the three types of edges in Fig. 3.4A, right bottom panel).

3.5.3. Molecular mechanisms of cell sorting and mixing mechanics

The present estimation provides mechanical insights of the previously reported molecular functions in cell sorting (Fig. 3.5B): *Drosophila trn* and its paralogue *capricious* (*caps*) encode leucine rich repeat containing transmembrane proteins that have a function in controlling cell affinity and the regulation of cell communication for cell survival (Milan, Cell, 2001; Milan, Dev. Cell, 2002; Sakurai, Dev. Biol., 2007). The mammalian homologue, Lrrn1 is required for the formation of the midbrain-hindbrain boundary by regulating cell affinity (Tossell, Dev. Biol., 2011). Eph kinases comprise a large protein family of receptor protein tyrosine kinases. Eph receptors are activated by binding to ephrins, their membrane-anchored ligands, to transduce signals that play diverse roles in axon guidance, neural crest-cell migration, and boundary formation of rhombomeres through their function in repulsive cell-cell interactions (Fagotto, Winklbauer, and Rohani 2014; Sela-Donenfeld and Wilkinson 2005). In addition, mammalian EphB signaling plays a tumor-suppressive role by compartmentalizing cancer cells, potentially through cell-repulsive activity by means of actin cytoskeleton reorganization (Cortina et al. 2007). The result showing decreased line tension at homotypic cell junctions (γ_c) within the *Eph*-RNAi clones (Fig. 3.5B) is consistent with the previously proposed repulsive functions of Eph receptors. Therefore, this method was consistent with the previously reported cell functions. Given the common and uncommon biological functions between *trn* and *Eph*, it would be interesting to investigate how the difference in cell mechanics between the *trn*-overexpression clone and *Eph*-RNAi clone contributes to biological functions of those genes.

Our analysis showed that the overexpression of *hbs* alone can result in negative clone tension (Fig. 3.5C), which leads to convoluted clonal morphology and cell scattering. The main contribution to the negative clone tension was the increase of γ_c (Fig. 3.5B), which would be a reflection of either an increase in cortical contractility or a decrease in adhesion at homotypic cell junctions within the clone (Eq. 3.1). That suggests that the scattered morphology of the *hbs*-overexpression clones was derived from increased cell bond tension at the *hbs*–*hbs* cell interface, which is independent of the interaction between heterotypic cell junctions at the wild-type–*hbs* interface. The mechanical basis of *hbs* function has been poorly understood, except for its heterophilic interaction with the other nephrin family proteins Roughest and Kirre. This result therefore provides a new mechanical insight into the cell mixing mechanisms mediated by those proteins.

3.5.4. Future problems

In addition to line tension parameters, the clone boundary shape could be affected by inter-clonal differences in other parameters such as the cell proliferation rate, apoptosis rate, and cell division orientation, which I will incorporate into the vertex model in the future. For example, the proliferation rate appeared to be increased more often in *Eph*-RNAi cells than in wild-type cells (Fig. S3.3B). Differential proliferation rates induced by such mutants are known to cause not only clone boundary smoothing [e.g., $\textit{Ras}^{\mathrm{V12}}$-expressing (constitutively active form) cells (Prober and Edgar 2000) and $\textit{tkv}^{\mathrm{Q253D}}$-expressing (activated form of Dpp receptor) cells (Nellen et al. 1996)] but also the mechanical elongation of slower-dividing cells at the clone boundary and the compaction of faster-dividing cells [e.g., *Hippo* mutant clones in wild-type tissue (Legoff et al. 2013; Mao et al. 2013; Pan et al. 2016)], so that cell shape anisotropy, which is a new criterion for cell elongation (Legoff et al. 2013; Mao et al. 2013), as well as BDWT, clonal cell area, and other parameters might be reliable criteria for differential proliferation. The regulation of cell division orientation depends on the pathway of planar cell polarity, morphogen gradient, and mechanical cell stretching (Gillies and Cabernard 2011; di Pietro, Echard, and Morin 2016; Stooke-Vaughan, Davidson, and Woolner 2017). Specifically, misoriented or directionally oriented cell division inside or at the periphery of the clone results in a rounded or convoluted shape of the clone boundary (Kale et al. 2016; Li et al. 2009; Mao et al. 2011). Taken together, the incorporation of additional criteria is required (e.g., cell shape anisotropy) in order to precisely infer the most responsive parameters of genotypes.

According to the increasing dimensions of the parameter space, parameter estimation should be performed in the higher dimensions of the PC space. While I used the PC1-PC2 space containing 80% of the information for the current estimation (Fig. 3.5A), PC3 contained about 10% of the information, which segregated *Eph*-RNAi clones from *trn*-overexpression clones (Fig. 3.3I, J). Additionally, I could narrow down the estimated parameter region by combining this current analysis with other analyses, such as a distribution of several criteria as in the parameter estimation of homogeneous epithelial tissue (Aegerter-Wilmsen et al. 2010; Farhadifar et al. 2007). For example, *hbs*-overexpression clones showed an anomalous distribution of cell numbers within clones due to an increasing fraction of clones with smaller numbers of cells (Fig. S3.3A and S3.3C), while wild-type clones show coherent morphologies (Fig. 3.1L) due to the remarkable lack of cell rearrangement in imaginal discs (Gibson et al. 2006). That indicates that the combinatorial use of the clone size distribution (Fig. S3.13B) with PCA could estimate the parameters for *hbs*-overexpression clones in a narrower range (Fig. S3.13A, parameters covered by both blue and grey oblique lines). Future studies should also clarify the limits and applicability of the multivariate inference of cell mechanics by exploring more complex systems as well as a wider variety of genotypes.

The pipeline based on cell shape quantification developed in this study may be extended to an image-based cancer diagnosis. High-throughput microscopy image-based cancer prognosis has been developed and is expected to provide useful prognostic information for precision medicine (Yu et al. 2016). In addition to the potential contribution to such a classification of the cancer subtype or grade, this method has a potential to provide the mechanistic understanding of tumor development. Elucidation of mechanistic ground of tumor morphology may help cancer treatment planning. Moreover, manipulation of the clone tension at the interface between normal cells and cancer cells (γ_b) as well as of that between cancer cells (γ_c) can be an alternative clinical approach to suppress cancer progression either by limiting tumor invasion or by promoting cell competition.

3.6. Figures

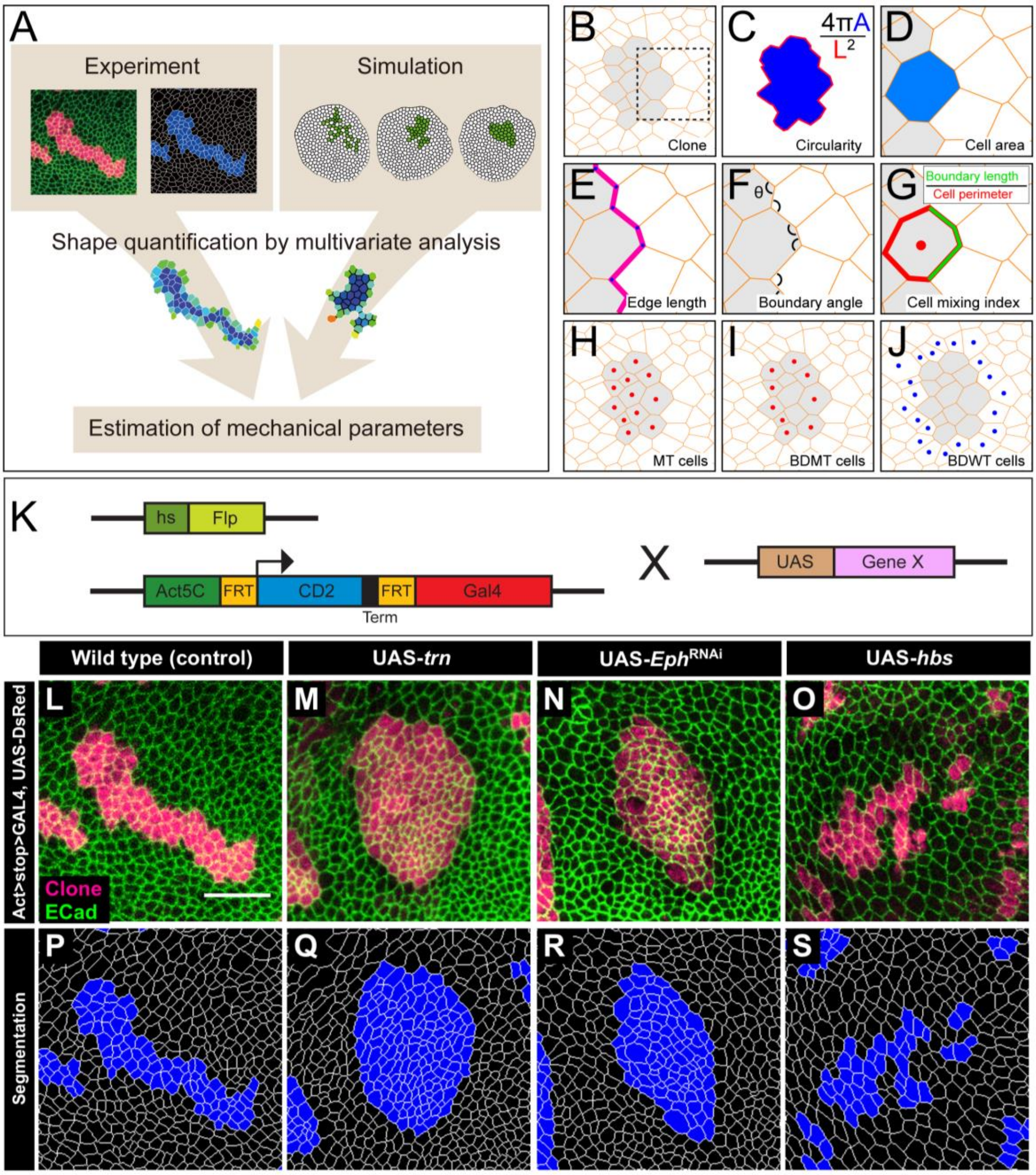

Fig. 3.1. The multivariate estimation pipeline using quantitative evaluation of clone shape. **(A)** Schematic summary of the inference procedure. **(B–J)** Criteria used for the evaluation of clone shape (Provided by D. Umetsu). Circularity (C) was measured only for closed clones, while the other six cell-based criteria (D–J) were measured for both closed clones and open clones. The cell-based criteria (D–J) were calculated for each edge, tri-cellular junction, or cell, and the values were averaged over each clone. **(B)** Scheme for a clone. Orange lines represent adherens junctions, and cells within a clone are shaded. **(C)** Circularity calculated as 4π A/(L2), where "A" represents the area of the clone, and "L" is the perimeter length of the clonal interface. The circularity of a perfect circle should be 1.

(D–G) Magnified images of the box in (B). **(D)** Area of a cell within a clone normalized by that of all wild-type cells surrounding the clone in a disc. **I** Length of edges (cell junctions between neighboring vertices) at the clone boundary normalized by that of edges between wild-type cells. **(F)** Boundary angle, which is the smaller angle (<180°) between neighboring junctions along the clone boundary at every tri-cellular junction (three-way vertices). **(G)** Cell mixing index, which is the fraction of the perimeter of a cell that is shared with cells from the other side of the clone boundary. **(H–J)** The cells used to calculate the average cell mixing index for MT, BDMT, and BDWT are marked by red dots in (H, all cells within the clone) (I, clonal cells beside the clone boundary) and blue dots in (J, wild-type cells beside the clone boundary), respectively. **(K)** Scheme for genetic manipulation used to generate the clones (Provided by D. Umetsu). GAL4 is expressed only when the CD2 cassette, which includes a transcription termination sequence and is flanked by FRT sites, is excised upon Flippase (Flp) induction by heat shock. Once expressed, GAL4 binds to the UAS sequence and drives expression of the downstream gene. **(L–O)** Clones expressing a marker for wild-type (L), trn (M), double-strand RNA against Eph (N), and hbs (O). The samples were prepared by D. Umetsu. **(P–S)** Segmentation of the cell junctions in (L–O) (Provided by D. Umetsu).

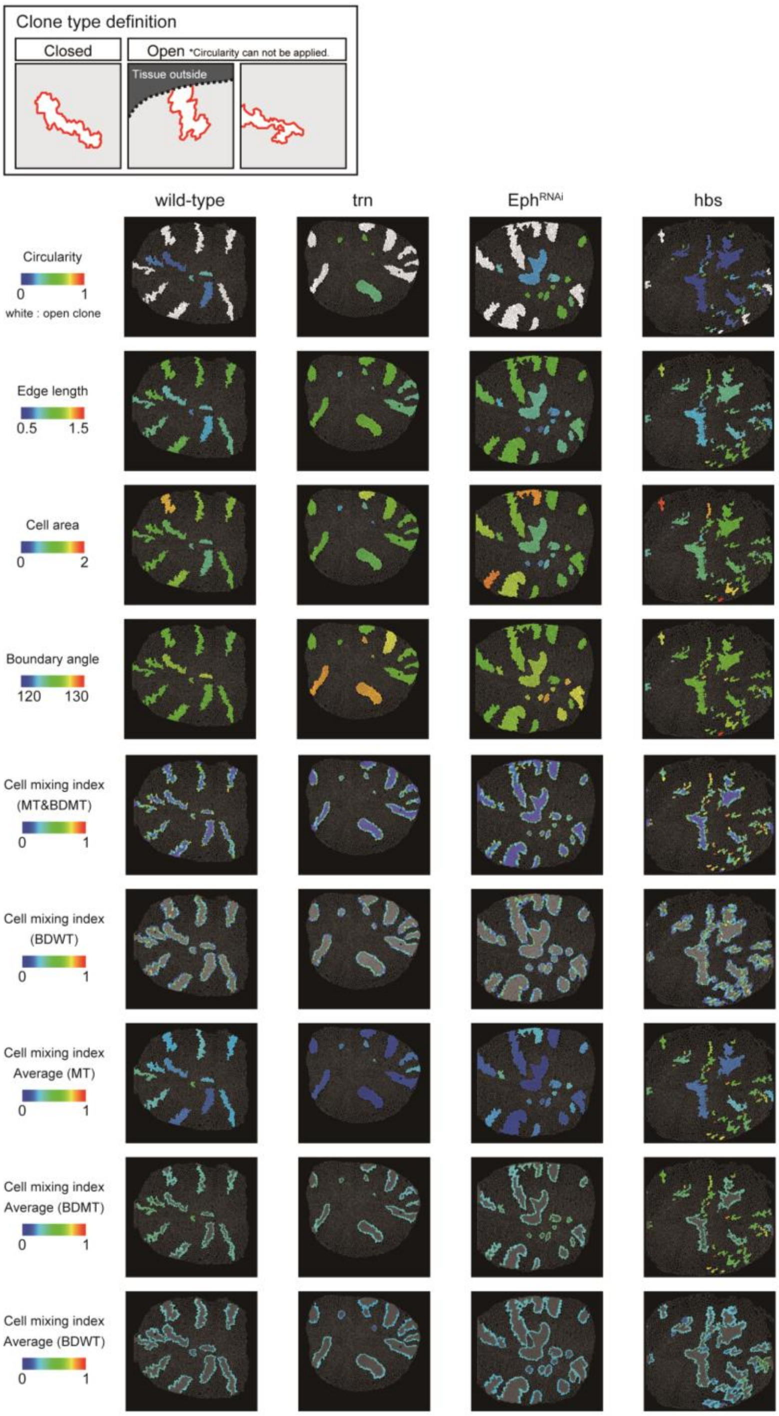

Fig. 3.2. Clone shape quantifications in wing discs.

Uppermost panels: Definition of clone type. “Closed” clone is completely enclosed by wild-type cells (left), while “Open” clone contains an invisible portion due to its location at the distal region of the tissue (middle) or image frame (right). Visualization of individual criteria (Fig. 3.1C–J) for the examined clones of four genotypes (Fig. 3.1L–O). For open clones, circularity was not measurable, so they were filled by a white color.

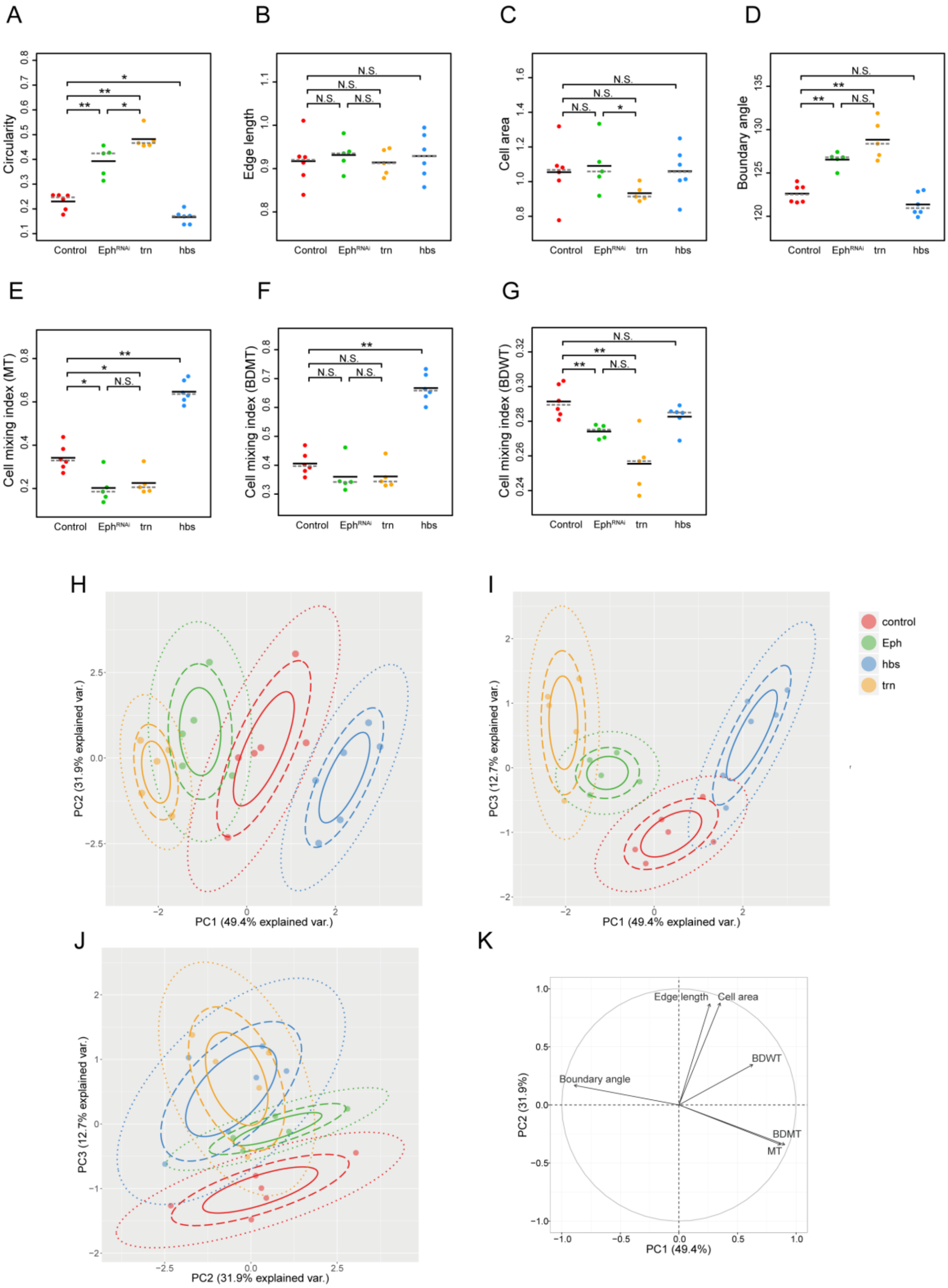

Fig. 3.3. Principal component analysis of clone shape indicators for four genotypes.

(A–G) Plots for circularity (A), edge length (B), cell area (C), boundary angle (D) and cell mixing index of MT cells (E), BDMT cells (F), and BDWT cells (G) of clones of four genotypes including wild-type (red), Eph RNAi (green), trn overexpression (yellow), and hbs overexpression (blue). The plotted data were obtained from clones with averaging within a disc. Black solid lines and gray broken lines represent the average and median values, respectively. Wilcoxon rank sum test, n = 6 for control and hbs overexpression; n = 5 for Eph RNAi and trn overexpression. **P < 0.01, *P < 0.05 and P > 0.05 (N.S., Not Significant). **(H–J)** Results of principal component analysis using six criteria (edge length, cell area, boundary angle, and cell mixing index of MT cells, BDMT cells, and BDWT cells) are plotted for PC1 vs. PC2 (H), PC1 vs. PC3 (I), and PC2 vs. PC3 (J). **(K)** Quantified contribution (factor loadings; Section "Principal Component Analysis (PCA)" for definition) of each criterion on PC1 and PC2. The arrow length represents the sum of the squared correlation coefficient of PC1 and PC2, noting that the sum of all PCs is equal to 1.

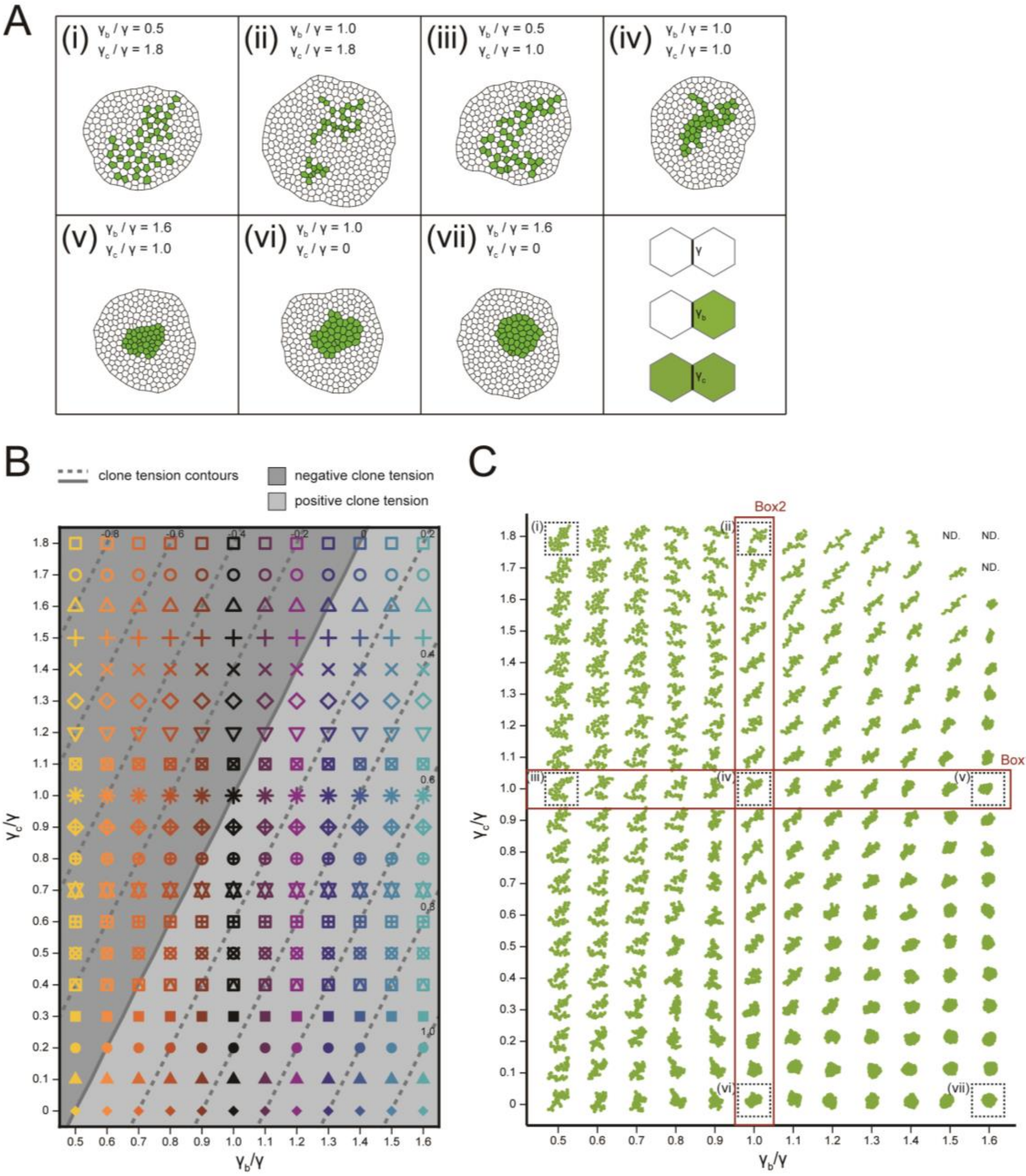

Fig. 3.4. Cell vertex model simulations.

(A) Right bottom: The classification of line tension parameters: γ [default tension at edges between non-clonal cells (white)], γ_b (clone boundary tension at edges on the clone boundary), and γ_c [inner clonal tension at edges between clonal cells (green)]. (i–vii) Snapshots of simulated clones when the total number of green cells is 40. **(B)** Parameter space of normalized line tension (γ_b/γ and γ_c/γ) with contour lines of clone tension σ (See Section "Clone Tension for definition"). Each symbol denotes different combinations of parameters (γ_b/γ, γ_c/γ). **(C)** Representative form of the clones for all simulation parameters in (B), noting that the model did not work at the three parameter points indicated by "ND." Clones enclosed within black dashed boxes are the same as those in (i–vii).

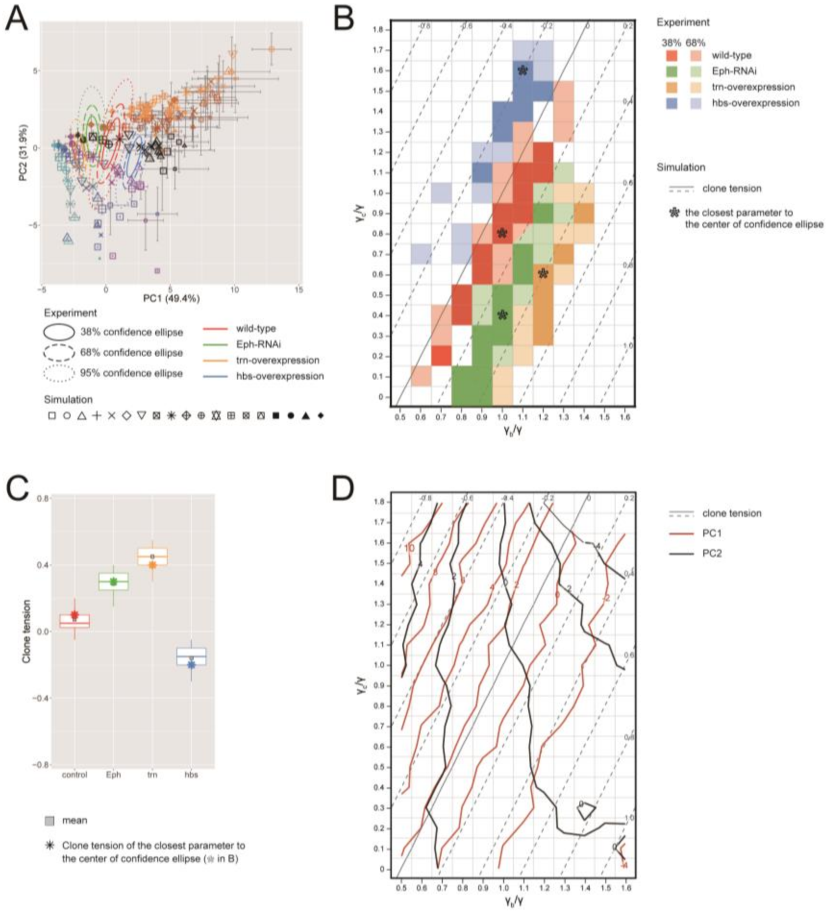

Fig. 3.5. Inference of tension parameter and clone tension of four genotypes.

(A) Projection of simulated clones onto the PC space of Drosophila experiments (See Section “Projection of the Simulation Data onto the PCA Space of the Experimental Data” for Projection; Symbols denote parameter values given in Fig. 3.4B). A limited set of simulation points are plotted for visibility (see Supplementary Fig. S3.12 for the projection of the entire simulated dataset). The experimental confidence ellipses were identical to those in Fig. 3.3H. The averaged PC scores were plotted with symbol size proportional to the number of cells within a clone and error bar representing standard deviation. **(B)** Estimated mechanical parameters of four genotypes. Mechanical parameters within the 38 and 68% confidence ellipses in (A) are shown by dark and light colors, respectively. Pentagon asterisks (*) mark the best representative parameters, which are the closest to the center of each confidence ellipse. **(C)** Estimated clone tension of four genotypes calculated by the estimated mechanical parameters within the 68% confidence ellipse [dark and light colors in (B)]. The upper/lower hinge and thick middle line represent the 25th/75th and 50th percentiles, respectively. Gray squares show the averaged clone tension. Octagonal asterisks are the clone tension of the best representative parameters [pentagonal asterisks in (B)]. **(D)** Projection of the contour lines of PC1 and PC2 scores onto the parameter space of vertex model simulations.

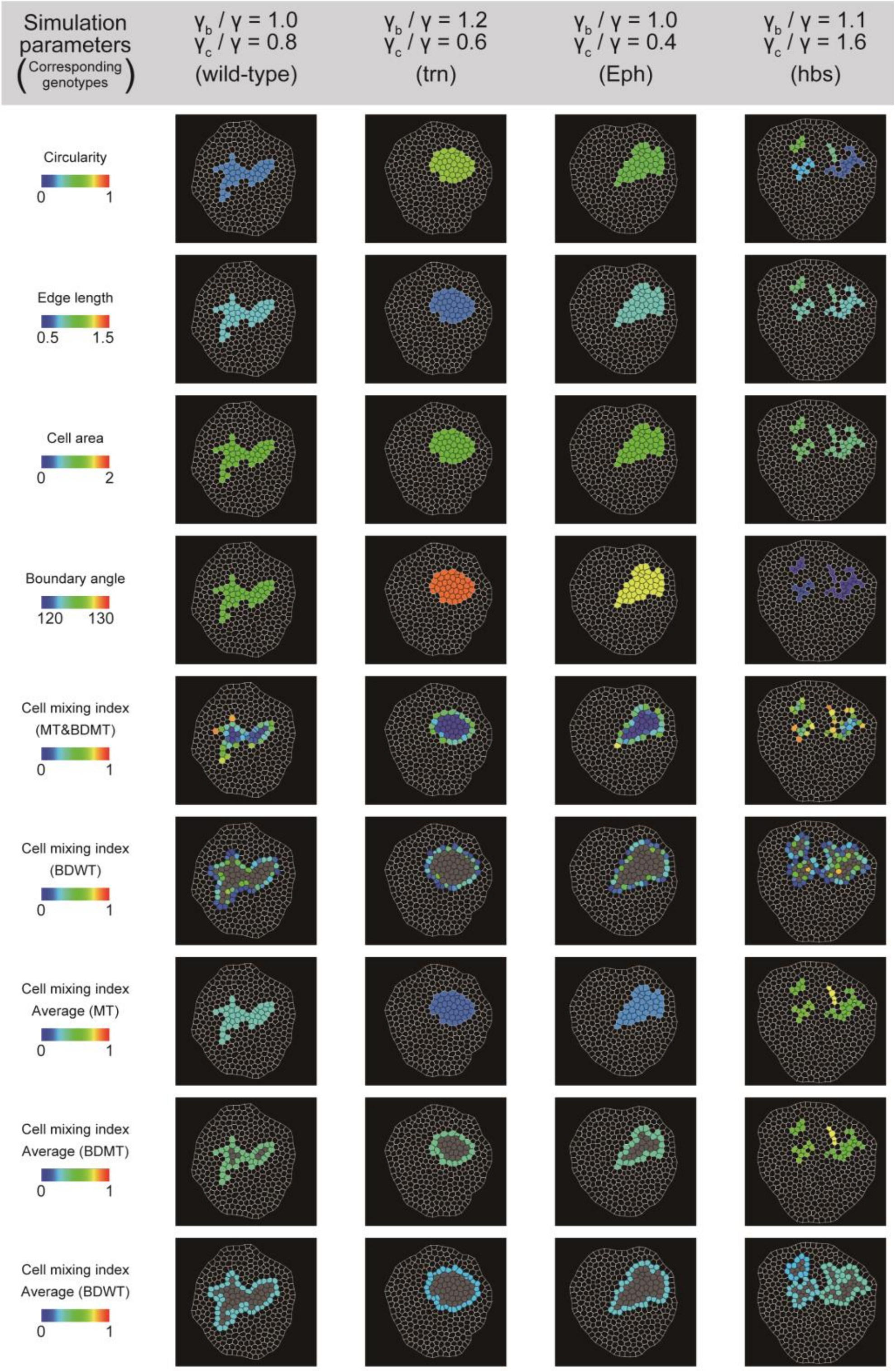

Fig. 3.6. Simulation clones corresponding to the experimental clones.

Visualization of individual criteria for the four simulated clones, which correspond to the best representative combination of line tension parameters for the four genotypes (pentagon asterisks in Fig. 3.5B)

3.7. Supporting figures

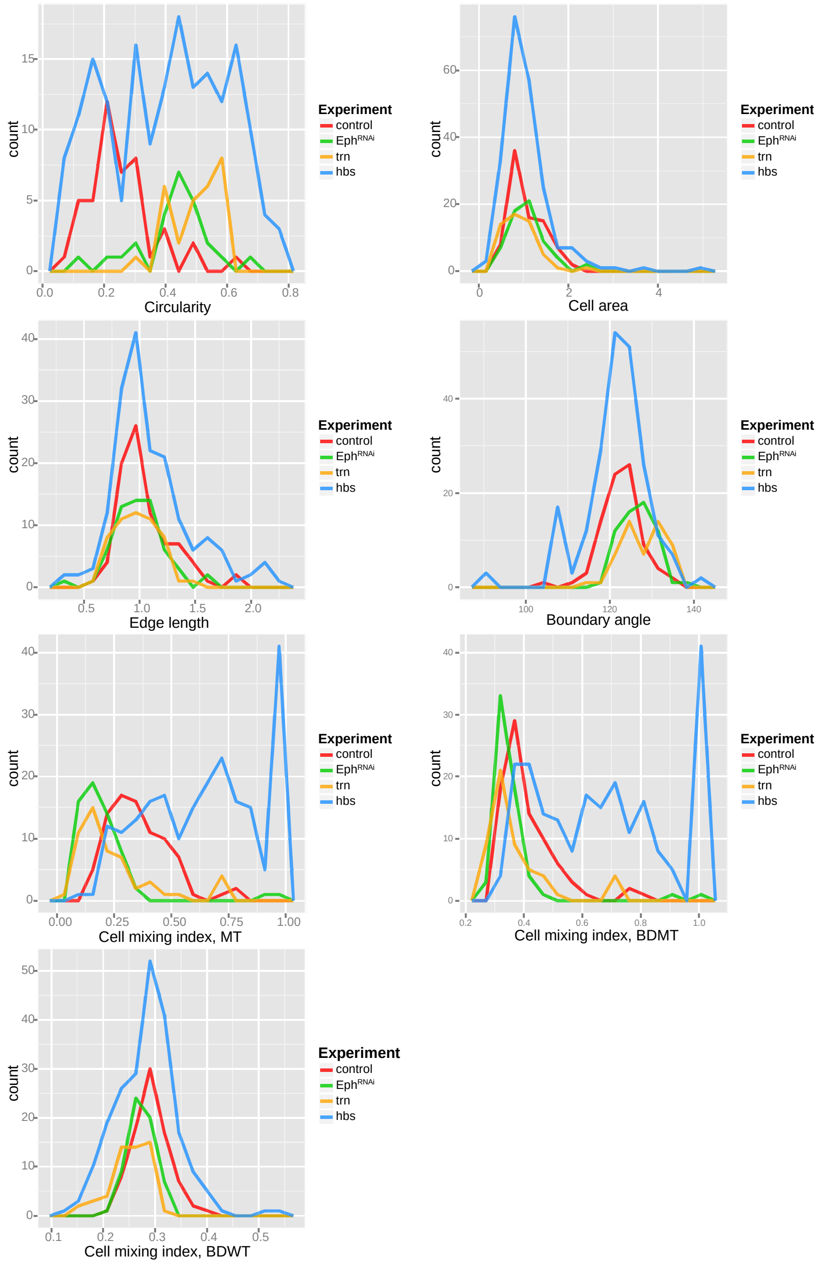

Fig. S3.1.

Histograms of individual criteria for the examined clones of the four genotypes shown in Fig. 3.3A–G. The values for each criterion was calculated by me and plotted by D. Umetsu.

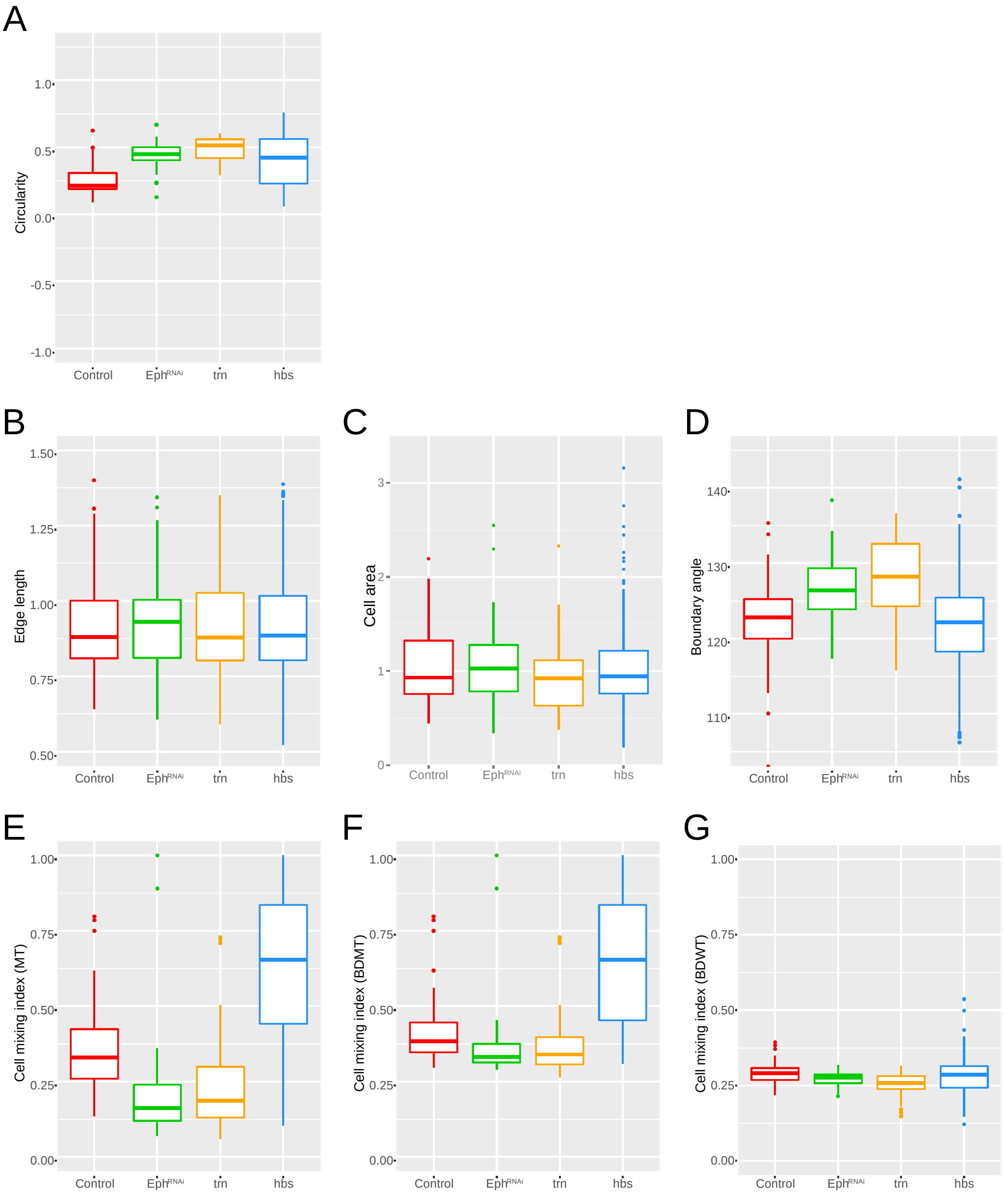

Fig. S3.2.

(A-G) Box plots of circularity (A), edge length (B), cell area (C), boundary angle (D), and cell mixing index of MT cells (E), BDMT cells (F), and BDWT cells (G) for the examined clones of four genotypes: control (red), Eph RNAi (green), trn overexpression (yellow), and hbs overexpression (blue). Plotted data were obtained from individual clones without averaging within a disc (see Fig. 3.3 for "with averaging"). I used only closed clones for circularity and both open and closed clones for the other criteria. The upper/lower hinge and thick middle line represent the 25th/75th and 50th percentiles, respectively, whereas colored dots denote outliers. I note that a few outliers with extremely high values of cell mixing index (MT, BDMT) in Eph denote clones containing only one or two cells inside of them. The criteria values was calculated by me and plotted by D. Umetsu.

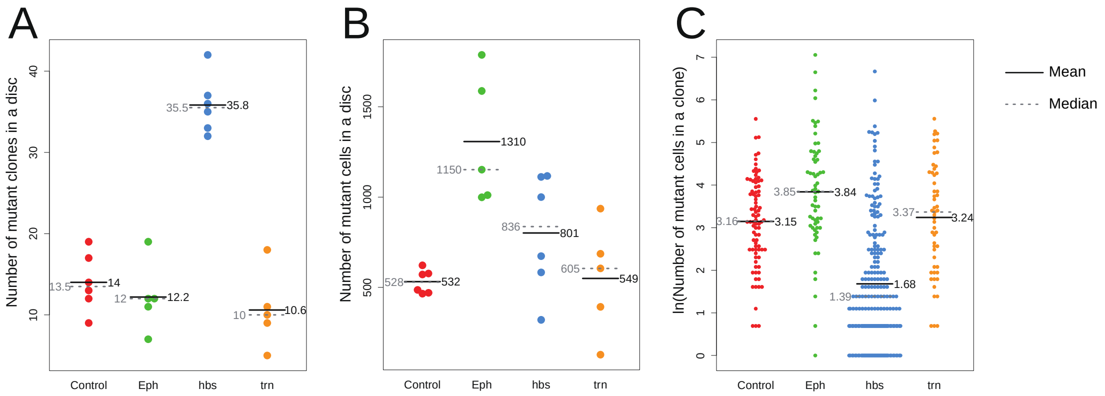

Fig. S3.3.

Each dot represents the number of clones (A) or cells (B) within a disc or the number of cells within a clone (C). Black solid lines and grey broken lines represent the average and median values, respectively.

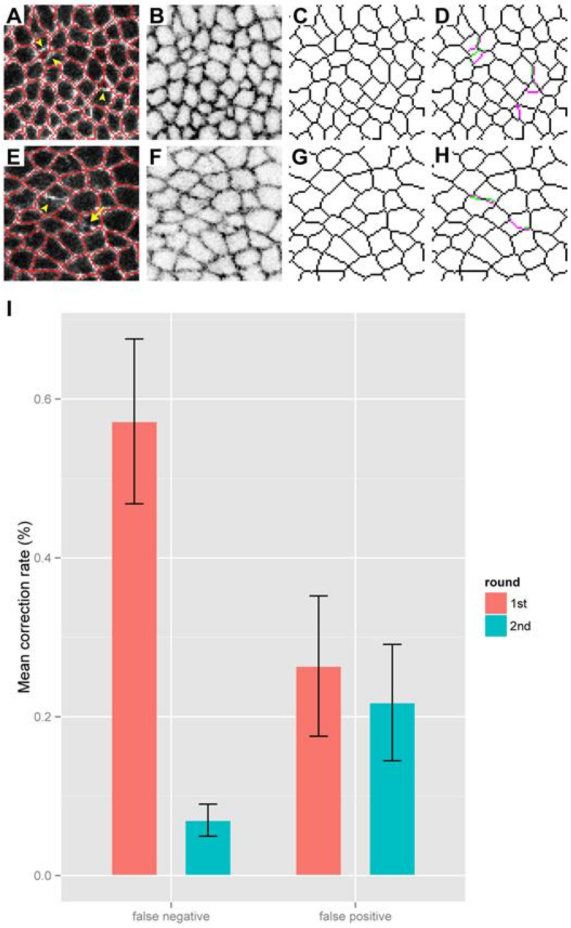

Fig. S3.4.

Estimation of segmentation error (Provided by D. Umetsu). **(A) and (E)** Overlay of a segmentation mask on its original image after auto-segmentation. Two magnified regions of an image sample from the Eph RNAi experiment. **(B)** Only the original image in (A) is shown. **(C)** Only the segmentation mask in (A) is shown. **(D)** Overlay of a hand-corrected segmentation mask on the auto-segmentation mask. Removed bonds from the auto-segmentation mask are shown in green and newly added bonds are shown in magenta. **(F)** Only the original image in (E) is shown. **(G)** Only the segmentation mask in (E) is shown. **(H)** Overlay of hand-corrected masks by different individuals. Note that while one bond was corrected in both masks (magenta and green bonds are aligned side by side) the other one exhibited discrepancy. Only one person considered it as a bond (magenta bond). Arrowheads point unrecognized cell bonds (false negative) and an arrow indicates a divisive cell bond. **(I)** Mean correction rate made by 5 individuals. Hand-corrections were performed 2 rounds by different persons for each round. The mean rate of hand-correction made by 1st and 2nd round in total was 1.12 % of all cell junctions (The sum of mean false negative and positive in 1st and 2nd round of hand-correction). Mean final discrepancy rate between 2 individuals was 0.23 % (max. 0.44 %).

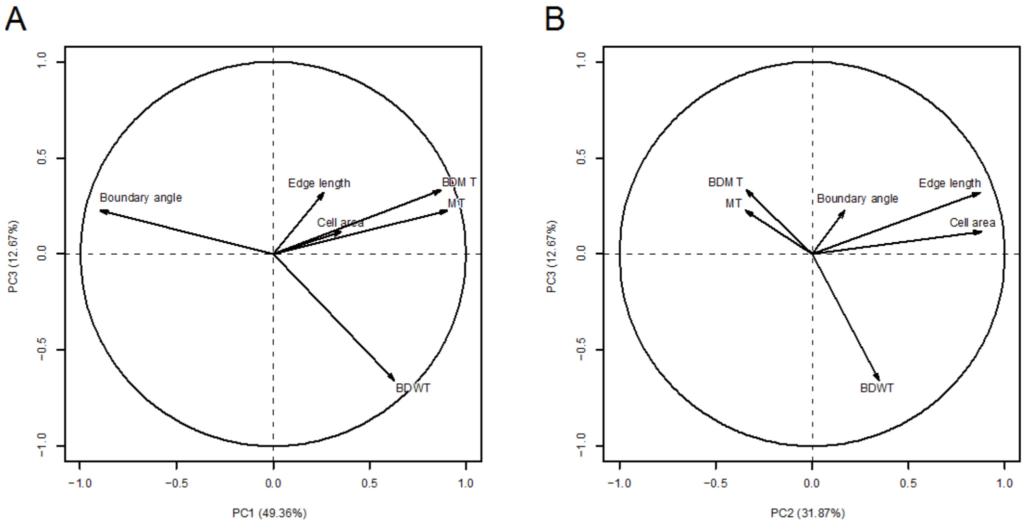

Fig. S3.5.

(A–B) Factor loadings of each criterion on PC1, PC2, and PC3 corresponding to the PCA with averaging within discs shown in Fig. 3.3H-J.

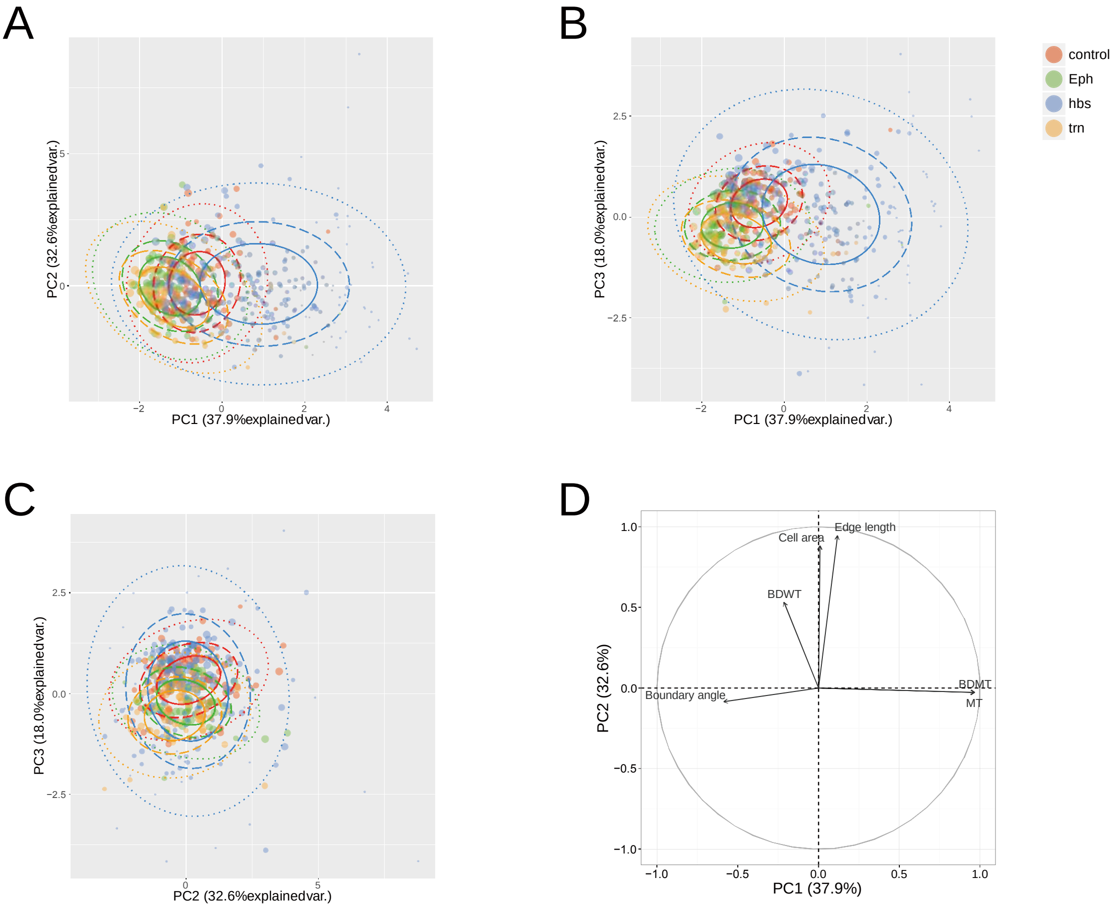

Fig. S3.6.

(A–C) PCA using the same six criteria shown in Fig. 3.3H–J without averaging of individual clones within each wing disc. **(D)** The quantified contribution (factor loading) of each criterion on PC1 and PC2 in (A) was similar to that in Fig. 3.3K.

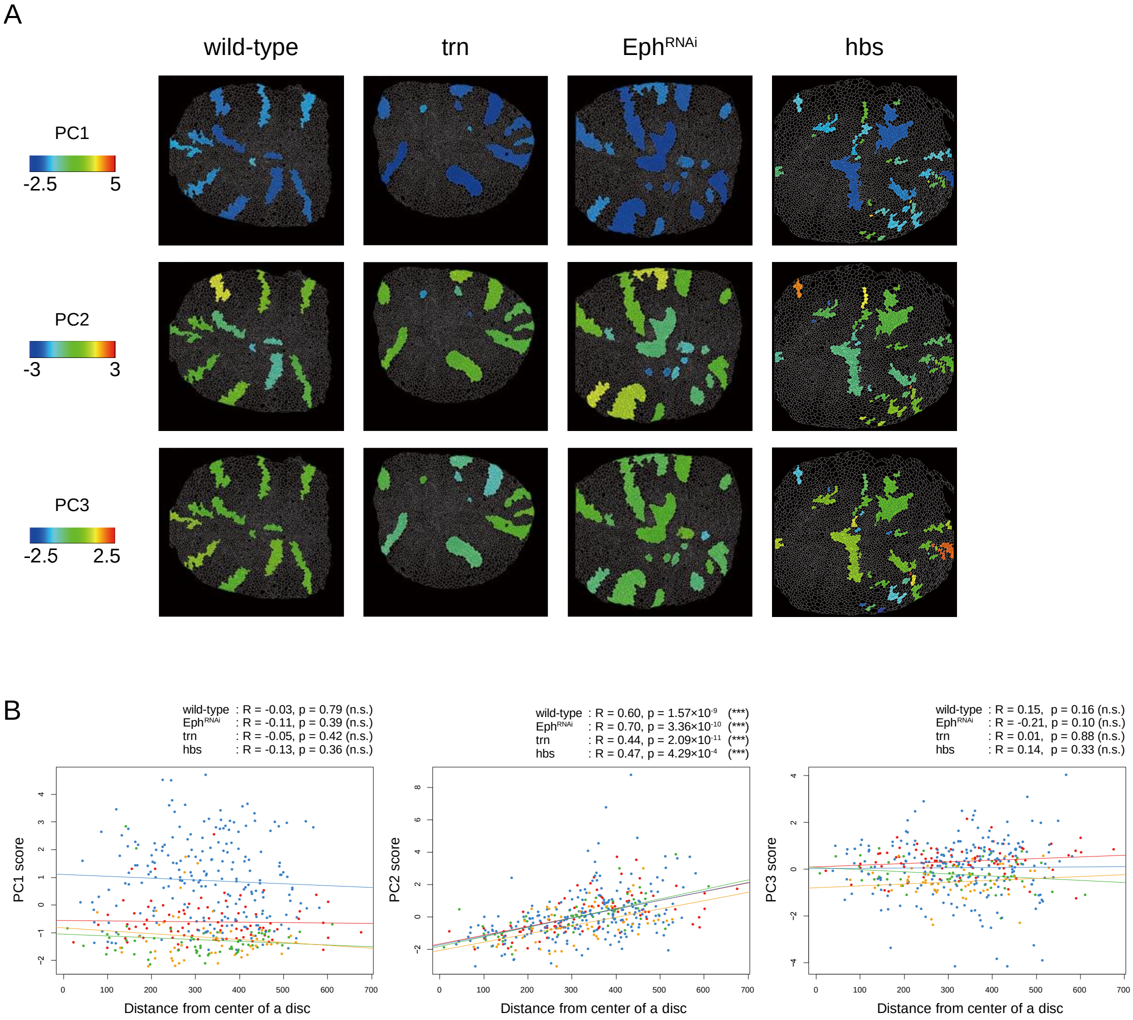

Fig. S3.7.

(A) Visualization of the scores of PC1, PC2, and PC3 for the examined clones of the four genotypes shown in Fig. S3.6A–C. **(B)** The PC2 score has a positive correlation with the distance from the center of the disc (middle panel), while the PC1 and PC3 scores do not (left and right panels). The center position was determined manually by referring to the position of the highest E-cad intensity. Pearson correlation coefficient R and test for the association between paired samples were calculated using the R environment with the "cor" and "cor.test" functions.

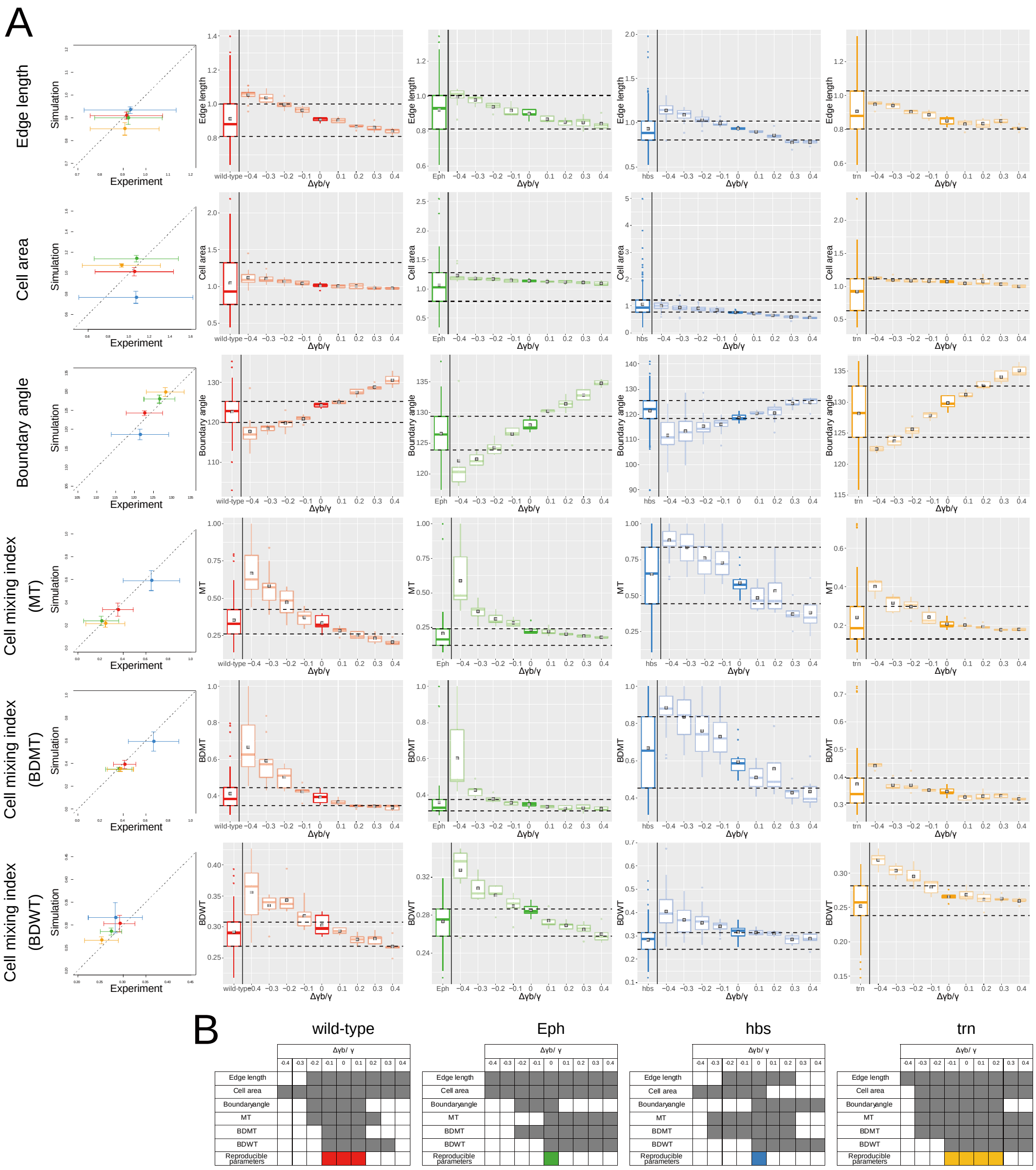

Fig. S3.8.

Evaluating precision of estimated line tension parameter γ_b. **(A)** Left most panels: Validation of the best representative parameters (γ_b and γ_c indicated by pentagon asterisks in Fig. 3.5B) in simulation by comparing clone shape criteria with those in experiment. Wild-type (red), Eph-RNAi (green), hbs-overexpression (blue), trn-overexpression (yellow). Error bars of experiment were SD (standard deviations) of all clones which were identical datasets plotted in Fig. S3.2, whereas that of simulation were SD of all clones at the estimated parameters (asterisks in Fig. 3.5B). Distance between the plots and y = x (dashed line) were less than SDs, indicating experiment was reproduced by the estimated parameters. Right panels (box plots) evaluated the parameter precision of γ_b for each genotype (horizontal direction) regarding six clone shape criteria (vertical direction). Box plot of each genotype was shown at the left most side for each panel indexed by “wild-type”, “Eph”, “hbs” and “trn”, whose datasets were identical with left most panels. Black dashed lines denote 25th and 75th percentiles of the experimental plots. Box plots at the right side of black solid line show simulated clones as a function of parameter shift $\Delta\gamma_b/\gamma$ from the best representative parameter ($\Delta\gamma_b/\gamma = 0$). **(B)** Grey filled region denotes box plots in simulation overlapped with that of experiment bounded between black dashed lines in A. Colored region at the lowest row indexed by “reproducible parameters” summarizes the parameter shift which reproduced experiments in all criteria. The maxima of absolute value of the reproducible parameters (colored $\Delta\gamma_b/\gamma$) [±0.1 (wild-type), under ±0.1 (Eph, hbs), and ±0.2 (trn)] were defined as the estimation precision of γ_b/γ. The estimated precision of γ_b/γ are equal to that of clone tension regarding γ_b, based on Equation 2 in Main text.

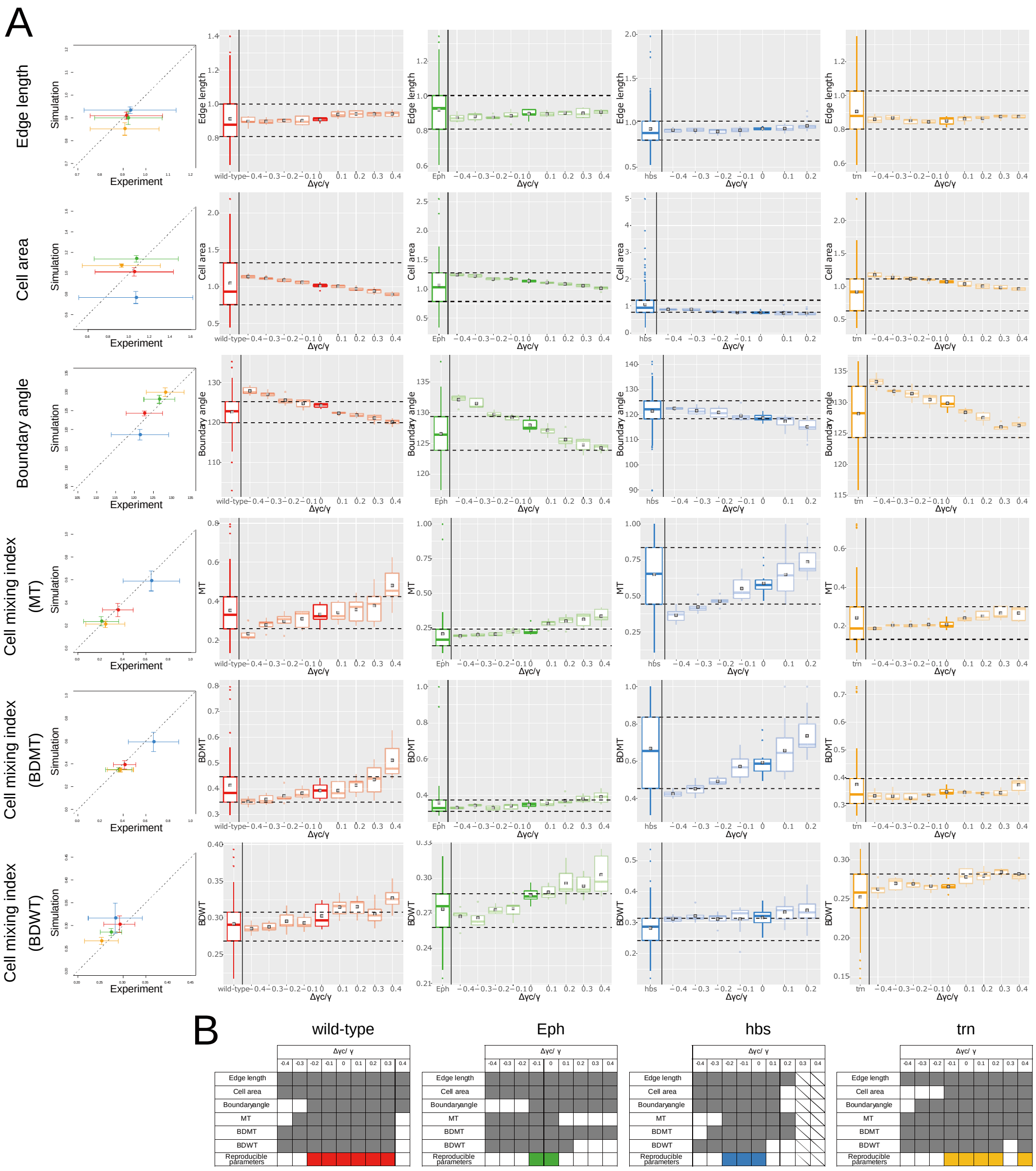

Fig. S3.9.

Evaluating precision of estimated line tension parameter γ_c. **(A-B)** The definition and layout of plots were the same with Supplementary Fig. 3.8, except for evaluating the parameter precision of γ_c in right panels. I note that simulation parameter shifting +0.3 and +0.4 ($\Delta\gamma_c/\gamma = 0.3, 0.4$) for hbs was absent, because the parameters were out of range. Following the evaluation of estimation precision of γ_b in Fig. S3.8, precision estimation of γ_c was evaluated as ±0.1 (Eph), ±0.2 (hbs, trn), and ±0.3 (wild-type), while $\Delta\gamma_c/\gamma = 0.4$ in trn was unlikely because simulation with $\Delta\gamma_c/\gamma = 0.3$ already failed to reproduce experiment. These values are twice of the estimation precision of clone tension regarding γ_c, calculated from Equation 2 in Main text. The estimation precision of clone tension was totally given by larger value between that regarding γ_b (Fig. S3.8) and γ_c; ±0.15 (wild-type), under ±0.1 (Eph), ±0.1 (hbs), ±0.2 (trn).

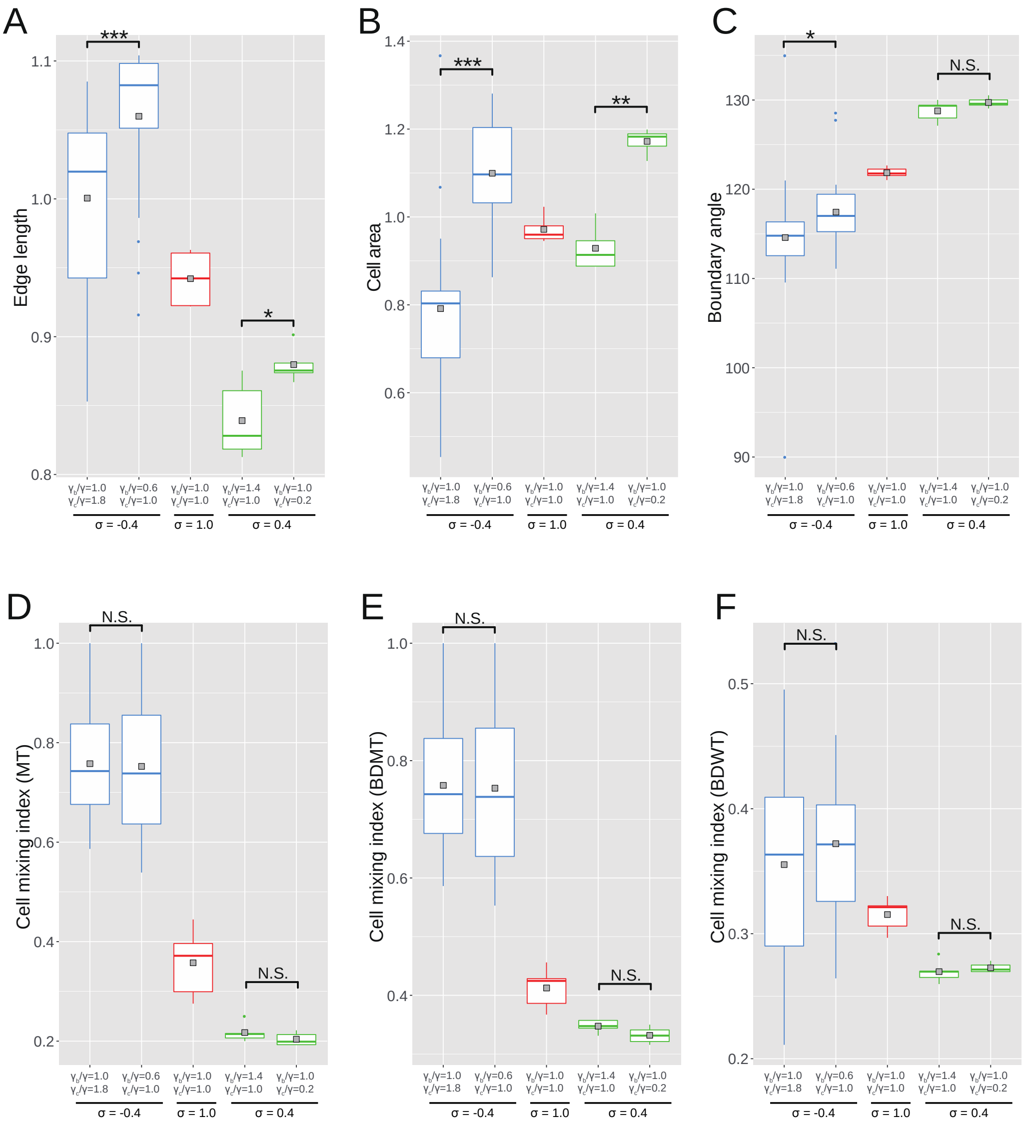

Fig. S3.10.

Role of mechanical parameters γ_b and γ_c on clone shape under constant clone tension σ in simulations (σ = -0.4 and 0.4; see Fig. 3.4C for corresponding clone shape). Box plot of (A) Edge length, (B) cell area, (C) boundary angle, (D) MT, (E) BDMT and (F) BDWT (see Fig. 3.1D-J for definition) for all clones at 40 cells in clones in total. Edge length and cell area were significantly smaller as γ_b and γ_c got larger at constant σ (σ = -0.4 and 0.4; A-B) while the other indicators showed mostly not significant difference (C-F). The physical reason of this difference is that larger line tension parameter γ_c contributes to shorten edge length so as to decrease cell area inside of the clone bulk. In addition, larger line tension parameter γ_b contributes to shorten edge length at the clone boundary. Wilcoxon rank sum test. n = 5 independent simulations for each parameter. $P < 0.001$ (***), $P < 0.01$ (**), $P < 0.05$ (*) and $P > 0.05$ (N.S., Not Significant).

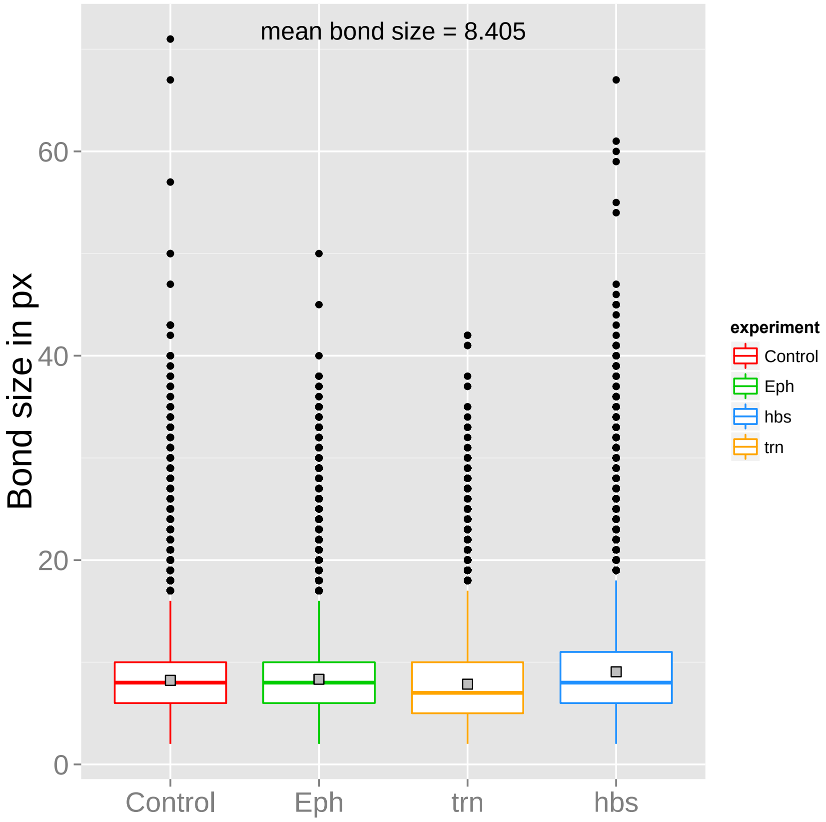

Fig. S3.11.

The mean bond size in pixel for each experiment (Provided by D. Umetsu). The mean bond size was calculated for all bonds including inside and outside of clones in all experiments. The data was plotted for each genotype separately. The mean bond size for all cell bonds of all experiments was 8.4 pixels/bond.

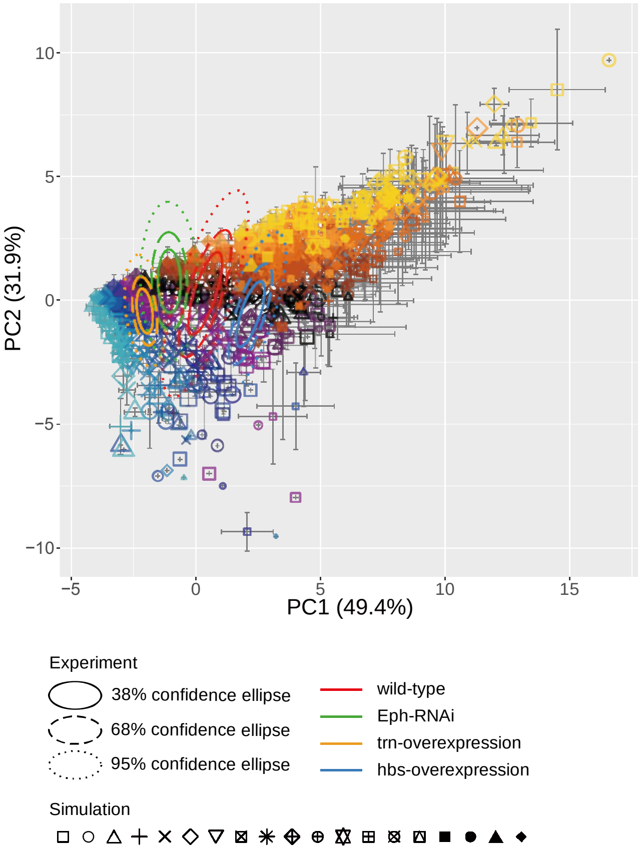

Fig S3.2.

Projection of all simulated clones onto the PC space of Drosophila experiments, which is a complete version of Fig. 3.5A.

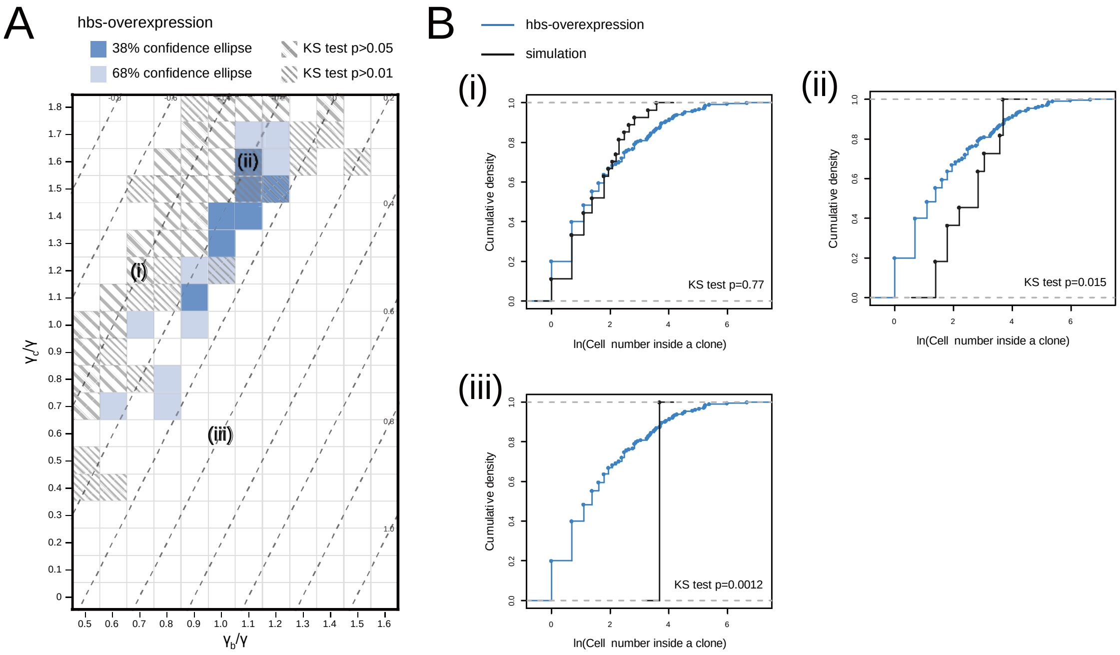

Fig. S3.13.

(A) The parameter region of hbs was limited to a more narrow range by combining it with another observation criterion, the distribution of cell number within a clone (B). In the regions containing grey oblique lines, the empirical cumulative distribution of the cell number within clones was similar to that of hbs-overexpression clones (KS test, $P > 0.05$ or $P > 0.01$). The blue-colored regions showing the estimated mechanical parameters of hbs-overexpression clones generated by projection onto the PC space were the same as those in Fig. 3.5B. The ranges of the grey-oblique and both blue-colored regions were partially overlapped each other. **(B)** The empirical cumulative distribution of cell number within clones was compared between hbs-overexpression clones and simulated clones [(i) $\gamma_b/\gamma = 0.7$, $\gamma_c/\gamma = 1.2$, (ii) $\gamma_b/\gamma = 1.1$, $\gamma_c/\gamma = 1.6$, (iii) $\gamma_b/\gamma = 1.0$, $\gamma_c/\gamma = 0.6$].

	Edge length	Cell area	Boundary angle	MT	BDMT	BDWT
Weight (PC1)	0.153	0.205	-0.519	0.525	0.505	0.366
Weight (PC2)	0.630	0.635	0.122	-0.248	-0.247	0.251
Weight (PC3)	0.367	0.134	0.259	0.258	0.380	-0.754

Table 3.1.

Weights for each criteria to calculate PC scores in Fig. 3.3H-K, which correspond to a11, a12, …, a16 in Section “Projection of the Simulation Data onto the PCA Space of the Experimental Data” in Main Text.

4. General conclusion

A wide variety of living organisms in the earth interact with each other and form a society (ecological system). Such situation in which different kinds of organisms coexist leads to cooperative and/or competitive interactions between each animal. For example, when different organisms exist in the same territory, they share or outcompete weaker animals by comparing their relative fitness. Recently, it has been gradually apparent that cells in a multicellular society also compete for their territory through a phenomenon called cell competition. In chapter 2, I analyzed spatio-temporal evolution of cell turnover during cell competition between normal host-tissue cells and oncogenic cells. The main discovery is that oncogenic mutant cells compensate for the space of normal cells' apoptosis by rapid cell expansion through re-connection of local cellular connectivity. This finding links the cell-level topological dynamics and tissue-scale mutant expansion, and may help to understand the pathological development initiated from an oncogenic mutation. In chapter 3, I analyzed how tissue occupancy of mutant clones is regulated by cell mechanical properties. I developed non-invasive methods for inferring cell mechanics and showed the mechanical basis contributed to distinct tissue occupancy under different genetic mutation. In summary, these two studies bridges gaps between cell-level behavior and tissue-level dynamics by using theoretical model, which can evaluate how individual cellular parameters influence cell population dynamics, respectively. Additionally, the validity of model predictions is verified by genetic experiment in *Drosophila* and quantitative image analysis. Such combinatorial way of research enables us to capture the phenomenon from a wide view, and would potentially create a research paradigm to understand complicated phenomena due to combination of variety of factors.

5. References

Aegerter-Wilmsen, Tinri et al. 2010. “Exploring the Effects of Mechanical Feedback on Epithelial Topology.” *Development (Cambridge, England)* 137(3):499–506.

Affolter, Markus and Konrad Basler. 2007. “The Decapentaplegic Morphogen Gradient: From Pattern Formation to Growth Regulation.” *Nature Reviews Genetics* 8(9):663–74.

Aigouy, Benoît et al. 2010. “Cell Flow Reorients the Axis of Planar Polarity in the Wing Epithelium of Drosophila.” *Cell* 142(5):773–86.

Aigouy, Benoit, Daiki Umetsu, and Suzanne Eaton. 2016. “Segmentation and Quantitative Analysis of Epithelial Tissues.” Pp. 227–39 in *Methods in molecular biology*.

Aliee, Maryam et al. 2012. “Physical Mechanisms Shaping the Drosophila Dorsoventral Compartment Boundary.” *Current Biology* 22(11):967–76.

Amoyel, Marc and Erika a Bach. 2014. “Cell Competition: How to Eliminate Your Neighbours.” *Development* 141(5):988–1000.

Aragona, Mariaceleste et al. 2013. “A Mechanical Checkpoint Controls Multicellular Growth through YAP/TAZ Regulation by Actin-Processing Factors.” *Cell* 154(5):1047–59.

Arbouzova, N. I. 2006. “JAK/STAT Signalling in Drosophila: Insights into Conserved Regulatory and Cellular Functions.” *Development* 133(14):2605–16.

Bao, Sujin, Karl-Friedrich Fischbach, Victoria Corbin, and Ross L. Cagan. 2010. “Preferential Adhesion Maintains Separation of Ommatidia in the Drosophila Eye.” *Developmental Biology* 344(2):948–56.

Bardet, Pierre-Luc et al. 2013. “PTEN Controls Junction Lengthening and Stability during Cell Rearrangement in Epithelial Tissue.” *Developmental Cell* 25(5):534–46.

Bielmeier, Christina et al. 2016. “Interface Contractility between Differently Fated Cells Drives Cell Elimination and Cyst Formation.” *Current Biology* 26(5):563–74.

Bilder, David. 2001. “PDZ Proteins and Polarity: Functions from the Fly.” *Trends in Genetics* 17(9):511–19.

Bilder, David. 2004. “Epithelial Polarity and Proliferation Control: Links from the Drosophila Neoplastic Tumor Suppressors.” *Genes & Development* 18(16):1909–25.

Böhni, Ruth et al. 1999. “Autonomous Control of Cell and Organ Size by CHICO, a Drosophila Homolog of Vertebrate IRS1–4.” *Cell* 97(7):865–75.

Bosveld, Floris et al. 2012. “Mechanical Control of Morphogenesis by Fat/Dachsous/Four-Jointed Planar Cell Polarity Pathway.” *Science* 336(6082):724–27.

Bosveld, Floris, Olga Markova, et al. 2016. “Epithelial Tricellular Junctions Act as Interphase Cell Shape Sensors to Orient Mitosis.” *Nature* 530(7591):495–98.

Bosveld, Floris, Boris Guirao, et al. 2016. “Modulation of Junction Tension by Tumor Suppressors and

Proto-Oncogenes Regulates Cell-Cell Contacts.” *Development* 143(4):623–34.

Bove, Anna et al. 2017. “Local Cellular Neighbourhood Controls Proliferation in Cell Competition” edited by A. Mogilner. *Molecular Biology of the Cell* mbc.E17-06-0368.

Brodland, G.Wayne. 2002. “The Differential Interfacial Tension Hypothesis (DITH): A Comprehensive Theory for the Self-Rearrangement of Embryonic Cells and Tissues.” *Journal of Biomechanical Engineering* 124(2):188.

Brodland, G.Wayne et al. 2010. “Video Force Microscopy Reveals the Mechanics of Ventral Furrow Invagination in Drosophila.” *Proceedings of the National Academy of Sciences* 107(51):22111–16.

Brodland, G.Wayne et al. 2014. “CellFIT: A Cellular Force-Inference Toolkit Using Curvilinear Cell Boundaries” edited by A. J. Kabla. *PLoS ONE* 9(6):e99116.

Brumby, Anthony M. 2003. “Scribble Mutants Cooperate with Oncogenic Ras or Notch to Cause Neoplastic Overgrowth in Drosophila.” *The EMBO Journal* 22(21):5769–79.

Burke, Richard and Konrad Basler. 1996. “Dpp Receptors Are Autonomously Required for Cell Proliferation in the Entire Developing Drosophila Wing.” *Development (Cambridge, England)* 122(7):2261–69.

Chang, L. H. et al. 2011. “Differential Adhesion and Actomyosin Cable Collaborate to Drive Echinoid-Mediated Cell Sorting.” *Development* 138(17):3803–12.

Chen, C. L., M. C. Schroeder, M. Kango-Singh, C. Tao, and G. Halder. 2012. “Tumor Suppression by Cell Competition through Regulation of the Hippo Pathway.” *Proceedings of the National Academy of Sciences* 109(2):484–89.

Chiou, Kevin K., Lars Hufnagel, and Boris I. Shraiman. 2012. “Mechanical Stress Inference for Two Dimensional Cell Arrays” edited by S. Shvartsman. *PLoS Computational Biology* 8(5):e1002512.

Clavería, Cristina, Giovanna Giovinazzo, Rocío Sierra, and Miguel Torres. 2013. “Myc-Driven Endogenous Cell Competition in the Early Mammalian Embryo.” *Nature* 500(7460):39–44.

Clevers, Hans. 2006. “Wnt/β-Catenin Signaling in Development and Disease.” *Cell* 127(3):469–80.

Collinet, Claudio, Matteo Rauzi, Pierre-françois Lenne, and Thomas Lecuit. 2015. “Local and Tissue-Scale Forces Drive Oriented Junction Growth during Tissue Extension.” *Nature Cell Biology* 17(10):1247–58.

Cortina, Carme et al. 2007. “EphB–ephrin-B Interactions Suppress Colorectal Cancer Progression by Compartmentalizing Tumor Cells.” *Nature Genetics* 39(11):1376–83.

Curran, Scott et al. 2017. “Myosin II Controls Junction Fluctuations to Guide Epithelial Tissue Ordering.” *Developmental Cell* 43(4):480–492.e6.

Doggett, Karen, Felix A. Grusche, Helena E. Richardson, and Anthony M. Brumby. 2011. “Loss of the Drosophila Cell Polarity Regulator Scribbled Promotes Epithelial Tissue Overgrowth and Cooperation with Oncogenic Ras-Raf through Impaired Hippo Pathway Signaling.” *BMC Developmental Biology* 11(1):57.

Dworak, H. a, M. a Charles, L. B. Pellerano, and H. Sink. 2001. “Characterization of Drosophila Hibris, a Gene Related to Human Nephrin.” *Development (Cambridge, England)* 128(21):4265–76.

Eichenlaub, Teresa, Stephen M. Cohen, and Héctor Herranz. 2016. “Cell Competition Drives the Formation of Metastatic Tumors in a Drosophila Model of Epithelial Tumor Formation.” *Current biology : CB* 26(4):419–27.

Eisenhoffer, George T. et al. 2012. “Crowding Induces Live Cell Extrusion to Maintain Homeostatic Cell Numbers in Epithelia.” *Nature* 484(7395):546–49.

Eldar, Avigdor and Michael B. Elowitz. 2010. “Functional Roles for Noise in Genetic Circuits.” *Nature* 467(7312):167–73.

Elowitz, Michael B. 2002. “Stochastic Gene Expression in a Single Cell.” *Science* 297(5584):1183–86.

Fagotto, Francois, Rudolf Winklbauer, and Nazanin Rohani. 2014. “Ephrin-Eph Signaling in Embryonic Tissue Separation.” *Cell Adhesion & Migration* 8(4):308–26.

Farhadifar, Reza, Jens-Christian Röper, Benoit Aigouy, Suzanne Eaton, and Frank Jülicher. 2007. “The Influence of Cell Mechanics, Cell-Cell Interactions, and Proliferation on Epithelial Packing.” *Current biology : CB* 17(24):2095–2104.

Fletcher, Alexander G., James M. Osborne, Philip K. Maini, and David J. Gavaghan. 2013. “Implementing Vertex Dynamics Models of Cell Populations in Biology within a Consistent Computational Framework.” *Progress in Biophysics and Molecular Biology* 113(2):299–326.

Froldi, Francesca et al. 2010. “The Lethal Giant Larvae Tumour Suppressor Mutation Requires dMyc Oncoprotein to Promote Clonal Malignancy.” *BMC Biology* 8(1):33.

Gibson, Matthew C., Ankit B. Patel, Radhika Nagpal, and Norbert Perrimon. 2006. “The Emergence of Geometric Order in Proliferating Metazoan Epithelia.” *Nature* 442(7106):1038–41.

Gibson, Matthew C. and Norbert Perrimon. 2003. “Apicobasal Polarization: Epithelial Form and Function.” *Current Opinion in Cell Biology* 15(6):747–52.

Gibson, William T. et al. 2011. “Control of the Mitotic Cleavage Plane by Local Epithelial Topology.” *Cell* 144(3):427–38.

Gibson, William T. et al. 2014. “On the Origins of the Mitotic Shift in Proliferating Cell Layers.” *Theoretical Biology and Medical Modelling* 11(1):26.

Gibson, William T. and Matthew C. Gibson. 2009. “Chapter 4 Cell Topology, Geometry, and Morphogenesis in Proliferating Epithelia.” Pp. 87–114 in *erom*, vol. 89. Elsevier Inc.

Gillies, Taryn E. and Clemens Cabernard. 2011. “Cell Division Orientation in Animals.” *Current Biology* 21(15):R599–609.

Graner, François. 1993. “Can Surface Adhesion Drive Cell-Rearrangement? Part I: Biological Cell-Sorting.” *Journal of Theoretical Biology* 164(4):455–76.

Graner, François and James A. Glazier. 1992. “Simulation of Biological Cell Sorting Using a Two-Dimensional Extended Potts Model.” *Physical Review Letters* 69(13):2013–16.

Graner, François and Yasuji Sawada. 1993. “Can Surface Adhesion Drive Cell Rearrangement? Part II: A Geometrical Model.” *Journal of Theoretical Biology* 164(4):477–506.

Di Gregorio, Aida, Sarah Bowling, and Tristan Argeo Rodriguez. 2016. “Cell Competition and Its Role in the Regulation of Cell Fitness from Development to Cancer.” *Developmental Cell* 38(6):621–34.

Grzeschik, Nicola A., Linda M. Parsons, Melinda L. Allott, Kieran F. Harvey, and Helena E. Richardson. 2010. “Lgl, aPKC, and Crumbs Regulate the Salvador/Warts/Hippo Pathway through Two Distinct Mechanisms.” *Current Biology* 20(7):573–81.

Grzeschik, Nicola A., Linda M. Parsons, and Helena Richardson. 2010. “Lgl, the SWH Pathway and Tumorigenesis: It’s a Matter of Context and Competition!” *Cell Cycle* 9(16):3222–32.

Gudipaty, S. A. et al. 2017. “Mechanical Stretch Triggers Rapid Epithelial Cell Division through Piezo1.” *Nature* 543(7643):118–21.

Guirao, Boris and Yohanns Bellaïche. 2017. “Biomechanics of Cell Rearrangements in Drosophila.” *Current Opinion in Cell Biology* 48:113–24.

Gumbiner, Barry M. and Nam-Gyun Kim. 2014. “The Hippo-YAP Signaling Pathway and Contact Inhibition of Growth.” *Journal of Cell Science* 127(4):709–17.

Hafezi, Yassi, Justin A. Bosch, and Iswar K. Hariharan. 2012. “Differences in Levels of the Transmembrane Protein Crumbs Can Influence Cell Survival at Clonal Boundaries.” *Developmental Biology* 368(2):358–69.

Hale, Rosalind and David Strutt. 2015. “Conservation of Planar Polarity Pathway Function Across the Animal Kingdom.” *Annual Review of Genetics* 49(1):529–51.

Hamaratoglu, Fisun, Markus Affolter, and George Pyrowolakis. 2014. “Dpp/BMP Signaling in Flies: From Molecules to Biology.” *Seminars in Cell & Developmental Biology* 32:128–36.

Hara, Yusuke, Murat Shagirov, and Yusuke Toyama. 2016. “Cell Boundary Elongation by Non-Autonomous Contractility in Cell Oscillation.” *Current Biology* 26(17):2388–96.

Harvey, Kieran F., Xiaomeng Zhang, and David M. Thomas. 2013. “The Hippo Pathway and Human Cancer.” *Nature Reviews Cancer* 13(4):246–57.

Heisenberg, Carl-Philipp and Yohanns Bellaïche. 2013. “Forces in Tissue Morphogenesis and Patterning.” *Cell* 153(5):948–62.

Heller, Davide et al. 2016. “EpiTools: An Open-Source Image Analysis Toolkit for Quantifying Epithelial Growth Dynamics.” *Developmental Cell* 36(1):103–16.

Honda, Hisao. 1983. “Geometrical Models for Cells in Tissues.” *International Review of Cytology* 81:191–248.

Huang, Juan, Wenke Zhou, Wei Dong, Annie M. Watson, and Yang Hong. 2009. “Directed, Efficient, and Versatile Modifications of the Drosophila Genome by Genomic Engineering.” *Proceedings of the National Academy of Sciences* 106(20):8284–89.

Igaki, Tatsushi, Jose Carlos Pastor-Pareja, Hiroka Aonuma, Masayuki Miura, and Tian Xu. 2009.

“Intrinsic Tumor Suppression and Epithelial Maintenance by Endocytic Activation of Eiger/TNF Signaling in Drosophila.” *Developmental Cell* 16(3):458–65.

Ishihara, Shuji and Kaoru Sugimura. 2012. “Bayesian Inference of Force Dynamics during Morphogenesis.” *Journal of Theoretical Biology* 313:201–11.

Itzkovitz, Shalev et al. 2011. “Single-Molecule Transcript Counting of Stem-Cell Markers in the Mouse Intestine.” *Nature Cell Biology* 14(1):106–14.

Iwata, H. 2002. “SHAPE: A Computer Program Package for Quantitative Evaluation of Biological Shapes Based on Elliptic Fourier Descriptors.” *Journal of Heredity* 93(5):384–85.

Johnston, Laura A., David A. Prober, Bruce A. Edgar, Robert N. Eisenman, and Peter Gallant. 1999. “Drosophila Myc Regulates Cellular Growth during Development.” *Cell* 98(6):779–90.

Kajita, Mihoko et al. 2014. “Filamin Acts as a Key Regulator in Epithelial Defence against Transformed Cells.” *Nature Communications* 5:4428.

Kale, Abhijit, Gerard Rimesso, and Nicholas E. Baker. 2016. “Local Cell Death Changes the Orientation of Cell Division in the Developing Drosophila Wing Imaginal Disc Without Using Fat or Dachsous as Orienting Signals” edited by A. Singh. *PLOS ONE* 11(12):e0167637.

Karim, F. D. and G. M. Rubin. 1998. “Ectopic Expression of Activated Ras1 Induces Hyperplastic Growth and Increased Cell Death in Drosophila Imaginal Tissues.” *Development* 125(1):1–9.

Kerridge, Stephen et al. 2016. “Modular Activation of Rho1 by GPCR Signalling Imparts Polarized Myosin II Activation during Morphogenesis.” *Nature Cell Biology* 18(3):261–70.

Klingenberg, Christian Peter. 2011. “MorphoJ: An Integrated Software Package for Geometric Morphometrics.” *Molecular ecology resources* 11(2):353–57.

KORN, ROBERT W. and RICHARD M. SPALDING. 1973. “THE GEOMETRY OF PLANT EPIDERMAL CELLS.” *New Phytologist* 72(6):1357–65.

Koto, Akiko, Erina Kuranaga, and Masayuki Miura. 2009. “Temporal Regulation of Drosophila IAP1 Determines Caspase Functions in Sensory Organ Development.” *The Journal of Cell Biology* 187(2):219–31.

Krieg, Michael et al. 2008. “Tensile Forces Govern Germ-Layer Organization in Zebrafish.” *Nature Cell Biology* 10(4):429–36.

de la Cova, Claire, Mauricio Abril, Paola Bellosta, Peter Gallant, and Laura a. Johnston. 2004. “Drosophila Myc Regulates Organ Size by Inducing Cell Competition.” *Cell* 117(1):107–16.

Lacayo, Catherine I. et al. 2007. “Emergence of Large-Scale Cell Morphology and Movement from Local Actin Filament Growth Dynamics” edited by J. B. Alberts. *PLoS Biology* 5(9):e233.

Landsberg, Katharina P. et al. 2009. “Increased Cell Bond Tension Governs Cell Sorting at the Drosophila Anteroposterior Compartment Boundary.” *Current Biology* 19(22):1950–55.

Lecuit, Thomas and Pierre-François Lenne. 2007. “Cell Surface Mechanics and the Control of Cell Shape, Tissue Patterns and Morphogenesis.” *Nature Reviews Molecular Cell Biology* 8(8):633–44.

Lee, Sang-woo and Yoshihiro Morishita. 2017. “Possible Roles of Mechanical Cell Elimination Intrinsic to Growing Tissues from the Perspective of Tissue Growth Efficiency and Homeostasis” edited by P. K. Maini. *PLOS Computational Biology* 13(7):e1005651.

Lee, Tzumin and Liqun Luo. 1999. “Mosaic Analysis with a Repressible Cell Marker for Studies of Gene Function in Neuronal Morphogenesis.” *Neuron* 22(3):451–61.

Legoff, Loïc, Hervé Rouault, and Thomas Lecuit. 2013. “A Global Pattern of Mechanical Stress Polarizes Cell Divisions and Cell Shape in the Growing Drosophila Wing Disc.” *Development* 140(19):4051–59.

Levayer, Romain, Carole Dupont, and Eduardo Moreno. 2016. “Tissue Crowding Induces Caspase-Dependent Competition for Space.” *Current Biology* 26(5):670–77.

Levayer, Romain, Barbara Hauert, and Eduardo Moreno. 2015. “Cell Mixing Induced by Myc Is Required for Competitive Tissue Invasion and Destruction.” *Nature* 524(7566):476–80.

Levayer, Romain and Thomas Lecuit. 2013. “Oscillation and Polarity of E-Cadherin Asymmetries Control Actomyosin Flow Patterns during Morphogenesis.” *Developmental Cell* 26(2):162–75.

Levayer, Romain and Eduardo Moreno. 2013. “Mechanisms of Cell Competition: Themes and Variations.” *The Journal of Cell Biology* 200(6):689–98.

Levayer, Romain and Eduardo Moreno. 2016. “How to Be in a Good Shape? The Influence of Clone Morphology on Cell Competition.” *Communicative & Integrative Biology* 9(1):e1102806.

Lewis, Frederic T. 1928. “The Correlation between Cell Division and the Shapes and Sizes of Prismatic Cells in the Epidermis of Cucumis.” *The Anatomical Record* 38(3):341–76.

Li, Wei and Nicholas E. Baker. 2007. “Engulfment Is Required for Cell Competition.” *Cell* 129(6):1215–25.

Li, Wei, Abhijit Kale, and Nicholas E. Baker. 2009. “Oriented Cell Division as a Response to Cell Death and Cell Competition.” *Current Biology* 19(21):1821–26.

Li, Willis X. 2008. “Canonical and Non-Canonical JAK–STAT Signaling.” *Trends in Cell Biology* 18(11):545–51.

Lienkamp, Soeren S. et al. 2012. “Vertebrate Kidney Tubules Elongate Using a Planar Cell Polarity–dependent, Rosette-Based Mechanism of Convergent Extension.” *Nature Genetics* 44(12):1382–87.

Lye, Claire M. et al. 2015. “Mechanical Coupling between Endoderm Invagination and Axis Extension in Drosophila” edited by N. Tapon. *PLOS Biology* 13(11):e1002292.

Maitre, J. L. et al. 2012. “Adhesion Functions in Cell Sorting by Mechanically Coupling the Cortices of Adhering Cells.” *Science* 338(6104):253–56.

Maître, Jean-Léon et al. 2016. “Asymmetric Division of Contractile Domains Couples Cell Positioning and Fate Specification.” *Nature* 536(7616):344–48.

Mao, Yanlan et al. 2011. “Planar Polarization of the Atypical Myosin Dachs Orients Cell Divisions in Drosophila.” *Genes & Development* 25(2):131–36.

Mao, Yanlan et al. 2013. “Differential Proliferation Rates Generate Patterns of Mechanical Tension That Orient Tissue Growth.” *The EMBO Journal* 32(21):2790–2803.

Marinari, Eliana et al. 2012. “Live-Cell Delamination Counterbalances Epithelial Growth to Limit Tissue Overcrowding.” *Nature* 484(7395):542–45.

Martin, F. A., Salvador C. Herrera, and Ginés Morata. 2009. “Cell Competition, Growth and Size Control in the Drosophila Wing Imaginal Disc.” *Development* 136(22):3747–56.

Marygold, Steven J. et al. 2007. “The Ribosomal Protein Genes and Minute Loci of Drosophila Melanogaster.” *Genome Biology* 8(10):R216.

Menéndez, Javier, Ainhoa Pérez-Garijo, Manuel Calleja, and Ginés Morata. 2010. “A Tumor-Suppressing Mechanism in Drosophila Involving Cell Competition and the Hippo Pathway.” *Proceedings of the National Academy of Sciences of the United States of America* 107(33):14651–56.

Meyer, Heather M. and Adrienne H. K. Roeder. 2014. “Stochasticity in Plant Cellular Growth and Patterning.” *Frontiers in Plant Science* 5(September):420.

Meyer, S. N. et al. 2014. “An Ancient Defense System Eliminates Unfit Cells from Developing Tissues during Cell Competition.” *Science* 346(6214):1258236.

Milán, M., U. Weihe, S. Tiong, W. Bender, and S. M. Cohen. 2001. “Msh Specifies Dorsal Cell Fate in the Drosophila Wing.” *Development* 128(17):3263–68.

Milán, Marco, Lidia Pérez, and Stephen M. Cohen. 2002. “Short-Range Cell Interactions and Cell Survival in the Drosophila Wing.” *Developmental cell* 2(6):797–805.

Molina, Julian R. and Alex A. Adjei. 2006. “The Ras/Raf/MAPK Pathway.” *Journal of Thoracic Oncology* 1(1):7–9.

Monier, Bruno, Anne Pélissier-Monier, Andrea H. Brand, and Bénédicte Sanson. 2010. “An Actomyosin-Based Barrier Inhibits Cell Mixing at Compartmental Boundaries in Drosophila Embryos.” *Nature Cell Biology* 12(1):60–65.

Morata, Ginés and Luna Ballesteros-Arias. 2015. “Cell Competition, Apoptosis and Tumour Development.” *The International Journal of Developmental Biology* 59(1-2–3):79–86.

Morata, Ginés and Pedro Ripoll. 1975. “Minutes: Mutants of Drosophila Autonomously Affecting Cell Division Rate.” *Developmental Biology* 42(2):211–21.

Moreno, Eduardo and Konrad Basler. 2004. “dMyc Transforms Cells into Super-Competitors.” *Cell* 117(1):117–29.

Moreno, Eduardo, Konrad Basler, and Ginés Morata. 2002. “Cells Compete for Decapentaplegic Survival Factor to Prevent Apoptosis in Drosophila Wing Development.” *Nature* 416(6882):755–59.

Mumcu, Peer. 2011. “Self-Organized Growth in Developing Epithelia.”

Nagpal, Radhika, Ankit Patel, and Matthew C. Gibson. 2008. “Epithelial Topology.” *BioEssays* 30(3):260–66.

Nellen, Denise, Richard Burke, Gary Struhl, and Konrad Basler. 1996. “Direct and Long-Range Action of a DPP Morphogen Gradient.” *Cell* 85(3):357–68.

Neto-Silva, Ricardo M., Simon de Beco, and Laura a. Johnston. 2010. “Evidence for a Growth-Stabilizing Regulatory Feedback Mechanism between Myc and Yorkie, the Drosophila Homolog of Yap.” *Developmental Cell* 19(4):507–20.

Nier, Vincent et al. 2016. “Inference of Internal Stress in a Cell Monolayer.” *Biophysical Journal* 110(7):1625–35.

Nishimura, T. and M. Takeichi. 2008. “Shroom3-Mediated Recruitment of Rho Kinases to the Apical Cell Junctions Regulates Epithelial and Neuroepithelial Planar Remodeling.” *Development* 135(8):1493–1502.

Nishimura, Tamako, Hisao Honda, and Masatoshi Takeichi. 2012. “Planar Cell Polarity Links Axes of Spatial Dynamics in Neural-Tube Closure.” *Cell* 149(5):1084–97.

Norman, M. et al. 2012. “Loss of Scribble Causes Cell Competition in Mammalian Cells.” *Journal of Cell Science* 125(1):59–66.

Nose, Akinao, Akira Nagafuchi, and Masatoshi Takeichi. 1988. “Expressed Recombinant Cadherins Mediate Cell Sorting in Model Systems.” *Cell* 54(7):993–1001.

Oh, H. and K. D. Irvine. 2009. “In Vivo Analysis of Yorkie Phosphorylation Sites.” *Oncogene* 28(17):1916–27.

Ohsawa, Shizue et al. 2011. “Elimination of Oncogenic Neighbors by JNK-Mediated Engulfment in Drosophila.” *Developmental Cell* 20(3):315–28.

Oliver, Edward R. 2004. “Ribosomal Protein L24 Defect in Belly Spot and Tail (Bst), a Mouse Minute.” *Development* 131(16):3907–20.

Pan, Yuanwang, Idse Heemskerk, Consuelo Ibar, Boris I. Shraiman, and Kenneth D. Irvine. 2016. “Differential Growth Triggers Mechanical Feedback That Elevates Hippo Signaling.” *Proceedings of the National Academy of Sciences* 113(45):E6974–83.

Paré, Adam C. et al. 2014. “A Positional Toll Receptor Code Directs Convergent Extension in Drosophila.” *Nature* 515(7528):523–27.

Paulsson, Johan. 2004. “Summing up the Noise in Gene Networks.” *Nature* 427(6973):415–18.

Pelengaris, Stella, Mike Khan, and Gerard Evan. 2002. “C-MYC: More than Just a Matter of Life and Death.” *Nature Reviews Cancer* 2(10):764–76.

Pellettieri, Jason and Alejandro Sánchez Alvarado. 2007. “Cell Turnover and Adult Tissue Homeostasis: From Humans to Planarians.” *Annual Review of Genetics* 41(1):83–105.

di Pietro, Florencia, Arnaud Echard, and Xavier Morin. 2016. “Regulation of Mitotic Spindle Orientation: An Integrated View.” *EMBO reports* 17(8):1106–30.

Pincus, Z. and J. A. Theriot. 2007. “Comparison of Quantitative Methods for Cell-Shape Analysis.” *Journal of microscopy* 227(Pt 2):140–56.

Porazinski, Sean et al. 2016. “EphA2 Drives the Segregation of Ras-Transformed Epithelial Cells from

Normal Neighbors." *Current Biology* 26(23):3220–29.

Portela, Marta et al. 2010. "Drosophila SPARC Is a Self-Protective Signal Expressed by Loser Cells during Cell Competition." *Developmental Cell* 19(4):562–73.

Prober, David A. and Bruce A. Edgar. 2000. "Ras1 Promotes Cellular Growth in the Drosophila Wing." *Cell* 100(4):435–46.

R Development Core Team. 2015. "R: A Language and Environment for Statistical Computing. R Foundation for Statistical Computing, Vienna, Austria. URL http://www.R-Project.org/." *R Foundation for Statistical Computing, Vienna, Austria.* 2015.

Raff, Martin C. 1992. "Social Controls on Cell Survival and Cell Death." *Nature* 356(6368):397–400.

Raj, Arjun and Alexander van Oudenaarden. 2008. "Nature, Nurture, or Chance: Stochastic Gene Expression and Its Consequences." *Cell* 135(2):216–26.

Raser, Jonathan M. 2004. "Control of Stochasticity in Eukaryotic Gene Expression." *Science* 304(5678):1811–14.

Rauzi, Matteo, Pierre-François Lenne, and Thomas Lecuit. 2010. "Planar Polarized Actomyosin Contractile Flows Control Epithelial Junction Remodelling." *Nature* 468(7327):1110–14.

Rhiner, Christa et al. 2010. "Flower Forms an Extracellular Code That Reveals the Fitness of a Cell to Its Neighbors in Drosophila." *Developmental Cell* 18(6):985–98.

Rhiner, Christa and Eduardo Moreno. 2009. "Super Competition as a Possible Mechanism to Pioneer Precancerous Fields." *Carcinogenesis* 30(5):723–28.

Rodrigues, a. B. et al. 2012. "Activated STAT Regulates Growth and Induces Competitive Interactions Independently of Myc, Yorkie, Wingless and Ribosome Biogenesis." *Development* 139(21):4051–61.

Rudolf, Katrin et al. 2015. "A Local Difference in Hedgehog Signal Transduction Increases Mechanical Cell Bond Tension and Biases Cell Intercalations along the Drosophila Anteroposterior Compartment Boundary." *Development* 142(22):3845–58.

Sakurai, Kayoko T., Tetsuya Kojima, Toshiro Aigaki, and Shigeo Hayashi. 2007. "Differential Control of Cell Affinity Required for Progression and Refinement of Cell Boundary during Drosophila Leg Segmentation." *Developmental Biology* 309(1):126–36.

Sancho, Margarida et al. 2013. "Competitive Interactions Eliminate Unfit Embryonic Stem Cells at the Onset of Differentiation." *Developmental Cell* 26(1):19–30.

Sawyer, J. K. et al. 2011. "A Contractile Actomyosin Network Linked to Adherens Junctions by Canoe/afadin Helps Drive Convergent Extension." *Molecular Biology of the Cell* 22(14):2491–2508.

Schonbaum, Christopher P., Edward L. Organ, Shimian Qu, and Douglas R. Cavener. 1992. "The Drosophila Melanogaster Stranded at Second (Sas) Gene Encodes a Putative Epidermal Cell Surface Receptor Required for Larval Development." *Developmental Biology* 151(2):431–45.

Sela-Donenfeld, Dalit and David G. Wilkinson. 2005. "Eph Receptors: Two Ways to Sharpen Boundaries." *Current Biology* 15(6):R210–12.

Shibata, Tatsuo and Koichi Fujimoto. 2005. "Noisy Signal Amplification in Ultrasensitive Signal Transduction." *Proceedings of the National Academy of Sciences* 102(2):331–36.

Shindo, Asako and John B. Wallingford. 2014. "PCP and Septins Compartmentalize Cortical Actomyosin to Direct Collective Cell Movement." *Science* 343(6171):649–52.

Shraiman, Boris I. 2005. "Mechanical Feedback as a Possible Regulator of Tissue Growth." *Proceedings of the National Academy of Sciences* 102(9):3318–23.

Simões, Sérgio De Matos et al. 2010. "Rho-Kinase Directs Bazooka/Par-3 Planar Polarity during Drosophila Axis Elongation." *Developmental Cell* 19(3):377–88.

Simões, Sérgio de Matos, Avantika Mainieri, and Jennifer A. Zallen. 2014. "Rho GTPase and Shroom Direct Planar Polarized Actomyosin Contractility during Convergent Extension." *The Journal of Cell Biology* 204(4):575–89.

Simpson, Pat. 1979. "Parameters of Cell Competition in the Compartments of the Wing Disc of Drosophila." *Developmental Biology* 69(1):182–93.

Simpson, Pat and Ginès Morata. 1981. "Differential Mitotic Rates and Patterns of Growth in Compartments in the Drosophila Wing." *Developmental Biology* 85(2):299–308.

Slaughter, Danely P., Harry W. Southwick, and Walter Smejkal. 1953. "'Field Cancerization' in Oral Stratified Squamous Epithelium. Clinical Implications of Multicentric Origin." *Cancer* 6(5):963–68.

Stooke-Vaughan, Georgina A., Lance A. Davidson, and Sarah Woolner. 2017. "Xenopus as a Model for Studies in Mechanical Stress and Cell Division." *genesis* 55(1–2):e23004.

Sugimura, Kaoru, Pierre-François Lenne, and François Graner. 2016. "Measuring Forces and Stresses in Situ in Living Tissues." *Development (Cambridge, England)* 143(2):186–96.

Suijkerbuijk, Saskia J. E., Golnar Kolahgar, Iwo Kucinski, and Eugenia Piddini. 2016. "Cell Competition Drives the Growth of Intestinal Adenomas in Drosophila." *Current Biology* 26(4):428–38.

Sun, Gongping and Kenneth D. Irvine. 2011. "Regulation of Hippo Signaling by Jun Kinase Signaling during Compensatory Cell Proliferation and Regeneration, and in Neoplastic Tumors." *Developmental Biology* 350(1):139–51.

Sun, Zijun et al. 2017. "Basolateral Protrusion and Apical Contraction Cooperatively Drive Drosophila Germ-Band Extension." *Nature Cell Biology* 19(4):375–83.

Swain, P. S., M. B. Elowitz, and E. D. Siggia. 2002. "Intrinsic and Extrinsic Contributions to Stochasticity in Gene Expression." *Proceedings of the National Academy of Sciences* 99(20):12795–800.

Swarup, Sharan and Esther M. Verheyen. 2012. "Wnt/Wingless Signaling in Drosophila." *Cold Spring Harbor Perspectives in Biology* 4(6):a007930–a007930.

Tamada, Masako, Dene L. Farrell, and Jennifer A. Zallen. 2012. “Abl Regulates Planar Polarized Junctional Dynamics through β-Catenin Tyrosine Phosphorylation.” *Developmental Cell* 22(2):309–19.

Tamori, Yoichiro et al. 2010. “Involvement of Lgl and Mahjong/VprBP in Cell Competition” edited by N. E. Baker. *PLoS Biology* 8(7):e1000422.

Tamori, Yoichiro and Wu-Min Deng. 2011. “Cell Competition and Its Implications for Development and Cancer.” *Journal of Genetics and Genomics* 38(10):483–95.

Tamori, Yoichiro and Wu-Min Deng. 2013. “Tissue Repair through Cell Competition and Compensatory Cellular Hypertrophy in Postmitotic Epithelia.” *Developmental Cell* 25(4):350–63.

Tepass, Ulrich, Guy Tanentzapf, Robert Ward, and Richard Fehon. 2001. “Epithelial Cell Polarity and Cell Junctions in Drosophila.” *Annual Review of Genetics* 35(1):747–84.

Thompson, DW. 1917. “On Growth and Form (Edition 1).” *On growth and form.* 793.

Tsuboi, Alice, Daiki Umetsu, Erina Kuranaga, and Koichi Fujimoto. 2017. “Inference of Cell Mechanics in Heterogeneous Epithelial Tissue Based on Multivariate Clone Shape Quantification.” *Frontiers in Cell and Developmental Biology* 5(August).

Tyler, D. M., W. Li, N. Zhuo, B. Pellock, and N. E. Baker. 2007. “Genes Affecting Cell Competition in Drosophila.” *Genetics* 175(2):643–57.

Umetsu, Daiki, Benoît Aigouy, et al. 2014. “Local Increases in Mechanical Tension Shape Compartment Boundaries by Biasing Cell Intercalations.” *Current Biology* 24(15):1798–1805.

Umetsu, Daiki, Sebastian Dunst, and Christian Dahmann. 2014. “An RNA Interference Screen for Genes Required to Shape the Anteroposterior Compartment Boundary in Drosophila Identifies the Eph Receptor” edited by F. Pichaud. *PLoS ONE* 9(12):e114340.

Villa del Campo, Cristina, Cristina Clavería, Rocío Sierra, and Miguel Torres. 2014. “Cell Competition Promotes Phenotypically Silent Cardiomyocyte Replacement in the Mammalian Heart.” *Cell Reports* 8(6):1741–51.

Vincent, Jean-Paul, Alexander G. Fletcher, and L.Alberto Baena-Lopez. 2013. “Mechanisms and Mechanics of Cell Competition in Epithelia.” *Nature Reviews Molecular Cell Biology* 14(9):581–91.

Vincent, Jean-Paul, Golnar Kolahgar, Maria Gagliardi, and Eugenia Piddini. 2011. “Steep Differences in Wingless Signaling Trigger Myc-Independent Competitive Cell Interactions.” *Developmental Cell* 21(2):366–74.

Wagstaff, Laura et al. 2016. “Mechanical Cell Competition Kills Cells via Induction of Lethal p53 Levels.” *Nature Communications* 7:11373.

Wartlick, O. et al. 2011. “Dynamics of Dpp Signaling and Proliferation Control.” *Science* 331(6021):1154–59.

Wickham, Hadley. 2009. *ggplot2 Elegant Graphics for Data Analysis*.

Xu, Tian and Gerald M. Rubin. 1993. “Analysis of Genetic Mosaics in Developing and Adult Drosophila Tissues.” *Development (Cambridge, England)* 117(4):1223–37.

Yamamoto, Masatoshi, Shizue Ohsawa, Kei Kunimasa, and Tatsushi Igaki. 2017. “The Ligand Sas and Its Receptor PTP10D Drive Tumour-Suppressive Cell Competition.” *Nature* 542(7640):246–50.

Yu, Kun-hsing et al. 2016. “Predicting Non-Small Cell Lung Cancer Prognosis by Fully Automated Microscopic Pathology Image Features.” *Nature Communications* 7:12474.

Zallen, Jennifer A. and Richard Zallen. 2004. “Cell-Pattern Disordering during Convergent Extension in Drosophila.” *Journal of Physics: Condensed Matter* 16(44):S5073–80.

Zelditch, Miriam, Donald L. Swiderski, and H.David Sheets. 2012. *Geometric Morphometrics for Biologists (Second Edition)*.

Ziosi, Marcello et al. 2010. “dMyc Functions Downstream of Yorkie to Promote the Supercompetitive Behavior of Hippo Pathway Mutant Cells” edited by G. S. Barsh. *PLoS Genetics* 6(9):e1001140.

Ziv, O. et al. 2009. “The Co-Regulator dNAB Interacts with Brinker to Eliminate Cells with Reduced Dpp Signaling.” *Development* 136(7):1137–45.